# CODE SHIFT KEYING IMPULSE MODULATION FOR ULTRA WIDEBAND COMMUNICATIONS

by

Serhat Erküçük

M.A.Sc., Ryerson University, Toronto, Ontario, 2003

B.Sc., Middle East Technical University, Ankara, Turkey, 2001

A THESIS SUBMITTED IN PARTIAL FULFILLMENT
OF THE REQUIREMENTS FOR THE DEGREE OF

DOCTOR OF PHILOSOPHY

in the School
of
Engineering Science


SIMON FRASER UNIVERSITY
Summer 2007

## APPROVAL

**Name:** Serhat Erküçük

**Degree:** Doctor of Philosophy

**Title of thesis:** Code Shift Keying Impulse Modulation for Ultra Wideband Communications

**Examining Committee:** Dr. Ljiljana Trajković
Chair

---

Dr. Dong In Kim, Senior Supervisor

---

Dr. James K. Cavers, Supervisor

---

Dr. Paul K. M. Ho, Supervisor

---

Dr. Rodney Vaughan, Internal Examiner

---

Dr. Xiaodai Dong, External Examiner
Canada Research Chair (Tier-II) in UWB Commun.
Assoc. Prof., Electrical and Computer Engineering
University of Victoria

**Date Approved:** June 5, 2007

# Abstract

Ultra wideband impulse radio (UWB-IR) is a promising technology that has been recently investigated for high-rate data communications and low-rate location and ranging systems. Despite its many advantages including low-cost circuitry, use of unlicensed spectrum and multipath resolving capabilities, the current implementation of UWB-IRs exhibits some problems. Firstly, the conventional UWB-IR modulation format, pulse position modulation (PPM), uses consecutive fixed pulse transmit locations that are largely affected by multipath-delayed pulses, which degrades the system performance. Secondly, increasing the data rate of the most commonly used binary PPM (BPPM) format is still an open research problem. Thirdly, periodic time-hopping (TH) codes used for multiple-access generate undesired peaks for the spectrum, which may cause increased interference levels for the systems co-existing in the same bandwidth.

Considering above mentioned drawbacks of the current UWB-IRs, a new modulation format is proposed in this dissertation: Code Shift Keying (CSK) Impulse Modulation. $M$-ary CSK (MCSK), which can be employed by itself or combined with other UWB-IR modulations, achieves data transmission by selecting one of the $M$ orthogonal user-specific TH codes, where these TH codes are used to randomize pulse transmit locations. While the randomized pulse transmit locations reduce the effect of multipath-delayed pulses on the system performance, the random selection of TH codes increases the effective TH code period and suppresses the undesired peaks in the spectrum.

In this dissertation, CSK impulse modulation is studied in detail to quantify its performance improvement over the existing systems. Initially, MCSK is compared to $M$-ary PPM (MPPM) to show the advantage of randomizing pulse transmit locations over fixed locations. It is shown that MCSK can provide about 2 dB performance gain over MPPM in a multipath channel. Secondly, MSCK is combined with BPPM (i.e., MCSK/BPPM)

in order to increase the data rate of conventional TH-BPPM systems. It is shown that MCSK/BPPM can achieve improved system performance at increased data rate if system design parameters are properly selected. Finally, the power spectral density (PSD) characteristics of MCSK based IRs are studied. It is shown that the random selection of TH codes improves the resulting PSD with respect to that of conventional UWB-IRs.

Keywords: Code shift keying (CSK), impulse radios (IRs), ultra wideband (UWB) communications, randomized pulse transmit locations, increased data rate, improved power spectral density (PSD).

*To my family*

*"Cogito ergo sum."*

*— René Descartes (1596–1650)*

# Acknowledgments

I initially would like to thank my senior supervisor Prof. Dong In Kim for his excellent guidance, invaluable feedback and continuous support throughout my research work. I consider myself very lucky that I had the chance to work with him.

I would like to thank my examining committee for evaluating my dissertation and providing me their feedback on it. Special thanks to my supervisors Prof. James Cavers and Prof. Paul Ho for their constructive comments during my doctoral thesis proposal and the communications group presentations. I also would like to thank the external examiner Prof. Xiaodai Dong of the University of Victoria, the internal examiner Prof. Rodney Vaughan and the chair Prof. Ljiljana Trajković for serving on my examining committee.

I would like to acknowledge UWB-ITRC of Inha University, Korea as the primary source of financial support during my research work. I also would like to acknowledge support from Simon Fraser University, the School of Engineering Science, the Faculty of Applied Sciences and the Dean of Graduate Studies.

Finally, I would like to thank all my friends in the RF/Microwave Mobile Communications Laboratory and the School of Engineering Science staff and faculty for creating a friendly atmosphere in our department, where I spent my last four years.

# Contents

# List of Tables

# List of Figures

# List of Abbreviations

| | |
|---|---|
| **ACF** | autocorrelation function |
| **AWGN** | additive white Gaussian noise |
| **BER** | bit-error rate |
| **CDMA** | code-division multiple-access |
| **CF** | characteristic function |
| **CIR** | channel impulse response |
| **CSK** | code shift keying |
| **dB** | decibel |
| **DS** | direct sequence |
| **FCC** | Federal Communications Commission |
| **FIR** | finite impulse response |
| **GGD** | generalized Gaussian distribution |
| **GPS** | global positioning system |
| **GSM** | global system for mobile communications |
| **Hz** | hertz |
| **i.i.d** | independent identically distributed |
| **IR** | impulse radio |
| **LOS** | line-of-sight |
| **MA** | multiple-access |
| **MLSE** | maximum likelihood sequence estimation |
| **MUI** | multi-user interference |
| **NLOS** | non-line-of-sight |
| **OFDM** | orthogonal frequency division multiplexing |
| **OOK** | on-off keying |

| | |
|---|---|
| **pdf** | probability density function |
| **PAM** | pulse amplitude modulation |
| **PPAM** | pulse position amplitude modulation |
| **PPM** | pulse position modulation |
| **PSD** | power spectral density |
| **PSK** | phase shift keying |
| **PSM** | pulse shape modulation |
| **SER** | symbol-error rate |
| **SIR** | signal-to-interference ratio |
| **SNR** | signal–to–noise ratio |
| **TH** | time-hopping |
| **TR** | transmitted-reference |
| **UMTS** | universal mobile telecommunications system |
| **UWB** | ultra wideband |
| **WLAN** | wireless local area network |
| **WMAN** | wireless metropolitan area network |
| **WPAN** | wireless personal area network |
| **WWAN** | wireless wide area network |

# List of Symbols

| | |
|---|---|
| $\delta_d$ | pulse position modulation shift parameter |
| $d_i$ | $i$th transmitted bit |
| $E_b$ | bit energy |
| $E_s$ | symbol energy |
| $L_p$ | number of fingers in a partial-Rake receiver |
| $M$ | modulation order, e.g. $M$-CSK or $M$-PPM |
| $N_h$ | maximum time-hopping shift |
| $N_p$ | period of a time-hopping code |
| $N_s$ | pulse repetition number |
| $N_u$ | number of active users |
| $N_0$ | power spectral density of additive white Gaussian noise |
| $t$ | time, in seconds |
| $T_b$ | bit duration |
| $T_c$ | chip time |
| $T_f$ | frame time |
| $T_m$ | maximum delay spread |
| $T_p$ | pulse width |
| $T_s$ | symbol duration |

# List of Mathematical Conventions

| | |
|---|---|
| $\delta(\cdot)$ | Dirac delta function |
| $\mathbf{E}\{\cdot\}$ | expectation operator |
| $\mathcal{F}\{\cdot\}$ | Fourier transform |
| $Q(\cdot)$ | Q-function |
| $\lvert\cdot\rvert$ | absolute value operator |
| $\otimes$ | convolution operator |
| $\exp(x)$ | exponential, $e^x$ |
| $\hat{x}$ | decision on $x$ |
| $\lfloor x \rfloor$ | integer part of $x$ |
| $(\cdot)_x$ | base $x$ |
| $\log_x(\cdot)$ | logarithmic function to base $x$ |
| $\frac{d^n}{dx^n}(\cdot)$ | $n$th derivative of a function with respect to $x$ |
| $\max\{\mathbf{x}\}$ | maximum value in set $\mathbf{x}$ |
| $R_{xx}(\tau)$ | autocorrelation function of $x(t)$ |
| $S_{xx}(f)$ | power spectral density of $x(t)$ |

# Preface

This preface summarizes the research performed during my doctoral studies, and relates the resulting publications to this dissertation.

When I started my research on ultra wideband impulse radio (UWB-IR) communications in early 2004, my main interest was in increasing the data rate of UWB-IRs that use the conventional time-hopping binary pulse position modulation (TH-BPPM). After an extensive literature survey and evaluating pros and cons of the existing systems, we had the idea of transmitting extra information embedded in TH codes, while still using the BPPM modulation. This approach was the adoption of biorthogonal modulation combined with BPPM for code-division multiple-access (CDMA) systems proposed in [82] to UWB systems. With this approach, the incoming data selected one of the $M$ TH codes to transmit additional data in addition to BPPM modulated data, resulting in *$M$-ary code shift keying (MCSK)* impulse modulation combined with BPPM (i.e., MCSK/BPPM). This work was partially published in [70], and fully published in [71]. Also, a US patent application was filed regarding this work [83]. The combined MCSK/BPPM for increased data rate is presented in **Chapter 4** of this dissertation.

Parallel to our ongoing research on increasing the data rates of UWB-IRs, we also focused on the study of spectrum compliance of UWB-IRs. Since UWB systems should be designed to comply to spectral masks defined by spectrum regulatory agencies, study of power spectral densities (PSDs) resulting from different modulation formats is very important. Accordingly, we studied the PSD characteristics of MCSK based IRs and the effect of TH code set design on the spectrum. The main motivation of this work was to show the signalling advantages of MCSK based IRs over the conventional IRs in terms of PSD characteristics. This work was partially published in [76], and fully published in [67]. Also, an alternative method for evaluating the PSD was published in [40]. PSD characteristics of MCSK based IRs are

presented in **Chapter 5** of this dissertation.

After proposing a new modulation format for increased data rate and studying the resulting PSD, it was necessary to compare the MCSK impulse modulation to the same order $M$-ary PPM modulation. The main motivation of this work was to show the advantage of randomized pulse transmit locations over fixed locations. Although this work was the third main investigation of this dissertation, it is presented in **Chapter 3** before the other two main investigations for a better presentation of the dissertation. This work was partially published in [64], and fully published in [65]. Also, a former study that evaluated different channel models and Rake receivers, and motivated the mentioned investigation was published in [60].

Although the main scope of my research was the high-rate aspects of UWB communications, we also closely followed the standardization process of IEEE 802.15.4a, which is based on UWB-IRs that will be used for low-rate location and ranging systems in wireless personal area networks (WPANs). From January 2005 to January 2006, we contributed to this standardization process at different stages by proposing different modulation formats based on MCSK, presenting them at IEEE Wireless Standards meetings, and merging our proposals with other institutions or companies. Our contributions for IEEE 802.15.4a can be found in IEEE documents [84] – [86]. We also published some of the related research results at conferences [79], [87].[1] These papers consider the implementation of MCSK for the physical layer of IEEE 802.15.4a (i.e., burst transmission with fixed guard bands) and for chaotic signalling (an optional implementation for IEEE 802.15.4a), respectively. For these considerations, the implementation of *MSCK modulation* is significantly different from *MCSK impulse modulation* considered for high-rate data communications. In order not to divert the focus of MCSK impulse modulation, our research on low-rate UWB-IRs is not included in this dissertation.

In summary, this dissertation consists of three main investigations on high-rate UWB-IRs, which are published in various journals and conferences, as outlined in this preface. The details of these investigations can be found in Chapters 3–5.

[1]The paper presented at the flagship UWB conference (IEEE International Conference on Ultra Wideband, September 2005, Zurich, Switzerland) was selected as the runner-up paper, i.e., ranking between #4 to #6, in the Best Student Paper Award competition among 101 accepted student papers.

# Chapter 1

# Introduction

Wireless communications technologies have evolved faster than ever within the last decade. In today's wireless world, there are many standards for Wireless Wide, Metropolitan, Local and Personal Area Networks (respectively, WWAN, WMAN, WLAN, and WPAN). Fig. 1.1 depicts some of the established wireless standards and the current consideration of ultra wideband (UWB) communications in terms of coverage areas and target data rates. When coverage areas are considered, WWAN and WMAN can provide service at a wider range

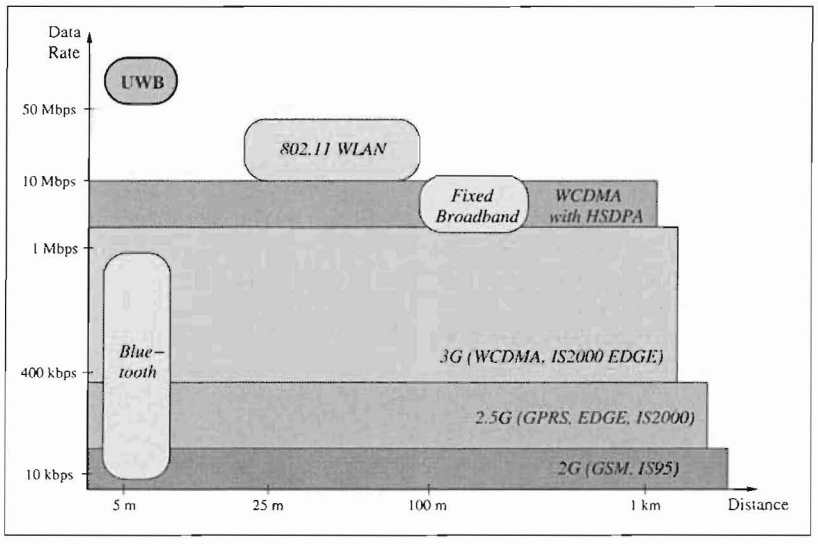


Figure 1.1: Today's wireless world in terms of coverage areas and data rates.

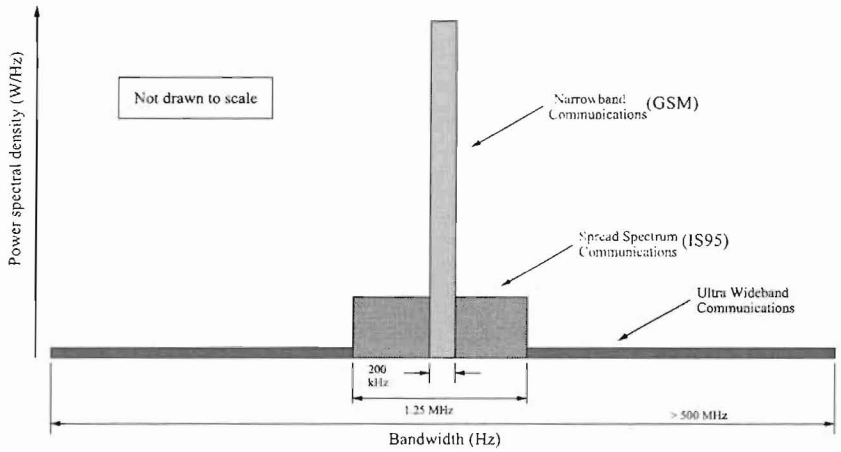


Figure 1.2: Power spectral density comparison for various communications systems.

with limited data rate, whereas WLAN and WPAN can provide higher data rates to employees or customers in an office or home environment. With the continuously increasing demand for higher-rate data services and their different applications, more standards will be developed in the near future and more devices will become *wireless*. This will bring the problem of *spectral crowding* as there will be less bands available for future systems. Therefore, new technologies that can co-exist with other systems without creating much interference will be of future interest. One of those new technologies is the *ultra wideband communications* systems.

In this chapter, initially the motivation for UWB communications is presented followed by the motivation for proposing the new *code shift keying* impulse modulation to overcome some of the problems associated with current UWB communications systems. The chapter is concluded with the dissertation organization.

## 1.1 Motivation for UWB Communications

UWB communications is a recent consideration that transmits its total power dissipated over a very large bandwidth. Accordingly, the resulting power spectral density (PSD) is very low compared to that of existing narrowband and spread spectrum communications systems. This allows the UWB system to co-exist with existing systems as the interference it creates is negligible. Fig. 1.2 illustrates the PSDs of narrowband, spread spectrum and

ultra wideband communications systems for comparison.

The first definition of UWB communications was made in the First Report and Order [1] released by Federal Communications Commission (FCC) of the United States in 2002 and has been accepted within IEEE Working Groups. According to this report, UWB systems should have a transmission bandwidth of at least 500 MHz, or the fractional bandwidth of these systems should be greater than 20%. Considering available technologies, there are currently two main considerations for UWB communications. The first one is the orthogonal frequency division multiplexing (OFDM) based UWB communications, which can use multiple sub-carriers to achieve at least 500 MHz bandwidth. The second one and the interest of this dissertation is the impulse radio based UWB communications, which transmits subnanosecond-duration pulses that can achieve at least 500 MHz bandwidth. These two technologies were considered for the WPAN standardization process of IEEE 802.15.3a (i.e., high-rate data communications) as multi-band OFDM (MB-OFDM) [2] and direct sequence UWB (DS-UWB) [3] proposals. Despite standardization efforts for a few years, neither of the proposals could become a standard. Therefore, the IEEE 802.15.3a Working Group decided to cease the standardization process in January 2006 in order for the market to decide. For the standardization process of IEEE 802.15.4a (i.e., low-rate precise location and ranging systems), impulse radio based UWB communications was agreed on as the main physical layer proposal. The standard draft of IEEE 802.15.4a [4] was approved as a new amendment to IEEE Std 802.15.4-2006 by the IEEE-SA Standards Board in March 2007 and will be available in June 2007.

Although different implementations of impulse radios were considered for IEEE 802.15.3a and IEEE 802.15.4a,[1] the *basic* impulse radio is considered in this dissertation as also considered in significant portion of studies in the literature. The basic impulse radio, which we refer to as UWB impulse radio (UWB-IR), was initially proposed by Win and Scholtz in [5] based on Scholtz's work on time-hopping impulse modulation [6], and later detailed in [7]. In [7], the authors presented UWB-IR as an ultra-wide bandwidth system that transmits subnanosecond-duration Gaussian monocycles, which achieves data transmission through binary pulse position modulation (BPPM) and multiple-access through user-specific time-hopping (TH) codes. This UWB-IR system serves as the benchmark and motivation of all UWB-IR communications studies in the literature. Following the work of Win and Scholtz,

[1] DS-UWB was considered for IEEE 802.15.3a and the transmission of bursts of pulses with fixed guard bands was considered for IEEE 802.15.4a.

various research areas emerged to improve the proposed system in terms of data rate, bit-error rate (BER) performance, spectral characteristics and cost efficiency. The research work done in the corresponding areas will be summarized in the next chapter, when the background information on UWB-IRs will be presented.

In addition to the attractive low PSD property of UWB-IRs, which allows them to co-exist with existing systems, low-cost circuitry, use of unlicensed spectrum and multipath resolving capabilities are the other main advantages of UWB-IRs. As a nature of UWB-IR communications, transmitting subnanosecond-duration pulses results in bandwidths in the order of a few GHz. This allows the UWB-IR system to transmit with a very low PSD, achieve very high data rates and have very fine time resolution. Accordingly, multipath-spread pulses can be effectively collected using a Rake receiver as most of the pulses can be resolved individually at the receiver. Cost efficient circuits used is also considered an important advantage of UWB-IRs. Without the need of a carrier frequency, the pulses can be shifted to the desired band by controlling their zero-crossings. Considering all these advantages, UWB-IR communications is an important consideration for some of the future technologies. Although there are many advantages associated with general aspects of UWB-IRs, there are some problems that need to be addressed when it comes to implementation. This includes the problems associated with current physical layer considerations, which make up the main motivation for the need of a new modulation.

## 1.2 Motivation for MCSK Impulse Modulation

$M$-ary code shift keying (MCSK) impulse modulation is the new modulation proposed in this dissertation to improve some aspects of conventional UWB-IRs. Before defining MCSK, let us overview the problems associated with existing UWB-IRs that motivated us proposing a new modulation.

The conventional UWB-IR modulation is the TH-BPPM proposed in [7]. This modulation uses BPPM for data transmission and user-specific TH codes to reduce catastrophic collisions that occur due to multiple-access. When this modulation format is employed, the data rate is limited by the BPPM. Therefore, either higher order modulations or alternative modulation formats should be proposed to meet the demand for higher data rates. Accordingly, our *first motivation* is to propose a new modulation format that can increase the data rate of the conventional TH-BPPM.

TH $M$-ary PPM (TH-MPPM) [8] is the most commonly considered modulation format that increases the data rate of the conventional TH-BPPM. In the conventional implementation of TH-MPPM, a single pulse is transmitted in one of the fixed $M$ consecutive pulse transmit locations. In a multipath channel, where Rake receivers are used to collect multipath energies [9], energy captures from consecutive pulse locations may be interfered by a large portion of the multipath-delayed received pulses. This may generate noticeable interference components for the $M$ decision variables, hence affecting the system performance. Accordingly, our *second motivation* is to increase the distance between consecutive pulse transmit locations so as to reduce the effect of multipath-delayed received pulses on the $M$ decision variables.

In a conventional UWB-IR system, which may use TH-BPPM or TH binary pulse amplitude modulation (TH-BPAM) [10], the PSD due to modulation effects results from data transmission and TH codes. Due to the periodicity of finite-length TH codes used in conventional UWB-IRs, the spectrum exhibits undesired peaks for both continuous and discrete spectrum that may cause significant interference to co-existing systems. These peaks can be smoothed and suppressed if the TH code length can be made infinite. However, this cannot be achieved easily considering the TH code design issues and the realization of TH codes at the receiver [11]. Accordingly, our *third motivation* is to increase the effective TH code period so as to smooth the continuous spectrum and suppress the discrete spectral components.

Considering the three motivations stated above, we propose a new UWB-IR modulation format, namely, $M$-ary Code Shift Keying impulse modulation, that can inherently address all the above concerns. MCSK impulse modulation achieves data transmission by selecting one of the $M$ orthogonal user-specific TH codes with the incoming $M$-ary data, where the selected TH codes are used to randomize pulse transmit locations. With this new modulation,

- a higher order modulation than TH-BPPM can be proposed, where the system design parameters can be adjusted to provide improved system performance at increased data rate,
- the separation between consecutive pulse transmit locations can be increased with respect to that of MPPM, while the data rate is fixed,

- reduced catastrophic collisions can still be maintained with the random selection of user-specific TH codes, and
- the effective TH code period can be increased with the random selection of TH codes in order to improve the PSD characteristics of conventional UWB-IRs.

The advantages stated above will be discussed and studied in the following chapters, when MCSK impulse modulation will be elaborated on.

By proposing MCSK impulse modulation for UWB-IRs in this dissertation, three main contributions are made to the UWB-IR communications area as presented in Chapters 3–5. In Chapter 3, MCSK is compared to the conventional TH-MPPM to show the advantage of pulse location randomization on the system performance. In Chapter 4, MCSK is combined with BPPM to increase the data rate of the conventional TH-BPPM at improved system performance. In Chapter 5, PSD characteristics of MSCK based UWB-IRs are studied to show how MCSK smoothes and suppresses the undesired spectral peaks resulting from conventional UWB-IRs.

Besides the main contributions of MCSK, novel approaches used in interference modelling, system analysis and spectrum evaluation are the other contributions of this dissertation. These contributions include accurate multi-user interference modelling in a multipath channel using the generalized Gaussian distributions in Chapter 3, calculation of the characteristic functions of multi-user interference terms in an additive white Gaussian noise channel in Chapter 4, exact analysis of the PSD by considering every shift for data and TH code changes in Chapter 5 and the TH code set design that controls the quantity and location of discrete spectral components in Chapter 5. Both the main and the other contributions will be elaborated on in the corresponding chapters.

As a summary, proposing and studying MCSK impulse modulation in this dissertation has resulted in several contributions to the UWB-IR communications area and academic community. In the following, the organization of the dissertation is outlined.

## 1.3 Dissertation Organization

This dissertation consists of six chapters, where the motivation for proposing a new UWB-IR modulation, i.e., MCSK impulse modulation, is presented in this chapter, i.e., Chapter 1. In the next chapter, i.e., Chapter 2, the background information on the existing UWB-IRs

will be presented together with the summary of ongoing research that tries to improve the current UWB-IRs. In Chapters 3–5,[2] the new MCSK impulse modulation will be studied, detailed and compared to conventional UWB-IRs to quantify its improvement over the current UWB-IR considerations. Finally, in Chapter 6, concluding remarks regarding the proposed MCSK modulation will be given. A more detailed outline of each chapter is presented as follows.

In **Chapter 2**, background information on UWB-IRs and the related literature survey are presented. Initially, existing modulation options and alternative transceiver structures are discussed. Then, PSD characteristics resulting from both pulse spectrum and modulation effects are given. Finally, multipath channel characteristics of UWB-IRs are presented.

In **Chapter 3**, MCSK impulse modulation is studied in detail, where it randomizes consecutive pulse transmit locations of the conventional TH-MPPM in order to reduce the effect of multipath delays on the decision variables. Initially, system models for the MCSK impulse modulation and TH-MPPM are described for a fair comparison model. MCSK and TH-MPPM systems are then analyzed in terms of the symbol-error rate (SER), where the upper and lower bounds on the SER are derived for single- and multi-user cases in the approximate $T_c$-spaced channel model. An implementable Rake receiver structure is then presented for the accurate $\tau$-spaced channel model to be used with simulation studies. At the end of the chapter, numerical and simulation results are presented to verify the SER analysis, and to show the advantages of MCSK over the conventional TH-MPPM.

In **Chapter 4**, MCSK/BPPM, a new modulation format, for UWB-IR communications is proposed and analyzed. Initially, the proposed MCSK/BPPM modulation system is described, and the system design parameters are explained in detail. The MCSK/BPPM system is analyzed in terms of the SER, where the upper and lower bounds on the SER are derived. Numerical and simulation results are presented to verify the theoretical SER analysis, and to show the advantages of the proposed system over the conventional TH-BPPM. For that, different combinations of system parameters are presented that yield improved system performance for MCSK/BPPM over TH-BPPM at increased data rate. Finally, the receiver complexities of both modulations are compared.

In **Chapter 5**, the effects of different code design techniques on the PSD and the

[2]In Chapters 3–5, some system model definitions (e.g., system parameters) may be repeated. This is necessary to maintain clarity and consistency within each chapter.

multiple access capability of MCSK based UWB-IRs are investigated. Initially, the PSD that accounts for TH code changes within a frame time is derived, verified and compared to the PSD of conventional UWB-IRs. Two main code design techniques are introduced for MCSK, and their effects on spectrum shaping and multiple access capability are discussed. Based on the PSD improvement of MCSK based UWB-IRs, some suggestions are made for the conventional UWB-IRs.

In **Chapter 6**, conclusions of the dissertation are presented. Initially, contributions of the proposed modulation to UWB-IR communications area are summarized. Finally, some future research directions are suggested.

# Chapter 2

# UWB Impulse Radios

In this chapter, the background information on ultra wideband impulse radios (UWB-IRs) is presented. The chapter starts with the presentation of different modulation options for UWB-IRs. These include the conventional modulations, the modulations that are designed to increase the data rates of conventional modulations and the signalling schemes that use autocorrelation receivers such as transmitted-reference systems. Next, power spectral density (PSD) characteristics of UWB-IRs are presented including pulse spectrum, effects of modulations on the PSD and the studies on co-existence. The chapter is concluded with the overview of UWB channel characteristics including channel measurement studies, the analytical multipath channel model obtained and the channel model assumptions used in the literature.

## 2.1 Modulation Options

### 2.1.1 Conventional modulations

The UWB-IR communications system has been detailed for the first time in [7]. The system model presented here achieves data transmission through binary pulse position modulation (BPPM) and multiple access capability through user specific time-hopping (TH) codes. Following the work in [7], possible modulation formats for UWB-IRs were studied and presented in [12] including on-off keying (OOK), positive-valued pulse amplitude modulation (PAM), binary phase shift keying (BPSK)[1] (also known as binary PAM (BPAM)) and BPPM.

[1]BPAM is equivalent to BPSK and will be used throughout the dissertation.

Among these modulations, BPPM and BPAM were the ones widely accepted and studied in the literature [13] – [15], mainly due to their superior performances or implementation advantages. We refer to these modulations as *conventional* UWB-IR modulations. In the following, these two modulations are described for multiple access schemes, where they are used with TH codes.

Conventional UWB-IR modulations **TH-BPPM** and **TH-BPAM** show similar signalling structures and are presented together. The signal that transmits the $i$th symbol (one-bit) of the $k$th user using conventional TH-BPPM and TH-BPAM can be modelled respectively as

$$s^{(k)}_{BPPM}(t) = \sqrt{\frac{E_b}{N_s}} \sum_{j=(i-1)N_s}^{iN_s-1} w_{tr}\Big(t - jT_f - c_j^{(k)}T_c - {d_i}^{(k)}\delta_d\Big) \tag{2.1}$$

$$s^{(k)}_{BPAM}(t) = \sqrt{\frac{E_b}{N_s}} \sum_{j=(i-1)N_s}^{iN_s-1} {d_i}^{(k)} w_{tr}\Big(t - jT_f - c_j^{(k)}T_c\Big). \tag{2.2}$$

The system parameters associated with these modulations are explained below:

- $w_{tr}(t)$ denotes the transmitted pulse with pulse width $T_p$. It is normalized so that $\int_{-\infty}^{+\infty} w_{tr}^2(t)dt = 1$.
- $T_f$ is the frame time to transmit one pulse, $N_s$ is the number of pulses used to transmit one symbol and $T_s = N_sT_f$ is the symbol duration. Since one-bit is transmitted with these modulations, $T_b$, bit duration, can be replaced with $T_s$.
- $E_b$ is the bit energy.
- $\mathbf{c}^{(k)} = \{c_0^{(k)}, c_1^{(k)}, \ldots, c_{N_p-1}^{(k)}\}$ is the $k$th user's $N_p$-long TH code consisting of integers, where each user is assigned a user-specific TH code to allow for multiple access in the system.
- The TH code satisfies $\{0 \leq c_j^{(k)} < N_h; \forall j, \forall k\}$, where $N_h$ is the maximum TH shift.
- In order to prevent inter-pulse interference, $N_hT_c + \delta_d + T_m \leq T_f$ where $T_c \geq T_p$ is the chip time, $\delta_d$ is the time shift parameter of BPPM (in case of BPAM, $\delta_d = 0$) and $T_m$ is the maximum delay spread. This condition may be relaxed if shorter $T_f$ is desired.
- For BPPM ${d_i}^{(k)} \in \{0, 1\}$ and for BPAM ${d_i}^{(k)} \in \{-1, 1\}$ carry the $i$th symbol information of the $k$th user.

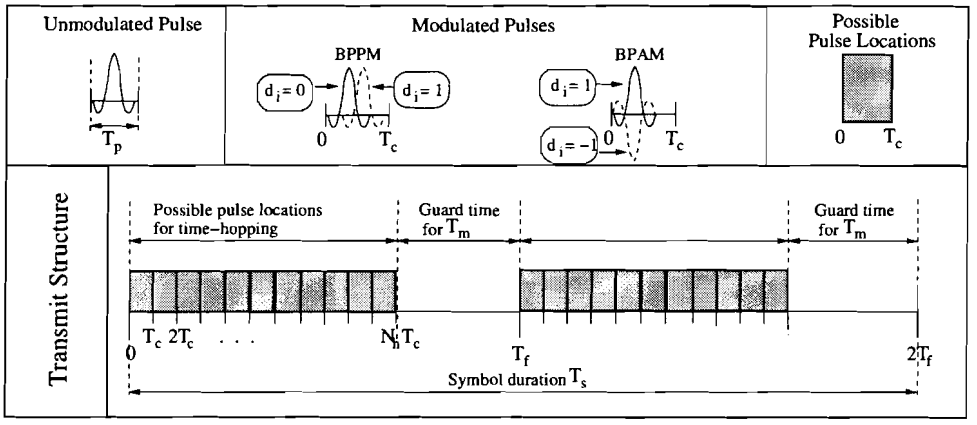


Figure 2.1: Transmit structures of conventional TH-BPPM and TH-BPAM.

In Fig. 2.1, the transmit structures and the associated system parameters of TH-BPPM and TH-BPAM are illustrated for $N_s = 2$, i.e., symbol duration $T_s = 2T_f$. While BPAM is an antipodal signalling, shift parameter $\delta_d$ of BPPM may be selected for either orthogonal or overlapping signalling spaces. Here, it is illustrated for the overlapping case as will be explained when Gaussian monocycles are presented.

In the analytical UWB-IR studies, it is widely accepted that the receive antenna *ideally* acts as a time-domain differentiator on the pulse. Accordingly, the received pulse $w_{rec}(t)$ is represented as the derivative of the transmitted pulse $w_{tr}(t)$ [7]. Rake receivers are commonly used in UWB-IR communications to collect multipath-spread pulses by correlating the received signal with the template waveform. The template waveform used is generally the same as received pulse in order to maximize the correlation. Accordingly, the received pulse $w_{rec}(t)$ is important in performance evaluations. In the following chapters, $w(t)$ will be used to represent the pulse that takes into account the effects of channel and transmit/receive antennas on $w_{tr}(t)$ and $w_{rec}(t)$ when system performances are studied.

Gaussian monocycles are one set of pulses that have been studied from both the performance and spectrum perspectives [16] – [18], following the second order Gaussian monocycle used in [7]. Also, different pulse shapes such as Hermite polynomials [19] and prolate spheroidal functions [20] have been considered. It is shown that the performance of a conventional modulation with high order Gaussian monocycles (eg., $4^{th}$ and $6^{th}$) is better than the one that uses Hermite pulses and similar to the one that uses prolate spheroidal pulses [18].

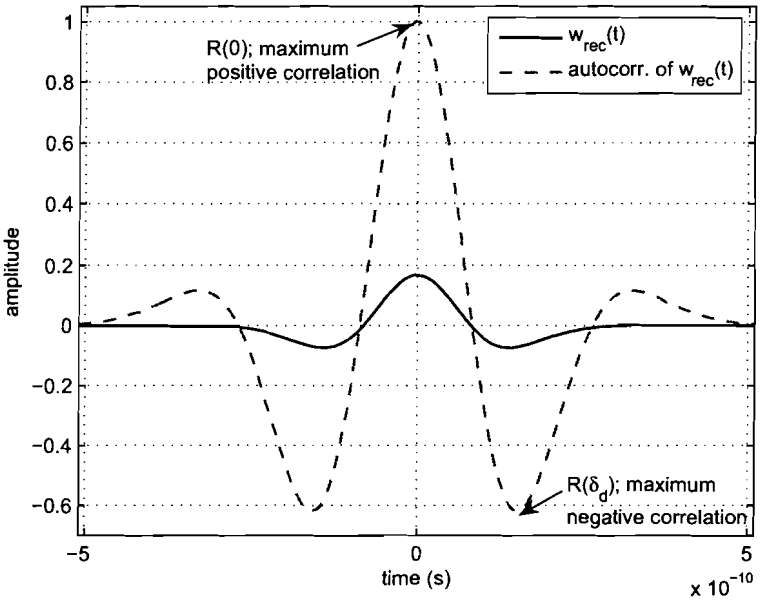


Figure 2.2: $2^{nd}$ order Gaussian monocycle and its autocorrelation function.

It is also concluded that generating Gaussian monocycles is easier than the generation of prolate spheroidal pulses, which do not have a closed-form representation. More will be elaborated on pulse shapes when the pulse spectrum is presented. An $n$th order Gaussian monocycle is the $n$th derivative of the basic Gaussian function and is given by [16]

$$p_n(t) = \varepsilon_n \frac{d^n}{dt^n} \exp\left[-2\pi \left(\frac{t}{\tau_m}\right)^2\right] \tag{2.3}$$

where $\varepsilon_n$ is used to normalize the pulse energy and $\tau_m$ is the time normalization factor. Selection of different order Gaussian monocycles affects the system performance mainly due to autocorrelation properties of the pulses when timing errors are considered [16]. In Fig. 2.2, the second order Gaussian monocycle used in [7]

$$w_{rec}(t) = \left[1 - 4\pi \left(\frac{t}{\tau_m}\right)^2\right] \exp\left[-2\pi \left(\frac{t}{\tau_m}\right)^2\right] \tag{2.4}$$

and its autocorrelation function $R(x) = \int_{-\infty}^{\infty} w_{rec}(t-x) w_{rec}(t) dt$ are plotted. It can be observed that the system performance (when there is no timing error) can be maximized

if the BPPM shift $\delta_d$ is selected to maximize $|R(0) - R(\delta_d)|$. Accordingly, pulse transmit locations in BPPM may be partially overlapping as previously illustrated in Fig. 2.1.

### 2.1.2 Higher-rate modulations

After studying the conventional binary modulations and possible pulses that they may be used with, let us consider modulations that are designed to increase the data rates of binary modulations.

**$M$-ary PPM**

The most commonly considered modulation format to increase the data rate of TH-BPPM is the TH-MPPM. TH-MPPM shows a similar signalling structure to TH-BPPM given in (2.1) and is expressed as

$$s_{MPPM}^{(k)}(t) = \sqrt{\frac{E_s}{N_s}} \sum_{j=(i-1)N_s}^{iN_s-1} w_{tr}\Big(t - jT_f - c_j^{(k)}T_c - {d_i}^{(k)}\delta_d\Big). \tag{2.5}$$

Eq. (2.5) differs from (2.1) by two parameters: (i) $E_s$ is the symbol energy, and (ii) ${d_i}^{(k)} \in \{0, 1, \ldots, M-1\}$. While the BPPM shift parameter $\delta_d$ is usually selected for overlapping signalling spaces to maximize the system performance, $\delta_d$ for MPPM is usually selected to satisfy orthogonal pulse locations.

There have been various studies on MPPM in the literature. In [8], $M$-ary PPM signals are investigated to improve the multiple access performance for a given number of users and data transmission rate with respect to the BPPM results presented in [6]. In [21], capacity of MPPM is investigated over additive white Gaussian noise (AWGN) channels. In [22], performance of TH-MPPM is analyzed in the presence of multi-user interference (MUI) and timing jitter. To characterize the MUI, Gaussian quadrature rules method is used instead of the inaccurate Gaussian approximation used in many studies. In [23], a general method for the evaluation of the symbol-error rate (SER) of both MPPM and $M$-ary PAM UWB-IR systems is presented in the presence of multipath channel, multi-user and strong narrowband interference. Although $M$-ary PAM is also considered in some other studies [13], [24], high order PAM is likely to violate the spectral mask defined by FCC [1] and therefore, MPAM is not considered for the current implementation of UWB-IRs.

**Hybrid PPM and PAM**

Another approach to increase the data rate is the hybrid combination of conventional modulations. In [25], hybrid pulse amplitude and position modulation scheme is proposed.

The proposed system is reported to potentially double the throughput of a BPPM or BPAM system, where the analytical error rate expressions of the system are derived over lognormal fading channels. In [26], pulse position amplitude modulation (PPAM) is proposed, where the channel capacity is determined for a multiple-access system. The error probability and performance bounds are derived for a multi-user environment in an AWGN channel.

**Pulse shape modulation**

Besides MPPM, MPAM and hybrid of these modulations, achieving data transmission through the transmission of different pulse shapes is another approach to increase the data rate. This approach is named pulse shape modulation (PSM). Using the advantage of the orthogonality of the modified Hermite polynomial function, multiple Hermite pulses are simultaneously transmitted in addition to BPPM, and appropriate error correction coding is employed to achieve improved performance at higher rate communications [19]. In order to generate the modified orthogonal Hermite pulses, the $n$th order modified Hermite polynomial given by

$$p_n(t) = (-1)^n \exp\left[\frac{t^2}{4}\right] \frac{d^n}{dt^n} \exp\left[-\frac{t^2}{2}\right] \tag{2.6}$$

is used. Although the proposed modulation can achieve increased data rate, it suffers from (i) violating the FCC spectral mask since each pulse has a different power spectrum, and (ii) the need for different circuits to achieve high data rates. Accordingly, the data rate will be limited by the number of different pulse generators available. In [27], FCC spectral mask is considered while generating the modified Hermite pulses, but the realization of the circuits and the cost of this approach still remain as a problem. In [28], a more detailed method is presented that can generate orthogonal sets of Hermite pulse waveforms occupying the same frequency band, which is a further improvement of [27].

In Sections 2.1.1 and 2.1.2, the presented modulations use Rake receivers [9] in order to collect multipath-spread pulses. This requires the knowledge of the channel and the use of many Rake fingers to achieve a good system performance. Therefore, the implementation of the UWB-IR system may be costly. To eliminate the need for estimating channel coefficients, systems that transmit reference pulses and use autocorrelation receivers are also considered in the literature. Such approaches are given in the next section.

### 2.1.3 Autocorrelation receivers

Considering the cost and complexity of using Rake receivers, a simple transceiver structure known as the transmitted-reference (TR) system has been proposed and studied in the literature. In a conventional TR system, a pair of pulses is transmitted in each frame, where the first pulse is used as a reference pulse and the second pulse is used as a data pulse to send information in terms of pulse polarity or position. At the receiver, the reference pulse is delayed, correlated with the data pulse and integrated to detect the transmitted information. Although the TR system eliminates channel estimation, it resembles differential detection that suffers from noise enhancement due to the cross-correlation operation and 3 dB power efficiency loss due to the transmission of a reference pulse.

The first known TR receiver for UWB-IR systems has been proposed in [29]. The signalling structure of a TR system can be given by

$$s_{TR}^{(k)}(t) = \sqrt{\frac{E_b}{2N_s}} \sum_{j=(i-1)N_s}^{iN_s-1} \left[ w_{tr}\left(t - jT_f - c_j^{(k)}T_c\right) + {d_i}^{(k)} w_{tr}\left(t - jT_f - c_j^{(k)}T_c - T_d^{(k)}\right)\right] \tag{2.7}$$

where the first pulse is the unmodulated reference pulse and the second pulse is the data pulse transmitted $T_d^{(k)}$ seconds later with the information ${d_i}^{(k)} \in \{-1, 1\}$. With this signal model, the system performance and the data rate depend on $T_d$, the inter-pulse distance. The other main factor that controls the system performance is the integration interval. The TR system has been well-studied in the literature. In [30], a hybrid receiver structure that performs a filtering matched to the hopping sequence, and a subsequent correlation of the data pulses with the reference pulses is analyzed both in AWGN and multipath channels. In [31], an analytical framework based on the sampling expansion approach is presented, where a closed-form expression for the bit-error probability of TR signalling is derived. Also, there have been studies that try to increase the data rate of TR systems by decreasing $T_d$. In [32], a dual pulse transmission scheme is proposed to increase the data rate with shorter inter-pulse distance and to cancel out the inter-pulse interference. In [33], an $M$-ary orthogonal coded/balanced signalling scheme is proposed to realize higher rate TR systems, where the inter-pulse interference resulting from overlapping multipath-delayed pulses is mitigated by combining the signalling and a pair of balanced matched filters in a joint manner. With this approach, inter-pulse distances can be effectively reduced in TR systems.

In Sections 2.1.1–2.1.3, various modulation options were overviewed from data rate and

system performance perspectives. In the literature, these systems are usually evaluated with the perfect synchronization assumption, as also will be the case for the code shift keying impulse modulation studied in the following chapters. A more realistic case for performance study is the presence of timing jitter. Some of the investigations that study the effect of timing jitter on the system performance can be found in [22], [34], [35], where they consider autocorrelation properties of the pulses.

## 2.2 Spectral Characteristics

After the overview of modulation options, spectral characteristics of UWB-IRs are presented in this section. Studying the PSD characteristics of UWB-IRs is important since the UWB-IR communications systems are designed to occupy the same bandwidth with some of the existing systems. Although the UWB-IR transmit power is very low, there have been some concerns about the UWB systems creating interference to co-existing systems. Accordingly, some spectral masks have been defined by regulatory agencies, where the UWB-IR transmit power is limited for a given bandwidth. Since the UWB-IR systems designed should conform to the defined spectral masks, effects of pulse shapes and modulations on the PSD should be carefully studied. In the following, unmodulated pulse spectrum and the modulation effects on the PSD are discussed in detail. At the end of the section, some studies on the co-existence issue are summarized.

### 2.2.1 Pulse spectrum

The UWB spectral mask [1] defined by FCC is the most commonly referred to spectral mask in the literature.[2] The current FCC spectral mask defines two conditions:
(i) The maximum power emission of UWB transmission is restricted to -41.3 dBm/MHz (i.e., 75 nW/MHz) in the range of 3.1 GHz to 10.6 GHz.
(ii) Power emission in the range 0.96 GHz to 3.1 GHz is more conservative. Maximum emission values are 10 dBm/MHz to 35 dB/MHz lower than -41.3 dBm/MHz.

Considering the given constraints, there have been different pulse design approaches in order to conform to the spectral mask. In [17], higher-order Gaussian monocycles are considered in order to meet the FCC spectral mask. Firstly, it is shown that the Gaussian

[2]It should be noted that spectral mask considerations in many countries are also similar to that of FCC.

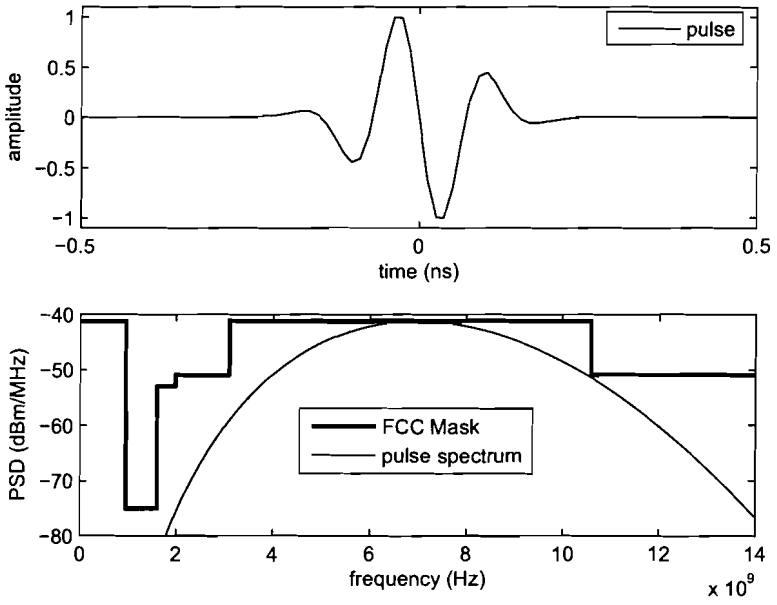


Figure 2.3: Upper plot: $5^{th}$ order Gaussian monocycle. Lower plot: FCC spectral mask.

monocycle considered in [7] violates the spectral mask even if the pulse width is decreased. In order to shift the pulse to the [3.1, 10.6] GHz frequency range, zero crossings of the pulses are increased with higher order Gaussian monocycles. A table that provides the parameters of pulses conforming to the FCC spectral mask is given in the paper. In Fig. 2.3, a $5^{th}$ order Gaussian monocycle that conforms to the FCC spectral mask is plotted in the upper plot, and its pulse spectrum and the FCC mask are plotted in the lower plot.

In addition to higher order Gaussian monocycles that can meet the FCC spectral mask, some other pulse design techniques were proposed in the literature. In [36], optimal design techniques are developed for waveforms synthesized by the digital finite impulse response (FIR) filter structure proposed in [37]. This approach formulates an optimization problem which has the spectral utilization as its objective and explicitly imposes all design constraints, including the spectral mask constraint. The resulting design method yields pulses that maximize the spectral utilization and are guaranteed to conform to the spectral mask, and hence there is no need to interactively search for suitable parameter values. In [38], a pulse design algorithm that uses different rectangular window filters for even and odd

symmetric pulses has been proposed and studied. Also, Hamming and Hanning windows are considered in this study for evaluation. With this approach, the generated pulses are time-limited so as to reduce the interference, which also simplifies the implementation. Although the approach does not maximize spectral utilization unlike [36], yet the pulses are represented with a closed-form representation and conform to the FCC mask. The other pulse shapes that are designed to satisfy the FCC mask include prolate spheroidal wave functions [20] and Hermite pulses [28]. These pulse shapes were presented in Section 2.1.1, when Gaussian monocycles were introduced.

The code shift keying impulse modulation that will be studied in the following chapters can be used with any of the pulses above. Therefore, another pulse design approach is not proposed in this dissertation. When any modulation is employed with the above designed pulses, the PSD will be affected by the modulation effects in addition to the pulse spectrum. Although a pulse may be designed to conform to the FCC spectral mask, the modulated signal may violate the power emission limits and should be carefully considered.

### 2.2.2 Effects of modulation on the PSD

The effect of modulation on the PSD is well studied in the literature for the conventional modulation formats. For a UWB-IR system, there are two main modulation factors: data modulation and time-hopping for multiple access. While the assumptions on data modulation are clear and consistent throughout the literature, assumptions on time-hopping vary. These assumptions include (i) no TH codes, (ii) finite-length periodic TH codes, and (iii) TH codes with infinite period. Among these assumptions, finite-length periodic TH codes is the most realistic consideration.

When conventional modulations are considered with finite-length TH codes, the periodically transmitted signal can be represented for both TH-BPPM and TH-BPAM as

$$y(t) = \sum_{k=-\infty}^{\infty} s\Big(t - k(N_p T_f)\Big) \tag{2.8}$$

if (2.1) and (2.2) are substituted into (2.8), respectively. Here, $y(t)$ is the continuously transmitted UWB-IR signal, where $s(t)$ is periodic with $N_p T_f$. The PSD of $y(t)$ is

$$S_{yy}(f) = |W_{tr}(f)|^2 \cdot S_{cc}(f) \tag{2.9}$$

where $|W_{tr}(f)|^2$ is the squared-magnitude spectrum of the unmodulated pulse and $S_{cc}(f)$ is the PSD of the modulation effects. $|W_{tr}(f)|^2$, which is directly related to the pulse spectrum,

was studied in the previous subsection. A general representation for $S_{cc}(f)$ can be given as

$$S_{cc}(f) = S_{cont}(f) + S_{disc}(f) \tag{2.10}$$

where $S_{cont}(f)$ and $S_{disc}(f)$ are the continuous spectrum and discrete spectral components, respectively. Calculation of $S_{cc}(f)$ will be elaborated on in Chapter 5. While the presence or absence of continuous and discrete terms in (2.10) will be determined by the data modulation, undesired peaks in the PSD will be determined by periodic TH codes. In [39], the effect of deterministic TH codes on the spectrum is studied, where the PSD terms resulting from TH codes are explicitly represented. In [40], the effect of TH code randomization on the PSD when code shift keying used is explicitly studied to smooth the undesired peaks in the PSD. In [41], the effect of TH code parameters on the PSD is studied by varying the number of possible shift locations.

There are also studies that assume infinite-length TH codes. In [42], the influence of the modulation format, multiple access format, and pulse shape on the PSD characteristics of impulse radios is discussed considering the FCC spectral mask. It is shown that the discrete spectral components due to PPM can be eliminated using polarity randomization. This approach is later detailed in [43] by considering pulse-by-pulse and symbol-by-symbol polarity randomizations. In [44], PSD of various time-hopping spread-spectrum (TH-SS) signalling schemes in the presence of random timing jitter is studied. By considering the Fourier transform of basic baseband pulse, PSD of different TH formats is shown to be tractable, where a general PSD representation can be obtained. Both finite- and infinite-length TH code cases can be evaluated using the general PSD representation presented in this paper.

Following the presentation of pulse spectrum and the modulation effects on the PSD, some of the works that study the co-existence issues are overviewed next.

### 2.2.3 Co-existence issues

The FCC defined power emission level below 3.1 GHz is very low, where most existing systems including GSM900, UMTS/WCDMA and GPS operate. On the other hand, the IEEE 802.11a Wireless Local Area Network (WLAN) system operates within the [3.1, 10.6] GHz frequency range, where the UWB-IR and the WLAN systems may generate mutual interference. This has caused a mutual concern and has been studied in the literature.

Before the release of the FCC spectral mask in 2002, there were also concerns for other systems including GSM900, UMTS/WCDMA and GPS. Accordingly, a study has been conducted on in-band interference power caused by different kinds of UWB signals at some predefined frequency bands [45]. The interference levels are studied as functions of the UWB pulse width at the frequency bands of GSM900, UMTS/WCDMA and GPS. Also, the UWB system performance degradation in an AWGN channel in the presence of interfering systems GSM and UMTS/WCDMA is considered. It is found that the interference in the frequency bands studied is the smallest if the pulse waveform is based on higher order Gaussian waveforms. When the UWB system degradation is studied, it is observed that the system performance suffers the most if the interference and the nominal center frequency of the UWB system are overlapping.

After the FCC spectral mask, an analysis of the co-existence issues of UWB with other devices in the same spectrum is provided [46]. Specifically, the interference to and from devices using the WLAN standard IEEE 802.11a is focused on. The results indicate that a UWB interferer operating at the peak allowable power density induces minimal interference into such WLAN devices in line-of sight (LOS) scenarios, even at close range. However, in the non-LOS (NLOS) case, a UWB interferer can severely affect the data-rate sustainable by 802.11a systems. Moreover, 802.11a interference into UWB systems is shown to reduce the signal-to-interference ratio (SIR) by as much as 36 dB when the interferer is within LOS of the UWB receiver.

Besides the co-existence analysis for performance degradations, reduced data rates and SIR levels, some studies have addressed to minimize the interference levels by spectrum shaping. These approaches are either based on pulse design [47] or TH code design [48], and generate spectral nulls at desired frequencies. In [47], a transmitter pulse shaping filter is formed as a coded Gaussian monocycle pulse where the codeword is obtained by approximating the Fourier series representation of the desired spectrum shaping. In [48], the design and optimization of TH codes to suppress the interference imposed by UWB-IRs is considered. In both cases, it is reported that the interference level is effectively reduced with the spectral nulls generated for the frequency band of IEEE 802.11a systems.

## 2.3 UWB Channel Characteristics

After the overview of modulation options and spectral characteristics, UWB channel characteristics are presented in this section.

### 2.3.1 Channel measurements

UWB channel characteristics in the frequency range [3.1, 10.6] GHz are different from narrowband and wideband channel characteristics. Accordingly, various measurement campaigns have been conducted to obtain measurement results to use in modelling the UWB channel characteristics. The first set of channel measurements collected were the responses to IEEE 802.15.3a call for contributions on UWB channel models. There were ten responses that presented reports on measurement conditions and results to the IEEE 802.15.3a Working Group. Some of the contributions can be found in [49] – [53]. Considering the similar observations in these reports and harmonizing them, a final report was presented to the committee, that proposed a multipath channel model [54]. This final report considers four channel types depending on the signalling path and the distance between transmitter and receiver as shown in Table 2.1. These four considerations are mainly adopted from [49], [50].

Table 2.1: Multipath channel type considerations for IEEE 802.15.3a.

| Channel type | Environment | Distance |
|---|---|---|
| CM1 | LOS | 0–4 m |
| CM2 | NLOS | 0–4 m |
| CM3 | NLOS | 4–10 m |
| CM4 | NLOS (heavy multipath) | 4–10 m |

The report [54] proposes a UWB channel model derived from the Saleh-Valenzuela model [55] with a couple of slight modifications, based on the clustering phenomenon observed in several channel measurements. The report recommends using a lognormal distribution rather than a Rayleigh distribution for the multipath gain magnitude, since the observations show that the lognormal distribution seems to better fit the measurement data. In addition, independent fading is assumed for each cluster as well as each ray within the cluster. The multipath model presented in [54] has been widely used in performance evaluations, despite it is limited to only indoor residential and office environments within 10 m range.

After [54], there have been a considerable number of papers published on the measurement and modelling for specific environments, but none of them has gained widespread acceptance for system testing purposes mainly due to not being contested by IEEE Working Groups. An overview of these measurements can be found in [56]. Recently, a comprehensive standardized model for ultrawideband propagation channels is presented in [57]. The model has been developed by the authors during their work for the IEEE 802.15.4a group, and was accepted by that body as the official model for comparing different system proposals for standardization. The channel model presented in [57] is more comprehensive than the model presented in [54] since it includes more specific measurement environments, as well it includes a number of refinements and improvements to previously presented channel models. It is also stressed by the authors that the 802.15.4a channel model presented in the paper is valid for UWB systems irrespective of their data rate and their modulation format (i.e., also valid for IEEE 802.15.3a considerations).

During the preparation of this dissertation, only the IEEE 802.15.3a channel model [54] was officially available. Therefore, only that model has been considered in system performance evaluations in the following chapters. In the next subsection, the published IEEE 802.15.3a multipath channel model is presented.

### 2.3.2 Multipath channel model

The UWB multipath channel model consists of the following discrete-time impulse response [54]

$$h(t) = \sum_{l=0}^{L} \sum_{k=0}^{K} \alpha_{k,l}\, \delta\Big(t - T_l - \tau_{k,l}\Big). \tag{2.11}$$

Parameters associated with this model are explained below.

- $\alpha_{k,l}$ is the gain coefficient of $k$th ray in $l$th cluster and $\tau_{k,l}$ is the arrival time of $k$th ray relative to $l$th cluster's arrival time $T_l$.
- The inter-cluster and inter-ray arrival times are independent and exponentially distributed.
- $\alpha_{k,l} = p_{k,l}\,\beta_{k,l}$ where $p_{k,l}$ is equiprobable $\pm 1$ to account for signal inversion due to reflections.

- $\beta_{k,l}$ is a lognormal random variable, denoted by $20\log_{10}(\beta_{k,l}) \propto N(\mu_{k,l}, \sigma^2)$, where $\mu_{k,l}$ and $\sigma^2$ are given in [54].
- The power delay profile is double exponentially decaying and given by $\mathbf{E}\{\beta_{k,l}^2\} = \Omega_0 \exp(-T_l/\Gamma)\exp(-\tau_{k,l}/\gamma)$, where $\mathbf{E}\{\cdot\}$ is the expectation operator, $\Omega_0$ is the mean power of the first ray of first cluster, and $\Gamma$ and $\gamma$ represent the power decay factors of the cluster and ray, respectively.

In order to model and evaluate different channel types (i.e., CM1–CM4), the parameters can be obtained from [54]. In system performance evaluations and simulations in the following chapters, the simplified channel impulse response will be used, where (2.11) can be equivalently represented as [56]

$$h(t) = \sum_{l=0}^{L-1} h_l\, \delta(t - \tau_l). \tag{2.12}$$

Here, $L$ is the total number of multipaths, $h_l$ is the $l$th multipath coefficient and $\tau_l$ is the delay of $l$th multipath component.

### 2.3.3 Channel model assumptions in the literature

An important issue overlooked in most of the studies is the channel model assumptions. When channel realizations are generated from (2.12), if two multipath components arrive within less than the pulse width, there may occur pulse overlappings. While wider bandwidth systems may observe less number of pulse overlaps (e.g., a UWB-IR system with 5 GHz bandwidth), 500 MHz bandwidth systems (e.g., IEEE 802.15.4a consideration) will largely be affected by overlapping pulses. In most of the analytical studies, where the typical 500 MHz – 2 GHz bandwidth UWB systems are considered [58], it is assumed that multipath arrivals are at multiples of chip time, irrespective of the system bandwidth, to simplify the analysis. Many simulation studies also consider this assumption, where the reported system performances may be inaccurate due to ignoring the effect of inter-pulse interferences. For more accurate performance results, channel models that account for pulse overlappings should be considered.

In the following, two channel models,[3] namely the accurate $\tau$-spaced channel model and the approximate $T_c$-spaced channel model are presented.

[3]In the dissertation, CM1–CM4 are referred to as "channel types", whereas $\tau$-spaced and $T_c$-spaced models are referred to as "channel models".

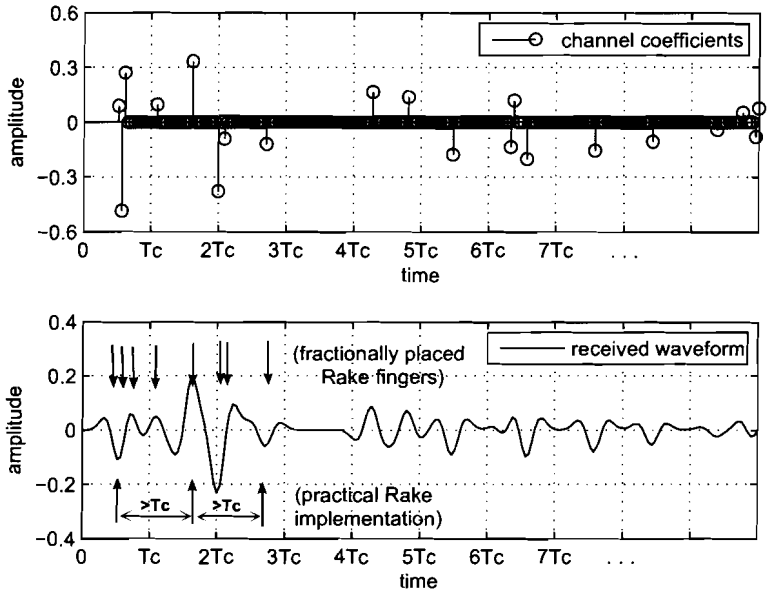


Figure 2.4: Illustration of $\tau$-spaced channel model and the Rake fingers.

### $\tau$-spaced channel model

The $\tau$-spaced channel model uses the exact multipath delay locations and amplitudes of channel coefficients given in (2.12), and accounts for possible pulse overlaps. There are only few papers that use this model in performance analysis [58], [59], where only semi-analytical results are presented. When using this model, the locations and tap weights of Rake fingers should be calculated from the channel coefficients in order to maximize the captured multipath energies [60], while conforming to the criterion of Rake fingers being separated by at least $T_c$ [9]. Accordingly, the performance of the UWB-IR systems depends on how well the Rake receiver can be implemented. When determining the Rake fingers, some studies use channel estimation techniques [61], whereas most other studies assume perfect knowledge of the channel. Also, some studies assume that the Rake fingers can be placed fractionally (i.e., even less than chip time $T_c$) [61], [62]. However, a realizable Rake structure is when the Rake fingers are separated by at least $T_c$. In Fig. 2.4, multipath channel coefficients and the received waveform are plotted in upper and lower plots, respectively. It can be observed that the received waveform is distorted due to pulse overlappings. To capture multipath energies, Rake implementations are illustrated for two considerations.

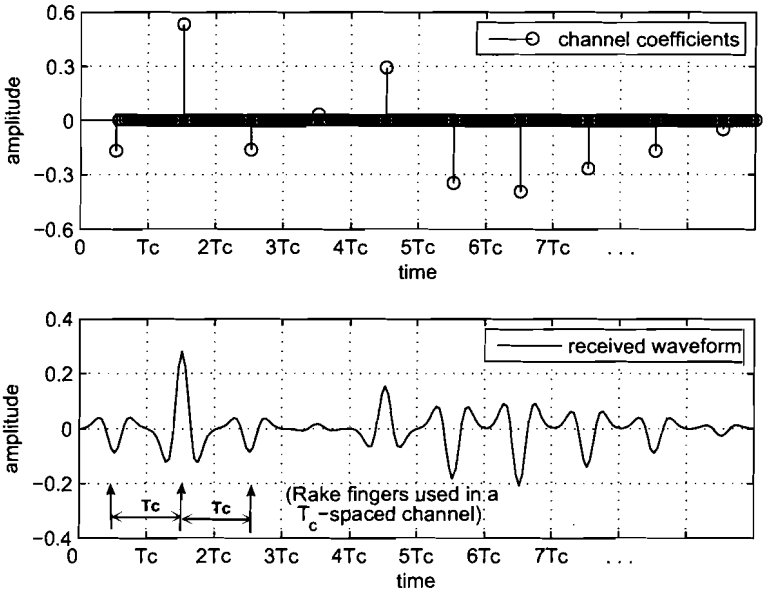


Figure 2.5: Illustration of $T_c$-spaced channel model and the Rake fingers.

**$T_c$-spaced channel model**

The $T_c$-spaced channel model assumes the arrival of multipaths at multiples of chip time $T_c$. Accordingly, this model can be represented as

$$h'(t) = \sum_{l=0}^{L-1} h'_l \delta(t - \tau'_l) \tag{2.13}$$

where $\tau'_l = kT_c$, $k$ is an integer and $h'_l$ are the channel coefficients. $\{h'_l\}$ can be obtained by lowpass or bandpass filtering $h(t)$ given in (2.12) followed by downsampling at multiples of $T_c$ [30], or by linearly combining coefficients quantized to the same chip time [63]. In Fig. 2.5, a $T_c$-spaced channel model is illustrated for multipath channel coefficients, received waveform and Rake finger locations. It can be observed that each pulse is resolved individually and pulse energies can be collected ideally.

In this chapter, the background information on UWB-IRs was presented. In the following three chapters, $M$-ary code shift keying impulse modulation will be studied in detail to address the issues summarized in Chapter 1.

# Chapter 3

# MCSK Impulse Modulation

In the previous two chapters, the motivation for a new ultra wideband impulse radio (UWB-IR) modulation and the background information on the current UWB-IRs were presented. In this chapter, $M$-ary code shift keying (MCSK) impulse modulation, a new modulation for UWB-IRs, is presented as the first main contribution of this dissertation.[1] The main motivation of the MCSK impulse modulation considered here is to randomize consecutive pulse transmit locations of the conventional time-hopping $M$-ary pulse position modulation (TH-MPPM) in order to reduce the effect of multipath delays on the decision variables.

## 3.1 Introduction

In UWB-IR communications, TH binary PPM (TH-BPPM) is the most commonly considered modulation format. Due to its limited data rate, TH-MPPM is the conventional modulation considered mainly to meet the demand for higher data rate. MPPM based UWB-IRs, including the TH-MPPM, have been widely studied in the literature [21] – [23]. In the conventional implementation of TH-MPPM, a single pulse is transmitted in one of the fixed $M$ consecutive pulse transmit locations. For multiple-access, user-specific TH codes are used to further shift the pulses to randomized locations in order to reduce catastrophic collisions. At the receiver, signal energy is captured from $M$ consecutive locations after synchronizing with the user-specific TH code. In a multipath channel, where Rake receivers are used to collect multipath energies [9], energy captures from consecutive pulse locations

[1] The material presented here is a combination of the works published in [64] and [65].

may be interfered by a large portion of the multipath-delayed received pulses, which may generate noticeable interference components for the $M$ decision variables, hence affecting the system performance.

The effect of interference components on $M$ decision variables can be totally eliminated if consecutive pulse transmit locations can be separated by the duration of multipath delay spread. However, such an implementation would significantly reduce the data rate. Given the high data rate and multiple-access capability constraints, a more feasible approach is to randomize the consecutive pulse transmit locations using $M$ orthogonal TH codes. With this approach, (i) the separation between consecutive pulse transmit locations can be increased while the data rate is fixed, and (ii) reduced catastrophic collisions can still be maintained with the random selection of user-specific TH codes. This new UWB-IR modulation format is referred to as $M$-ary code shift keying impulse modulation. In the following, MCSK impulse modulation will be introduced and detailed with the specific focus of the *randomizing effect* on pulse transmit locations.

MCSK is considered here for both single- and multi-user cases. In the study of the single-user case, the effect of multipath-delayed pulses on $M$ decision variables is explicitly provided in terms of channel impulse response coefficients. In the study of the multi-user case, an accurate semi-analytic symbol-error rate (SER) expression is derived based on modelling the multi-user interference (MUI) terms with the *generalized* Gaussian distribution (GGD) presented in [66]. Some approximations to MUI modelling are provided in Section 3.5, which increase the computational efficiency of numerical analysis significantly with respect to the simulation studies, while still providing accurate results. For all the analysis, the commonly used approximate $T_c$-spaced channel model is considered for convenience. In order to provide more *realistic* results, system performances are also provided in the accurate $\tau$-spaced channel model with *implementable* Rake receiver structures [60]. When *practical* implementations of MCSK and MPPM are considered, it is shown that MCSK can provide about 2 dB performance gain over MPPM as it reduces the effects of multipath delays on the decision variables by randomizing pulse transmit locations. This performance gain is mainly a result of the separated $M$ decision variables experiencing less interference terms due to the decaying power delay profile.

The rest of the chapter is organized as follows. In Section 3.2, system models for the MCSK impulse modulation and TH-MPPM are described. MCSK and TH-MPPM systems

are analyzed in Section 3.3 in terms of the SER, where the upper and lower bounds on the SER are derived for single- and multi-user cases. In Section 3.4, an implementable Rake receiver structure is presented for the accurate $\tau$-spaced channel model. In Section 3.5, numerical and simulation results are presented to verify the SER analysis, and to show the advantages of MCSK over the conventional TH-MPPM. The concluding remarks are given in Section 3.6.

## 3.2 System Model

An analogy can be made between MCSK and MPPM as they both use one of the $M$ pulse locations to transmit information. While the conventional TH-MPPM uses $M$ consecutive pulse locations shifted by a TH code, MCSK randomizes the pulse locations through $M$ TH codes. Due to the similarity and the difference of these two modulations, the signalling structures should be clearly defined for a fair comparison.

Let us initially start with TH-MPPM. The signal that transmits the $i$th symbol of the $k$th user using conventional TH-MPPM can be modelled as

$$s^{(k)}_{MPPM}(t) = \sqrt{\frac{E_s}{N_s}} \sum_{j=(i-1)N_s}^{iN_s-1} w\Big(t - jT_f - c_j^{(k)}T_c - d_i{}^{(k)}\delta_d\Big) \tag{3.1}$$

where $w(t)$ denotes the transmitted pulse, which includes the effects of transmitting and receiving antennas, with unit energy and pulse width $T_p$. The other system parameters are explained in detail after (2.2) for the general PPM format and after (2.5) for the $M$-ary PPM format. Using TH-MPPM, a pulse is initially shifted to one of the $N_h$ TH locations, and further shifted to one of the $M$ *consecutive* data-bearing pulse locations within a frame time $T_f$.

As opposed to consecutive fixed pulse transmit locations in MPPM, MCSK transmits pulses at randomized locations determined by $M$ TH codes. Accordingly, MCSK combines the TH shift and the PPM shift in (3.1) and achieves data transmission through one of the $M$ TH codes as

$$s^{(k)}_{MCSK}(t) = \sqrt{\frac{E_s}{N_s}} \sum_{j=(i-1)N_s}^{iN_s-1} w\Big(t - jT_f - \big(c^{(k)}_{d_i^{(k)}}\big)_j T_c\Big) \tag{3.2}$$

where $\left\{0 \le \big(c^{(k)}_{d_i^{(k)}}\big)_j < N_h + M - 1; \forall j, \forall k\right\}$ is equivalent to the combined TH and PPM

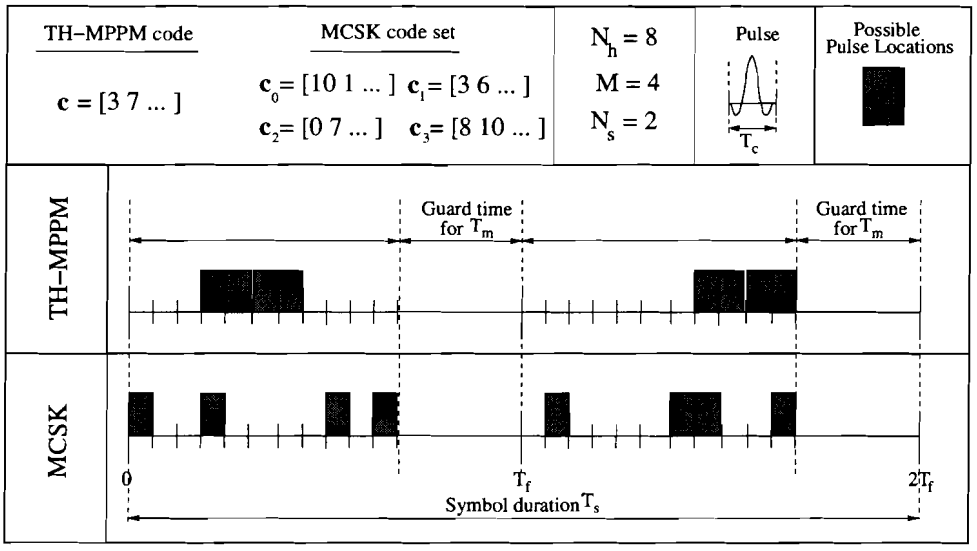


Figure 3.1: Illustration for TH-MPPM and MCSK transmit structures.

shift effect in MPPM and $d_i^{(k)} \in \{0, \ldots, M-1\}$ selects one of the $M$ TH codes of user $k$. Contrary to a single TH code $\mathbf{c}^{(k)}$ being assigned to each user in TH-MPPM, a TH code set consisting of $M$ TH codes $\{\mathbf{c}_0^{(k)}, \mathbf{c}_1^{(k)}, \ldots, \mathbf{c}_{M-1}^{(k)}\}$ is assigned to each user in MCSK, where $\mathbf{c}_m^{(k)} = \{(c_m^{(k)})_0, \ldots, (c_m^{(k)})_{N_p-1}\}$. Each TH code set is generated independently for each user to allow for multiple access. In each TH code set, the codes are designed to satisfy $\{(c_0^{(k)})_j \neq \ldots \neq (c_{M-1}^{(k)})_j, \forall j, \forall k\}$ to ensure orthogonal pulse transmit locations. For reduced collisions [7] and suppressed PSD components [67] in order to conform to the PSD limits for the given MHz bandwidth [1], it is further assumed that $(c_m^{(k)})_j$ is uniformly distributed over $[0, N_h + M - 2]$ while conforming to the TH code design constraints above. With these TH code sets, MCSK randomizes pulse transmit locations within each frame time. For better understanding of the differences between TH-MPPM and MCSK, their signalling structures are illustrated in Fig. 3.1 for a single-user when $N_h = 8$, $M = 4$, $N_s = 2$ for the given TH code sets. It can be observed that TH-MPPM transmits the pulses at $M$ consecutive locations further shifted by its TH code, whereas MCSK randomizes the pulse transmit locations based on its TH code set.

For a multiple-access system consisting of $N_u$ users with perfect power control, the received signal $r(t)$ at the output of the receive antenna can be modelled as

$$r(t) = \sum_{k=1}^{N_u} s^{(k)}(t - \tilde{\tau}_k) \otimes h_k(t) + n(t) \tag{3.3}$$

where $h_k(t)$ is the $k$th user's channel impulse response (CIR), $\otimes$ is the convolution operator, $\tilde{\tau}_k$ is the time asynchronism between the users and $n(t)$ is the additive white Gaussian noise (AWGN) with two-sided power spectral density $N_0/2$. $h_k(t)$ is given as [56]

$$h_k(t) = \sum_{l=0}^{L-1} h_{k,l}\delta(t - \tau_{k,l}) \tag{3.4}$$

with the assumption $\sum_{l=0}^{L-1} h_{k,l}^2 = 1$, $\forall k$ in order to remove the path loss factor, where $h_{k,l}$ is the $k$th channel's $l$th multipath coefficient, $\tau_{k,l}$ is the delay[2] of the $k$th channel's $l$th multipath component and $\delta(\cdot)$ is the Dirac delta function. For the commonly used approximate $T_c$-spaced channel model, $\{\tau_{k,l}\}$'s are assumed to be at the multiples of $T_c$ (i.e., $l \cdot T_c$) with the corresponding $\{h_{k,l}\}$ normalized accordingly, whereas for the accurate $\tau$-spaced model, $\{\tau_{k,l}\}$ and $\{h_{k,l}\}$ take the exact values for the given CIR.

Assuming a partial-Rake receiver with $L_p$ fingers, perfectly estimated CIR coefficients for user 1 and $T_c$-spaced channel model for simplicity in analysis, the correlator output statistics of the first user $\{D_m^{(1)}\}$ for the first symbol transmitted in a multipath channel are computed as

$$D_m^{(1)} = \sqrt{\frac{N_s}{E_s}} \sum_{j=0}^{N_s-1} \sum_{l=0}^{L_p-1} h_{1,l} \int_{jT_f}^{(j+1)T_f} r(t)\, w_{m,temp}^{(1)}(t)\, dt \tag{3.5}$$

for $\{m = 0, \ldots, M-1\}$, where

$$\begin{aligned} w_{m,temp,\,MPPM}^{(1)}(t) &= w\Big(t - jT_f - c_j^{(1)}T_c - mT_c - lT_c\Big) \\ w_{m,temp,\,MCSK}^{(1)}(t) &= w\Big(t - jT_f - (c_m^{(1)})_j T_c - lT_c\Big) \end{aligned}$$

are the template waveforms used by MPPM and MCSK, respectively. Given $d_0^{(1)}$ is transmitted,[3] (3.5) can be simplified for both MPPM and MCSK as

$$D_m^{(1)} = S_m + I_m + N_m \tag{3.6}$$

[2]The path delay $\tau_{k,l}$ is distinguished from the user delay $\tilde{\tau}_k$ by the sign "~".

[3]The user index (1) of $d_0^{(1)}$ and $c_m^{(1)}$ is omitted in the following text for mathematical convenience.

where $S_m$ is the output signal term, $I_m$ is the MUI term and $N_m$ is the output noise term. $S_m$ and $N_m$ can be given for MPPM and MCSK, respectively, as

$$S_m = \sum_{j=0}^{N_s-1} \sum_{l=0}^{L_p-1} h_{1,l} h_{1,(l+m-d_0)}\,, \qquad N_m = \sum_{j=0}^{N_s-1} \sum_{l=0}^{L_p-1} h_{1,l} n_{(j,l+m-d_0)} \tag{3.7}$$

$$S_m = \sum_{j=0}^{N_s-1} \sum_{l=0}^{L_p-1} h_{1,l} h_{1,(l+(c_m)_j-(c_{d_0})_j)}\,, \qquad N_m = \sum_{j=0}^{N_s-1} \sum_{l=0}^{L_p-1} h_{1,l} n_{(j,l+(c_m)_j-(c_{d_0})_j)} \tag{3.8}$$

where $h_{1,l} = 0$ for $l < 0$, and $\{n_{(a,b)};\ \forall a,\ \forall b\}$ are independent noise terms with $\sigma_n^2 = \frac{N_s}{2E_s/N_0}$. The common interference term $I_m$ is

$$I_m = \sqrt{\frac{N_s}{E_s}} \sum_{j=0}^{N_s-1} \sum_{l=0}^{L_p-1} \sum_{k=2}^{N_u} h_{1,l} \int_{jT_f}^{(j+1)T_f} \left( s^{(k)}(t-\tilde{\tau}_k) \otimes h_k(t) \right) \cdot w_{m,temp}^{(1)}(t)\, dt \tag{3.9}$$

and can be calculated for MPPM and MCSK by replacing the corresponding template waveform. $I_m$ will be elaborated on in the next section when generalized Gaussian distributions will be used to model the MUI. The transmitted symbol $d_0$ is then estimated for MPPM and MCSK as

$$\mathbf{max}\left\{D_m^{(1)}\right\} \;\Rightarrow\; m \;\Rightarrow\; \hat{d}_0. \tag{3.10}$$

## 3.3 Analysis of the Symbol-Error Rate

The transmitted symbol $d_0$ will be detected correctly at the receiver if $D_{d_0}^{(1)} > D_m^{(1)},\ \forall m,\ m \neq d_0$. Accordingly, the probability of error given $d_0$ is transmitted can be formulated as

$$P(e|d_0) = \Pr\Big[ \bigcup_{\substack{m=0 \\ m \neq d_0}}^{M-1} S_{d_0,m} + I_{d_0,m} + N_{d_0,m} < 0 \,\Big|\, d_0 \Big], \tag{3.11}$$

where $S_{d_0,m} = (S_{d_0} - S_m)$, $I_{d_0,m} = (I_{d_0} - I_m)$ and $N_{d_0,m} = (N_{d_0} - N_m)$. For convenience we here define $P_e(m|d_0)$, the *pair-wise* error probability of receiving $m$, given $d_0$ is transmitted, as

$$P_e(m|d_0) = \Pr\Big[ S_{d_0,m} + I_{d_0,m} + N_{d_0,m} < 0 \,\Big|\, d_0 \Big]. \tag{3.12}$$

Since the $M-1$ pair-wise error probabilities $\{P_e(m|d_0)\}$ are mutually dependent, an exact SER expression, $P_e$, is not allowed. Hence, the lower and upper bounds on $P_e$ can be evaluated as

$$\sum_{d_0=0}^{M-1} P(d_0)P^{(L)}(e|d_0) \leq P_e \leq \sum_{d_0=0}^{M-1} P(d_0)P^{(U)}(e|d_0) \tag{3.13}$$

$$\text{with} \quad P^{(L)}(e|d_0) = \max_{\substack{0\leq m\leq M-1 \\ m\neq d_0}} \Big\{P_e(m|d_0)\Big\} \quad \text{and} \quad P^{(U)}(e|d_0) = \sum_{\substack{m=0 \\ m\neq d_0}}^{M-1} P_e(m|d_0)$$

where $P(d_0)$ is the probability of $d_0$ being transmitted.

In the following subsections, the SER of TH-MPPM and MCSK are evaluated for single- and multi-user cases, where the single-user case is considered to explicitly observe the effects of fixed and randomized pulse locations and the multi-user case is considered to include the effect of MUI on the SER by modelling it with the accurate GGD.

### 3.3.1 Single-user case

Let us initially consider TH-MPPM. In the case of a single-user, $P_e(m|d_0)$ in (3.12) becomes a function of $S_{d_0,m}$ and $N_{d_0,m}$ since $I_{d_0,m} = 0$. For known channel coefficients $\{h_{1,l}\}$, (3.12) can be viewed as a binary modulation when $S_{d_0,m}$ is corrupted by the output noise value $N_{d_0,m}$ [9]. Therefore, (3.12) can be evaluated as

$$P_{e,MPPM}(m|d_0) = Q\Big(\sqrt{SNR_{d_0,m}}\Big) \tag{3.14}$$

where $Q(\cdot)$ is the Q-function and $SNR_{d_0,m}$ is the output signal-to-noise ratio (SNR) of the decision variable defined as

$$SNR_{d_0,m} = \frac{|S_{d_0,m}|^2}{\sigma^2_{N_{d_0,m}}} \tag{3.15}$$

for $m \neq d_0$, where $\sigma^2$ denotes the variance of $N_{d_0,m}$. Assuming the channel coefficients $\{h_{1,l}\}$ are known, using (3.7) the output SNR can be simplified to

$$SNR_{d_0,m} = \frac{2E_s}{N_0} \cdot H(d_0, m, L_p) \tag{3.16}$$

where $H(d_0, m, L_p)$ explicitly represents the effects of CIR and the partial-Rake receiver on the output SNR and is given by

$$H(d_0, m, L_p) = \frac{\left[\sum_{l=0}^{L_p-1}\left(h_{1,l}^2 - h_{1,l}h_{1,(l-(d_0-m))}\right)\right]^2}{\sum_{l_1',l_2',l_3'}\left(h_{1,l'} - h_{1,(l'+(d_0-m))}\right)^2}. \tag{3.17}$$

Here, the summation regions $l_1'$, $l_2'$ and $l_3'$ are defined as $\{l_1' | -(d_0 - m) \leq l' \leq -1\}$, $\{l_2' | 0 \leq l' \leq L_p - 1\}$ and $\{l_3' | L_p \leq l' \leq L_p - 1 - (d_0 - m)\}$, where these regions may or may not exist depending on the value of the $(d_0, m)$-pair. Also to note, $h_{1,l} = 0$ for only $l < 0$, whereas $h_{1,l'} = 0$ for $l' < 0$ and $l' > L_p - 1$.

Two interesting notes can be made with respect to $H(d_0, m, L_p)$ given in (3.17). First of all, it is independent of $N_s$, the number of pulses transmitted in a symbol. Therefore, increasing the symbol duration for a fixed frame time does not improve the output SNR value and hence the system performance, when no MUI is present. Secondly, it is a function of the difference $(d_0 - m)$. Therefore, different $(d_0, m)$-pairs may result in the same values since the relative differences are fixed in MPPM.

The SER of MCSK can be found similarly, but the computation of $P_{e,MCSK}(m|d_0)$ is different from that of $P_{e,MPPM}(m|d_0)$ due to the definition of $(d_0, m)$-pairs. In MCSK, each distinct $(d_0, m)$-pair refers to the selection of independent TH codes. Therefore, $P_{e,MCSK}(m|d_0)$ is not a function of $(d_0 - m)$ but a function of $\left((c_{d_0})_j - (c_m)_j\right)$, where $\left\{(c_m)_j, \forall m, \forall j\right\}$ are assumed to be uniformly distributed over $[0, N_h + M - 2]$ with the condition $(c_{d_0})_j \neq (c_m)_j$. Hence, the difference $C_j = \left((c_{d_0})_j - (c_m)_j\right)$ has the probability density function (pdf)

$$f_{C_j}(x) = \sum_{\substack{C_j=-(N_h+M-2) \\ C_j \neq 0}}^{N_h+M-2} \frac{(N_h + M - 1) - |C_j|}{(N_h + M - 1) \cdot (N_h + M - 2)} \cdot \delta(x - C_j) \tag{3.18}$$

when considered for every $j$ value. Since $C_j$ is independent $\forall j, j \in [0, N_s - 1]$, $S_{d_0,m}$ and $N_{d_0,m}$ become functions of $\left\{C_j | j = 0, \ldots, N_s - 1\right\}$, which indicates the combinations of different $C_j$ values. Accordingly, $P_{e,MCSK}(m|d_0)$ can be derived as

$$P_{e,MCSK}(m|d_0) = \sum_{\substack{C_0=-(N_h+M-2) \\ C_0 \neq 0}}^{N_h+M-2} \cdots \sum_{\substack{C_{N_s-1}=-(N_h+M-2) \\ C_{N_s-1} \neq 0}}^{N_h+M-2} \frac{(N_h + M - 1) - |C_0|}{(N_h + M - 1) \cdot (N_h + M - 2)} \cdots$$
$$\frac{(N_h + M - 1) - |C_{N_s-1}|}{(N_h + M - 1) \cdot (N_h + M - 2)} Q\left(\sqrt{SNR_{d_0,m}(\{C_j\})}\right). \tag{3.19}$$

$SNR_{d_0,m}(\{C_j\})$ can be computed using (3.8) and is given by

$$SNR_{d_0,m}(\{C_j\}) = \frac{|S_{d_0,m}(\{C_j\})|^2}{\sigma^2_{N_{d_0,m}(\{C_j\})}} = \frac{2E_s}{N_0} \cdot H(\{C_j\}, L_p) \tag{3.20}$$

$$\text{where} \quad H(\{C_j\}, L_p) = \frac{\left[\sum_{j=0}^{N_s-1} \sum_{l=0}^{L_p-1} \left(h_{1,l}^2 - h_{1,l} h_{1,(l-C_j)}\right)\right]^2}{N_s \sum_{j=0}^{N_s-1} \sum_{l_1',l_2',l_3'} \left(h_{1,l'} - h_{1,(l'+C_j)}\right)^2}. \tag{3.21}$$

Here, the summation regions $l_1'$, $l_2'$ and $l_3'$ are defined as $\{l_1' | -C_j \leq l' \leq -1\}$, $\{l_2' | 0 \leq l' \leq L_p - 1\}$ and $\{l_3' | L_p \leq l' \leq L_p - 1 - C_j\}$ with the same boundary constraints given after (3.17).

By comparing (3.21) with (3.17), two apparent advantages of MCSK over MPPM can be observed. First of all, the interference terms $\{h_{1,(l-C_j)}\}$ in MCSK coming from other $M-1$ decision variables are more separated from the desired terms $\{h_{1,l}\}$ than the interference terms $\{h_{1,(l-(d_0-m))}\}$ in MPPM due to the larger distribution range of $C_j$. Accordingly, for a decaying power delay profile, it is expected that the interference caused by multipath-delayed pulses will have less effect on the decision variables of MCSK. Secondly, $\{C_j\}$ are independent for $\{j = 0, \ldots, N_s - 1\}$. Therefore, combining independent $\{C_j\}$ increases the diversity gain and it is expected that the performance gain of MCSK over MPPM will increase with $N_s$ increasing, since MPPM is independent of $N_s$ for the single-user case.

### 3.3.2 Multi-user case

In the presence of multiple interfering users, the MUI term $I_{d_0,m}$ should also be included in the calculation of $P_e(m|d_0)$ as given in (3.12). However, modelling of $I_{d_0,m}$ is not trivial since $I_{d_0,m} = (I_{d_0} - I_m)$ depends on many variables including the $(d_0, m)$-pair for TH-MPPM, the $\{C_j\}$-values for MCSK, and the CIR coefficients $\{h_{k,l}\}$, the path delay $\{\tau_{k,l}\}$, the user delay $\{\tilde{\tau}_k\}$ for $k = 1, \ldots, N_u$ for both modulations as given in (3.9). On the other hand, obtaining the system performance by simulation studies is not the best approach since many simulations should be conducted for the convergence of SER values.

One approach for the accurate modelling of MUI distributions is the *generalized* Gaussian distributions used in [66]. However, for an accurate SER expression, each channel realization should have its own GGD for modelling the MUI, which makes the SER evaluation computationally complex. With the motivation of providing an accurate and computationally efficient SER evaluation, some approximations are considered for GGDs in this chapter

when modelling the MUI distribution. Although GGDs will be used *ideally* in this section to model the MUI distributions for each channel realization in order to provide an accurate SER expression, approximations to MUI modelling will be made in Section 3.5 to yield the SER evaluation computationally efficient and yet accurate.

Modelling the MUI term with the GGD is a two-step procedure as proposed in [66]. For an accurate SER expression, MUI distributions are obtained individually for each channel realization. For that, $I_{d_0,m} = (I_{d_0} - I_m)$ is simulated using (3.9) for the given channel realization $\{h_{1,l}\}$ with various channel realizations and user delays of $N_u - 1$ interfering users for each $(d_0, m)$-pair or $\{C_j\}$-values depending on the modulation. The distribution of $I_{d_0,m}$ is then fitted into the GGD resulting in the pdf $f_{I_{d_0,m}}(x)$. The details of the modelling of $f_{I_{d_0,m}}(x)$ are presented in Appendix A. Once $f_{I_{d_0,m}}(x)$ is determined, the characteristic function (CF) method can be used to evaluate the error probability as in [15]. By calculating[4] the CF's of $I_{d_0,m}$ and $N_{d_0,m}$, and the deterministic value of $S_{d_0,m}$ for each channel realization, $P_e(m|d_0)$ can be accurately evaluated.

For the error probability evaluations of TH-MPPM and MCSK for each channel realization, let us rewrite $P_e(m|d_0)$ given in (3.12) as

$$P_e(m|d_0) = \Pr\Big[S_{d_0,m} + \Lambda_{d_0,m} < 0 \,\Big|\, d_0\Big] \tag{3.22}$$

where $\Lambda_{d_0,m} = I_{d_0,m} + N_{d_0,m}$. Due to the independence of the MUI and noise terms, the CF of $\Lambda_{d_0,m}$ can be expressed as

$$\Phi_{\Lambda_{d_0,m}}(\omega) = \Phi_{I_{d_0,m}}(\omega) \cdot \Phi_{N_{d_0,m}}(\omega) \tag{3.23}$$

where the CF's of the MUI and noise terms, respectively, are

$$\Phi_{I_{d_0,m}}(\omega) = \int_{-\infty}^{\infty} e^{j\omega x} \cdot f_{I_{d_0,m}}(x)\, dx = \sum_{n=0}^{\infty} \frac{(j\omega)^n}{n!} \mu_n \tag{3.24}$$

$$\Phi_{N_{d_0,m}}(\omega) = \int_{-\infty}^{\infty} e^{j\omega x} \cdot f_{N_{d_0,m}}(x)\, dx = e^{-\sigma^2_{N_{d_0,m}} \omega^2/2} \tag{3.25}$$

$$\text{with} \quad \sigma^2_{N_{d_0,m}} = \frac{N_s}{2E_s/N_0} \sum_{j=0}^{N_s-1} \sum_{l'_1,l'_2,l'_3} \big(h_{1,l'} - h_{1,(l'+(d_0-m))}\big)^2 \quad \text{for TH-MPPM}$$

$$\text{and} \quad \sigma^2_{N_{d_0,m}} = \frac{N_s}{2E_s/N_0} \sum_{j=0}^{N_s-1} \sum_{l'_1,l'_2,l'_3} \Big(h_{1,l'} - h_{1,(l'+C_j)}\Big)^2 \quad \text{for MCSK.}$$

[4]For MCSK, the terms $S_{d_0,m}$, $I_{d_0,m}$ and $N_{d_0,m}$ are functions of $\{C_j\}$. Accordingly, these terms should be associated with $\{C_j\}$ whenever MCSK is considered.

In (3.24), $\mu_n$ is the $n$th-order moment of the GGD [68], where the odd-order moments are zero due to the symmetrical distribution of a GGD around zero, and the even-order moments can be numerically calculated from (A.2). After taking the inverse transform of (3.23) as in [69], the cumulative distribution function of $\Lambda_{d_0,m}$ can be expressed as

$$F_{\Lambda_{d_0,m}}(x) = \frac{1}{2} + \frac{1}{\pi}\int_0^{\infty} \frac{\sin(x\omega)}{\omega}\Phi_{\Lambda_{d_0,m}}(\omega)\,d\omega. \tag{3.26}$$

For TH-MPPM, $P_e(m|d_0)$ depends on the unique $(d_0, m)$-pair and can be evaluated as

$$P_{e,MPPM}(m|d_0) = \Pr\left[S_{d_0,m} + \Lambda_{d_0,m} < 0 \,\middle|\, d_0\right] \;=\; 1 - F_{\Lambda_{d_0,m}}(S_{d_0,m}). \tag{3.27}$$

For MCSK, $P_e(m|d_0)$ depends on the pdf of $C_j$ given in (3.18) for each $(d_0, m)$-pair. Accordingly, $P_e(m|d_0)$ of MCSK can be evaluated as

$$\begin{aligned} P_{e,MCSK}(m|d_0) &= \Pr\left[S_{d_0,m}(\{C_j\}) + \Lambda_{d_0,m}(\{C_j\}) < 0 \,\middle|\, d_0\right] \\ &= \sum_{\substack{C_0=-(N_h+M-2)\\ C_0\neq 0}}^{N_h+M-2} \cdots \sum_{\substack{C_{N_s-1}=-(N_h+M-2)\\ C_{N_s-1}\neq 0}}^{N_h+M-2} \frac{(N_h+M-1)-|C_0|}{(N_h+M-1)\cdot(N_h+M-2)} \cdots \\ &\qquad \frac{(N_h+M-1)-|C_{N_s-1}|}{(N_h+M-1)\cdot(N_h+M-2)} \left[1 - F_{\Lambda_{d_0,m}(\{C_j\})}\left(S_{d_0,m}(\{C_j\})\right)\right] \end{aligned} \tag{3.28}$$

where $S_{d_0,m}(\{C_j\})$ and $F_{\Lambda_{d_0,m}(\{C_j\})}$ can be obtained from (3.8), (3.23)–(3.26). It should be noted that the multi-user case error probability expressions given in (3.27) and (3.28) become equal to the single-user case expressions given in (3.14) and (3.19) when $\Phi_{I_{d_0,m}}(\omega)$ in (3.24) is unity.

## 3.4 Realistic Rake Implementation

In Section 3.3, the $T_c$-spaced channel model and a Rake receiver with fingers placed ideally at the multiples of $T_c$ were considered for simplicity in analysis. In this section, it is aimed to present more accurate channel conditions and implementable receiver structures in order to provide more realistic system performances. For that, the $\tau$-spaced channel model with exact multipath arrival times and a Rake receiver implementation with fingers being separated by at least the chip time $T_c$ are considered. While the $\tau$-spaced channel model accounts for possible pulse overlapping that reduces the system performance, the Rake receiver implementation with fingers separated by at least the chip time approach tries to maximize the

collected energy. Here, a possible implementation of a Rake receiver is presented for known CIR coefficients $\{h_{1,l}\}$ in the accurate $\tau$-spaced channel model.

The simplest approach to a realistic Rake receiver implementation is to select the largest CIR coefficients that are separated by at least $T_c$ in a $\tau$-spaced channel model. Given the coefficients and multipath arrivals of $h_1(t)$, $\mathbf{H}_1 = \{h_{1,l} \,|\, l = 0, \ldots, L-1\}$ and $\mathbf{T}_1 = \{\tau_{1,l} \,|\, l = 0, \ldots, L-1\}$, the largest coefficients $\mathbf{H}_{1,max} = \{h_k \,|\, k = 0, \ldots, K-1\}$, $\mathbf{H}_{1,max} \subset \mathbf{H}_1$, and the corresponding arrival times $\mathbf{T}_{1,max} = \{\tau_k \,|\, k = 0, \ldots, K-1\}$, $K \leq L$, $\mathbf{T}_{1,max} \subset \mathbf{T}_1$, at least separated by $T_c$, can be found using the following procedure [60]:

1. Initialize $\tau_{1,-1} = 0$ and $k = 0$.
2. Define $\mathbf{T}'_1 = \{\tau_{1,l} \,|\, \tau_{1,l} \in [\tau_{1,k-1}, \tau_{1,k-1} + T_c]\}$.
3. Define $\mathbf{H}'_1 = \{h_{1,l} \,|\, l \in \mathbf{T}'_1\}$.
4. Find $\max\{|\mathbf{H}'_1|\} \Rightarrow h_{1,k}$, where $|\cdot|$ denotes absolute value.
5. Find the corresponding $\tau_{1,k}$.
6. $k = k + 1$; Go to Step 2 if $k \neq K$.

Here, $K$ is assumed to be the maximum number of fingers that can be obtained using the above procedure. Therefore, a Rake receiver using all $K$ fingers obtained by this procedure serves as an *implementable*[5] all-Rake receiver. On the other hand, fewer fingers can be used to implement partial-Rake or selective-Rake receivers, which are more desired for implementation since they are cost effective.

## 3.5 Results

In this section, initially the SER bounds for TH-MPPM and MCSK are validated in the approximate $T_c$-spaced channel model for the single-user case, followed by the system performance comparison in the accurate $\tau$-spaced channel model using the above Rake receiver implementation for line-of-sight (LOS) and non-LOS (NLOS) channel types (i.e., CM-1 and CM-3). In the second part, GGD is considered for modelling the MUI for the multi-user

[5]Since the realistic $\tau$-spaced channel model allows for pulse overlapping and the Rake fingers are separated by at least $T_c$, an all-Rake receiver considered here cannot collect all the signal energy.

case in order to verify the analysis in the $T_c$-spaced channel model, followed by the system performance comparison in the $\tau$-spaced channel model for more realistic results. In both numerical analysis and simulations, a second order Gaussian monocycle with pulse width $T_p = 0.6$ ns, chip time $T_c = 0.6$ ns, and frame times $T_f = 60$ ns and $T_f = 120$ ns, respectively, for the IEEE 802.15.3a CM-1 and CM-3 channel types [54] are considered. All the SER and bit-error rate (BER) performances are reported for fixed symbol energy $E_s$ to conform to FCC power limits.

### 3.5.1 Performances for the single-user case

In order to validate the analysis, SER bounds given in (3.13) are evaluated for TH-MPPM and MCSK in CM-1 by averaging over 1000 channel realizations and verified by simulations for different $N_s$ values when $L_p = 8$ Rake fingers are used. Maximum shift of MCSK is fixed to $(N_h + M - 2) = 31$ for different $M$ values, which control the value of $N_h$.

Initially, let us discuss the SER bounds plotted in Figs. 3.2 and 3.3. For 2PPM and 2CSK, the lower and upper bounds become the error probability $P_e$ due to $P_e(m|d_0)$ taking a single value for every $d_0$. For $\{4\text{PPM}, 8\text{PPM}\}$ and $\{4\text{CSK}, 8\text{CSK}\}$, the simulated performances approach the upper bound for medium and high SNR values. This can be explained by each $P_e(m|d_0)$ having almost independent contribution for the SER. Accordingly, the derived upper bound can be used to approximate the SER performances in the medium and high SNR regions. On the other hand, the lower bounds of TH-MPPM and MCSK, $\{M > 2\}$, are quite similar to the performances of 2PPM and 2CSK in the low and medium SNR regions, since the maximum $P_e(m|d_0)$ values that determine the lower bound are found to be similar to the $P_e(m|d_0)$ value of the binary modulations. For the illustration purpose, the lower bound of 4PPM is plotted for comparison to 2PPM in Fig 3.2.

In Figs. 3.2 and 3.3, it is also important to discuss the relative performances of TH-MPPM and MCSK. For this performance comparison, $N_s = \{1, 2, 4\}$ are considered. For every $N_s$ value, it is verified by simulations that MPPM does not have any performance improvement with increasing $N_s$, as also suggested by (3.17). On the other hand, MCSK improves its performance by increasing $N_s$ as the diversity gain increases with the combination of different CIR coefficients from different frame times. Here, the performances of TH-MPPM and MCSK are plotted for $N_s = 2$. It can be observed that MCSK provides 1-2 dB performance gain over MPPM when the SER range $[10^{-2}, 10^{-3}]$ is considered.

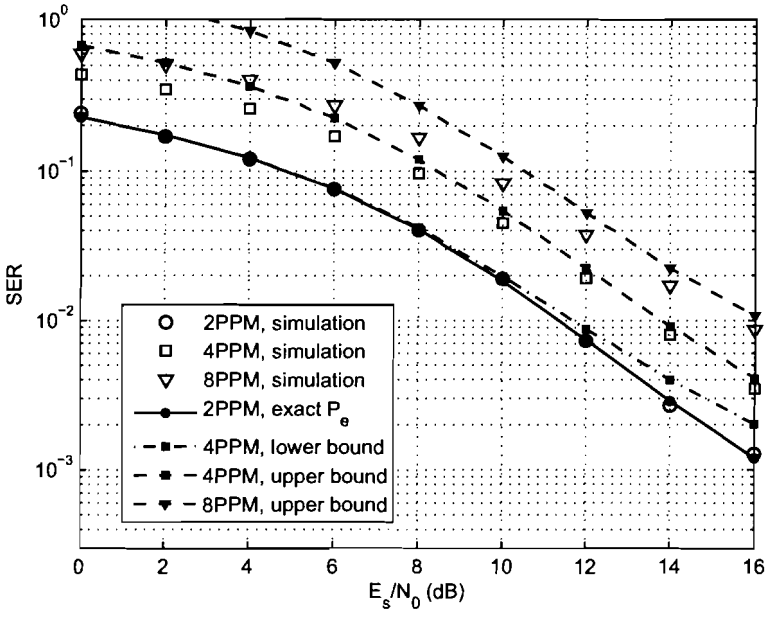


Figure 3.2: Bounds on the SER of TH-MPPM when $N_s = 2$.

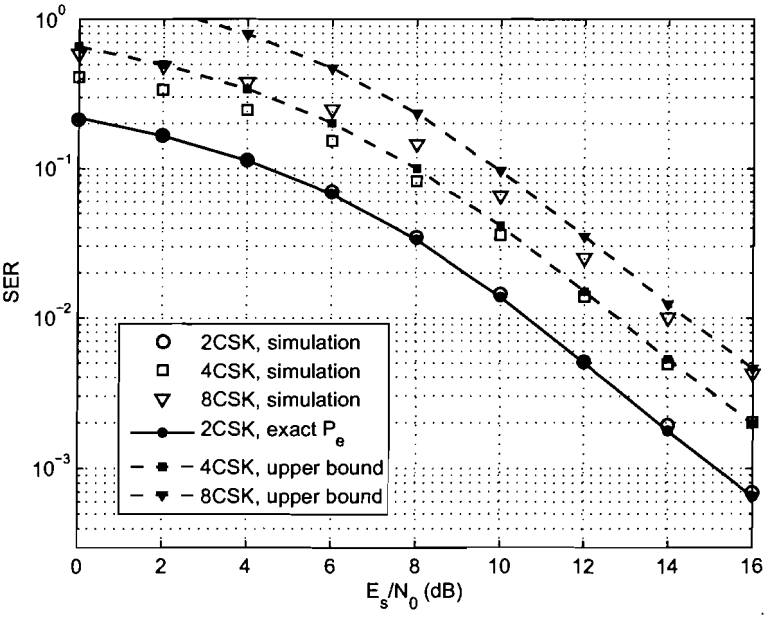


Figure 3.3: Bounds on the SER of MCSK when $N_s = 2$.

Another interesting point is that 2PPM becomes a special case of 2CSK when $(N_h + M - 2) = 1$ is substituted into (3.21). This is equivalent to 2PPM shifting the pulses only to $0^{th}$ and $1^{st}$ pulse locations. Accordingly, the performance of 2PPM is worse than the performance of 2CSK as also observed from the figures.

Next, the accurate $\tau$-spaced channel model is considered to provide more realistic performance results. In the simulation studies, it is assumed that the channel coefficients are perfectly estimated and the Rake fingers are separated by at least the chip time $T_c$. The locations of the Rake fingers are determined by the search algorithm presented in Section 3.4.

In Figs. 3.4 and 3.5, BER performances of TH-MPPM and MCSK are compared in CM-1 when all-Rake and partial-Rake ($L_p = 10$) receivers are considered, respectively, for $N_s = 2$. It can be observed that MCSK can provide about 1.5-2 dB performance gain over MPPM at BER $= 4 \cdot 10^{-4}$ for the all-Rake receiver and at BER $= 2 \cdot 10^{-3}$ for the partial-Rake receiver. When $N_s = 1$, while MPPM performs the same, it is observed that MCSK *slightly* decreases the performance gain to 1-1.5 dB. Accordingly, this performance gain is a result of *only* the randomizing effect, whereas the performance gain for $N_s > 1$ is determined by the diversity gain as well as the randomizing effect.

The performance gain reported in Fig. 3.5 is important since it is a result of a *practical* Rake receiver implementation. First of all, the channel model assumes the exact arrival of multipaths, and hence, there may be pulse overlaps, which is a realistic condition. Secondly, the Rake fingers are separated by at least the chip time, which is an implementable structure. Lastly, limited number of Rake fingers are considered, which is cost effective. Therefore, the performance gain reported in Fig. 3.5 is important from the practical aspects of TH-MPPM and MCSK comparison.

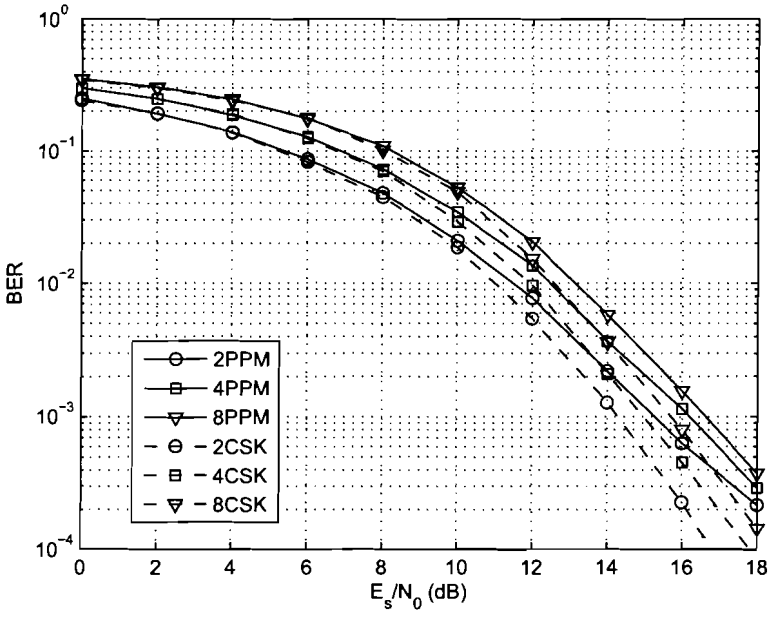


Figure 3.4: Performances of TH-MPPM and MCSK for practical implementation of an all-Rake receiver in the accurate $\tau$-spaced channel for CM-1.

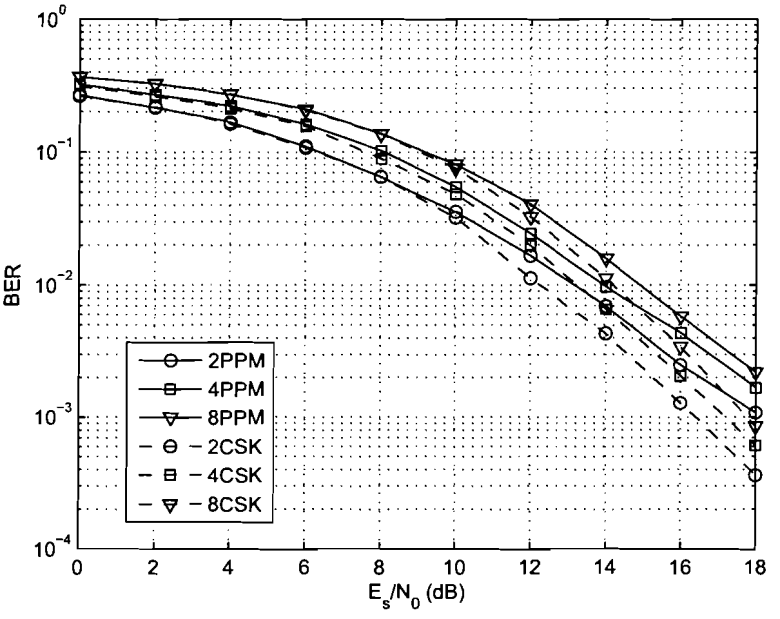


Figure 3.5: Performances of TH-MPPM and MCSK for practical implementation of a partial-Rake receiver with $L_p = 10$ fingers in the accurate $\tau$-spaced channel for CM-1.

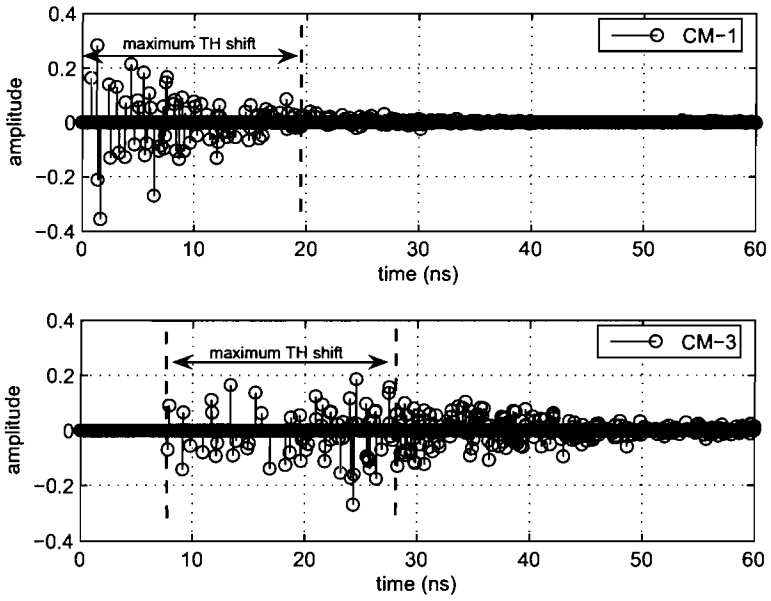


Figure 3.6: CIR coefficients in CM-1 and CM-3 channel types.

After the LOS CM-1 channel type, system performances are also compared in the NLOS CM-3 channel type. Before comparing the performances, it is important to compare the CIRs of CM-1 and CM-3 as plotted in Fig. 3.6. As illustrated in the plotted channel realizations, power delay profile of CM-1 decays faster than that of CM-3. Accordingly, for the maximum TH shift considered for MCSK ($\approx$ 19 ns) in this study, CIR coefficients in CM-1 become very small for the maximum distance. Hence, when the pulses are transmitted at significantly separated locations,[6] the decision variables are less affected by the multipath delays. This has resulted in 1-2 dB performance gain over MPPM as reported in the previous figures. When a CM-3 channel type is considered, the CIR coefficients are still significant even at the maximum separation. Accordingly, the system performance of MCSK is not expected to benefit from pulse location randomization. However, diversity gain achieved by combining different pulse locations for $N_s > 1$ may increase the performance.

[6]If the pulses were *continuously* transmitted at maximum separated locations, although the system performance could have improved, the PSD would have spectral components due to limited TH randomization that would violate the FCC spectral mask [67]. MCSK that transmits at randomized pulse locations eliminates this problem.

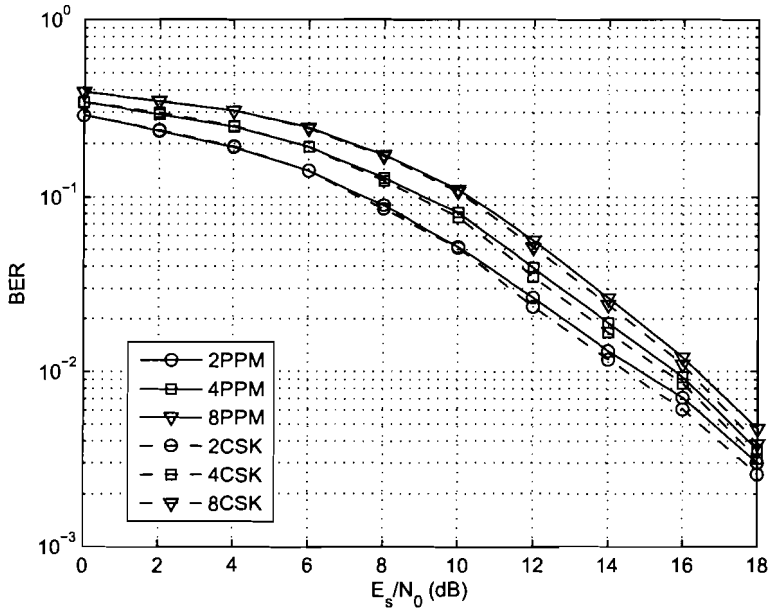


Figure 3.7: Performances of TH-MPPM and MCSK for practical implementation of a partial-Rake receiver with $L_p = 20$ fingers in the accurate $\tau$-spaced channel for CM-3.

In Fig. 3.7, BER performances of TH-MPPM and MCSK are compared in CM-3 when a partial-Rake ($L_p = 20$) receiver is considered for $N_s = 2$. It can be observed that MCSK provides about 0.2–0.5 dB performance gain at BER $= 10^{-2}$. When $N_s = 1$, TH-MPPM and MCSK perform almost the same, showing that the MCSK performance does not benefit from pulse location randomization in the slowly decaying power delay profile of CM-3. Accordingly, the performance gain provided by $N_s = 2$ is a net result of the diversity gain as mentioned in the previous paragraph.

### 3.5.2 Performances for the multi-user case

In order to evaluate the multi-user case analysis, 2PPM is considered as a special case of 2CSK, where the SER bounds for {4PPM, 8PPM} can be found similarly. The SER of MCSK can also be evaluated similarly by considering different $N_h$ values following the detailed example of 2PPM. Here, some assumptions and approximations are provided to yield the analysis evaluation computationally efficient.

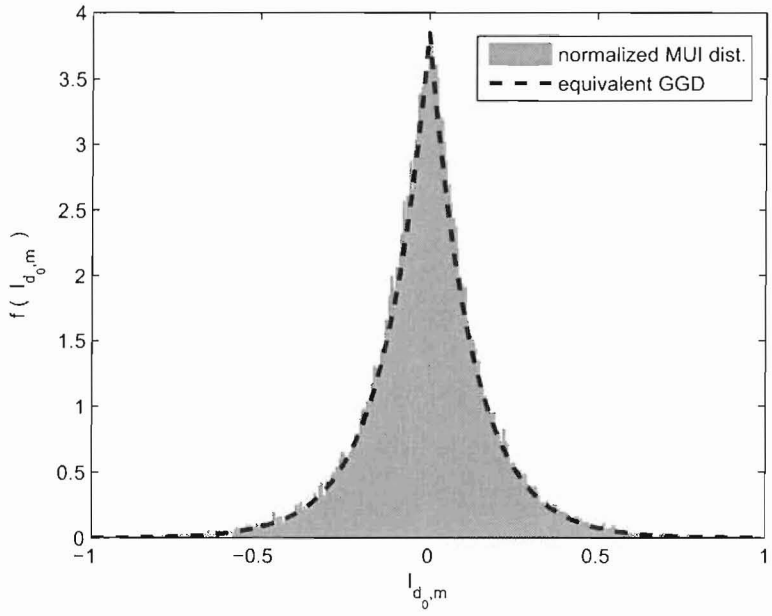


Figure 3.8: The MUI distribution obtained by simulations and its equivalent generalized Gaussian distribution.

For the *exact* evaluation of $P_e(m|d_0)$ in (3.27), initially the GGD of the MUI, $f_{I_{d_0,m}}(x)$, should be obtained for each channel realization and $(d_0, m)$-pair. It is important that each channel realization should have its own GGD since the values of $S_{d_0,m}$ and $N_{d_0,m}$ change with channel realizations. However, this requires many simulations. Therefore, it is assumed that a single MUI distribution is obtained by simulating (3.9) over *various* channel realizations for the first-order approximation. In Fig. 3.8, the MUI distribution of $N_u - 1 = 7$ interfering users obtained over 1000 channel realizations and its equivalent GGD $f_{I_{d_0,m}}(x)$ are plotted for $(d_0 = 0, m = 1)$. The MUI distribution for $(d_0 = 1, m = 0)$ is also found to be well in accordance with the same GGD. The MUI distribution and its associated GGD can be computed as outlined in Appendix A. Using the single distribution of $f_{I_{d_0,m}}(x)$ in (3.24), $P_e(m|d_0)$ in (3.27) can be evaluated over different channel realizations.

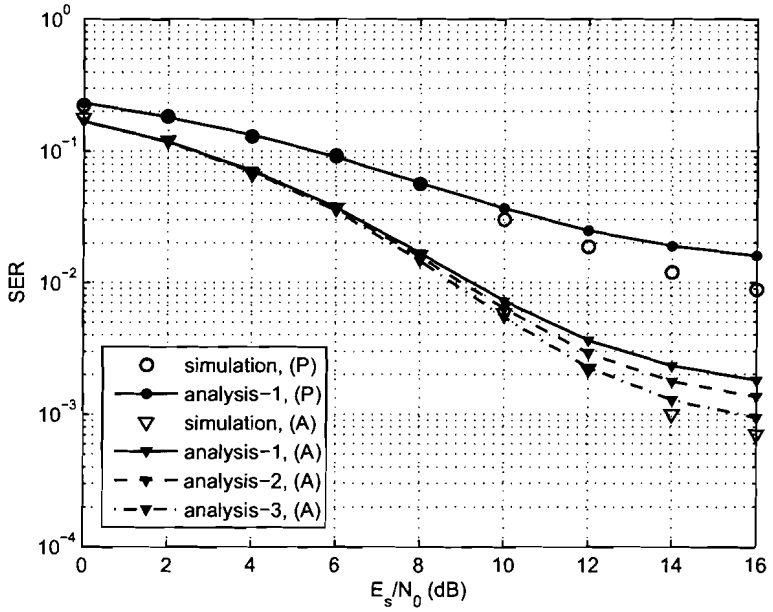


Figure 3.9: SER evaluation in the presence of $N_u - 1 = 7$ interfering users that are modelled by GGD.

In Fig. 3.9, numerical values for SER are compared to the simulation values for partial-Rake and all-Rake receivers. Here, analysis-1 refers to the calculation of $P_e(m|d_0)$ using the first-order approximation that considers only a single GGD, which is different for partial-Rake and all-Rake. It can be observed that the numerical values for analysis-1 deviate (perform worse) from the simulation values for the medium and high SNR regions. This is mainly due to using a *single* MUI distribution even for small $S_{d_0,m}$ values resulting from different channel realizations. This reason can be better understood by observing the distribution of $S_{d_0,m}$ values for an all-Rake receiver plotted for 1000 channel realizations in Fig. 3.10. It is observed that $S_{d_0,m}$ takes values in the range $[0.4, 1.6]$. Accordingly, for the case when $S_{d_0,m} \approx 0.4$, the averaged single MUI distribution plotted in Fig. 3.8 will cause overestimated interference, and the evaluated error probability will be worse than the simulation values as the worse-case errors dominate the performance.

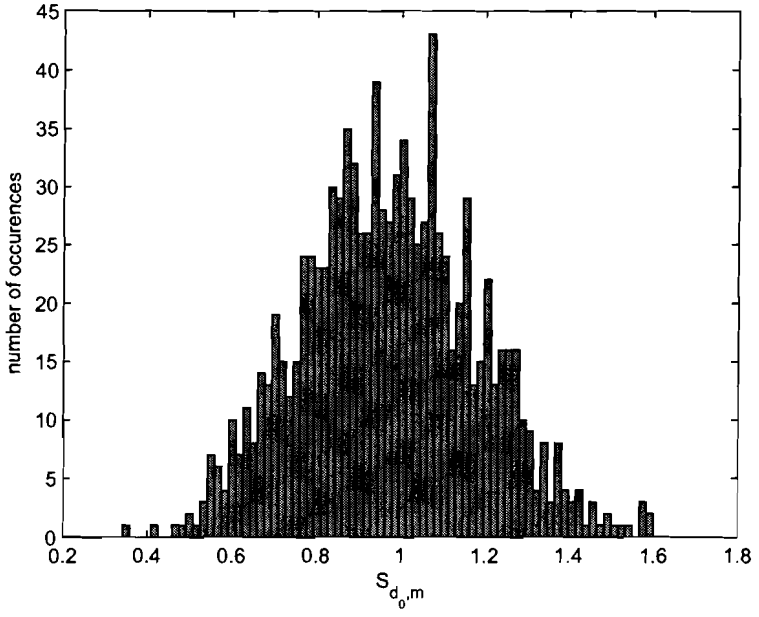


Figure 3.10: $S_{d_0,m}$ values obtained from different channel realizations.

By increasing the number of GGDs in the evaluation of $P_e(m|d_0)$, more accurate results can be obtained. Considering the range of $S_{d_0,m}$ values for the all-Rake given in Fig. 3.10, more GGDs are considered for the error probability evaluation as the second-order approximation. For analysis-2 (using 2 GGDs) and analysis-3 (using 4 GGDs), channel realizations that result in $S_{d_0,m} \approx \{0.8, 1.2\}$ and $S_{d_0,m} \approx \{0.4, 0.8, 1.2, 1.6\}$ are used in determining the independent MUI distributions, respectively. For the evaluation of (3.27), a quantization is made for each $S_{d_0,m}$ value to find the corresponding GGD to be used in each channel realization. With more GGDs, the accuracy of the approximation can be increased at the expense of more computation. In Fig. 3.9, it can be observed that the SER performance approximation becomes better with increasing number of GGDs. Even with four GGDs representing the MUI distribution, the evaluation of the semi-analytical SER expression results in values converging to simulation values. This evaluation is computationally more efficient than the simulation study since a set of channel realizations is used only *once* to get the noise-free MUI distributions to be evaluated at each SNR value, whereas the same set of channel realizations is *repeated* for each SNR value for the simulation study, which

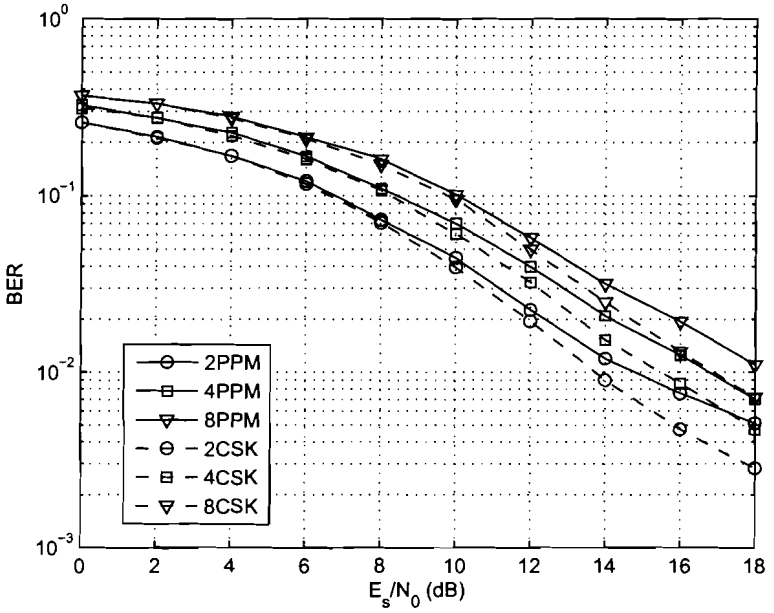


Figure 3.11: Performances of TH-MPPM and MCSK for practical implementation of a partial-Rake receiver with $L_p = 10$ fingers in the accurate $\tau$-spaced channel for CM-1 when $N_u = 8$ users are present.

significantly increases the computation time.

Although the SER approximation of the multi-user case is presented here for 2PPM, i.e., the special case of 2CSK, the multi-user case SER of MCSK can be evaluated similarly by considering different $\{C_j\}$ values and making similar approximations.

Next, the accurate $\tau$-spaced channel model is considered to provide more realistic performance results. In Fig. 3.11, BER performances of TH-MPPM and MCSK are compared in CM-1 for a partial-Rake ($L_p = 10$) receiver when $N_s = 2$ and $N_u = 8$. It can be observed that MCSK can provide about 1.5-2 dB performance gain over MPPM for the BER range $[10^{-2}, 5 \cdot 10^{-3}]$. When $N_s = 1$, it is observed that the performance gain is slightly reduced while the overall system performances of TH-MPPM and MCSK are degraded about 2 dB. Accordingly, the performance gain achieved by MCSK for $N_s = 1$ is mainly due to randomizing pulse transmit locations, whereas the increased performance gain for $N_s = 2$ is

due to both randomization and the diversity gain. While both TH-MPPM and MCSK significantly improve their performances with increasing $N_s$ in the presence of multiple users, MCSK also benefits from diversity gain, which additionally increases its performance gain over TH-MPPM as suggested by this study.

## 3.6 Conclusion

In this chapter, MCSK impulse modulation was proposed and studied, where it randomized the consecutive pulse transmit locations of the conventional TH-MPPM in order to reduce the effect of multipath delays on the decision variables. For that, lower and upper bounds on the SER were derived in the commonly used approximate $T_c$-spaced channel model for both single- and multi-user cases, and simulation studies were conducted in the accurate $\tau$-spaced channel models. For the single-user case, the effect of multipath-delayed pulses on $M$ decision variables was explicitly provided in terms of channel impulse response coefficients. For the multi-user case, an accurate semi-analytic SER expression was derived based on modelling the MUI terms with the GGD, where some approximations to MUI modelling were made that increased the computational efficiency of numerical analysis significantly with respect to the simulation studies, while still providing accurate results. For the performance comparison, the effects of CM-1 and CM-3 channel types and the pulse repetition number $N_s$ on the system performances were discussed in detail. Most importantly, the study shows that for the *practical* implementations of MCSK and TH-MPPM, MCSK can provide about 2 dB performance gain over MPPM as it reduces the effects of multipath delays on the decision variables by randomizing pulse transmit locations.

# Chapter 4

# MCSK Combined with BPPM

In the previous chapter, $M$-ary code shift keying (MCSK) impulse modulation was proposed and compared to time-hopping $M$-ary pulse position modulation (TH-MPPM), the conventional high order ultra wideband impulse radio (UWB-IR) modulation. It was shown that MCSK can provide about 2 dB performance gain over TH-MPPM in a multipath channel. Since TH binary PPM (TH-BPPM) is the benchmark modulation format in UWB-IR communications and that many modulations are proposed to increase its data rate and improve its performance, it is also necessary to compare MCSK with TH-BPPM. In this chapter, a novel hybrid modulation format based on MCSK, namely MCSK/BPPM, is proposed for comparison to TH-BPPM as the second main contribution of this dissertation.[1]

## 4.1 Introduction

In UWB-IR communications, in order to achieve high-rate data communications in the order of a few hundred MHz, the most commonly considered modulation scheme is the TH-BPPM format [7]. Due to the demand for higher data rates in the order of a few GHz, some alternative modulation formats have been proposed including the design of different pulses and the $M$-ary pulse position modulation so as to increase the data rate. In Section 2.1.2, implementation disadvantages of the pulse shape modulation (PSM) were summarized. These disadvantages include the data rate being dependent on the number and complexity of different circuits that generate orthogonal pulses, the necessity for different

[1] The material presented here is a combination of the works published in [70] and [71].

antenna structures, and the possibility of violating the spectral mask. In Chapter 3, TH-MPPM was studied. It was shown that the energy captured from consecutive pulse locations in MPPM could be interfered by a large portion of the multipath-delayed received pulses, which may generate noticeable interference components for the $M$ decision variables, hence affecting the system performance.

$M$-ary code shift keying was proposed in the previous chapter as an improvement to MPPM that suffers from self-interference due to consecutive pulse locations used. Since data transmission in MCSK is achieved through selecting one of the $M$ TH codes, there is flexibility in further increasing its data rate by combining it with either BPPM or binary pulse amplitude modulation (BPAM). The employment of MCSK is considered here only for BPPM in order to increase the data rate of the most commonly used conventional TH-BPPM format. MCSK employed for BPPM exhibits the characteristics of not affecting pulse shaping unlike [19] and improving the spectrum characteristics with respect to the conventional TH-BPPM [40], while increasing the data rate [70]. This is achieved by transmitting additional data embedded in user-specific TH codes while using BPPM.

This new signalling scheme, named combined MCSK/BPPM, uses one of the $M$ TH codes to additionally transmit $\log_2 M$ bits with respect to TH-BPPM. The transmitted data is detected at the receiver by performing $M$ correlations followed by the maximum-likelihood sequence estimation (MLSE), resulting in a modest increase in receiver complexity. The additional data is detected by choosing the TH code that gives a maximum correlation at the receiver. The proposed system shows better bit-error-rate (BER) performance than the conventional TH-BPPM system with increased information rate, if the system parameters are properly selected. While this result can be used for high-rate applications (e.g., IEEE 802.15.3a), it can also be used to improve the ranging and location capability of conventional TH-PPM systems, which is highly desired for low-rate applications (e.g., IEEE 802.15.4a). This can be achieved by increasing the frame time with fixed data rate that allows to mitigate the worse effects of multipath and multiple access interference, providing more accurate time-of-arrival estimation.

The rest of the chapter is organized as follows. In Section 4.2, the proposed MCSK/BPPM modulation system is described, and the system design parameters are explained in detail. The MCSK/BPPM system is analyzed in Section 4.3 in terms of the symbol-error rate (SER), where the upper and lower bounds on the SER are derived. In Section 4.4, numerical and simulation results are presented to verify the theoretical SER analysis, and

to show the advantages of the proposed system over the conventional TH-BPPM system. The concluding remarks are given in Section 4.5.

## 4.2 System Model

MCSK/BPPM shows a similar signal model structure with respect to the conventional TH-BPPM, therefore initially the signal model of the conventional TH-BPPM is given. The signal that transmits the $i$th bit of the $k$th user using the conventional TH-BPPM can be modeled as

$$s^{(k)}(t) = \sqrt{\frac{E_b}{N_s}} \sum_{j=(i-1)N_s}^{iN_s-1} w\Big(t - jT_f - c_j^{(k)}T_c - d_i{}^{(k)}\delta_d\Big) \tag{4.1}$$

where $w(t)$ denotes the transmitted pulse, which includes the effects of transmitting and receiving antennas, with unit energy and pulse width $T_p$. The other system parameters are explained in detail after (2.2). Here, the chip time $T_c > T_p + \delta_d$ is selected to allow for orthogonal time-hopping locations. Using this modulation format, every $N_sT_f$ seconds one-bit data is transmitted, where the information rate is given by $R_b = 1/N_sT_f$.

The proposed MCSK/BPPM considers more than one user-specific TH code for each user such that the conventional TH-BPPM code $\{c^{(k)}\}$ takes the form $\{c_n^{(k)}\}$, where $\{n = 0, \ldots, M-1\}$ and $\log_2 M$ is an integer. While one-bit data is being transmitted using BPPM, additional $\log_2 M$-bit data selects a particular TH code from the set of $M$ user-specific TH codes, which is the $M$-ary CSK. For $N_p/N_s > 1$, the same TH code is used until $N_p$ pulses are transmitted. This means that the BPPM effectively transmits $N_p/N_s$ bits[2] using the TH code chosen by $\log_2 M$-bit data. Hence, using the proposed MCSK/BPPM a total of $(\log_2 M + N_p/N_s)$ bits are transmitted for the duration of $(N_p/N_s)$ bits transmitted using the conventional TH-BPPM. This results in the increased information rate given as

$$R_s = \left(1 + \frac{\log_2 M}{(N_p/N_s)}\right) R_b. \tag{4.2}$$

The modulation format that can achieve the increased information rate given in (4.2) transmits the $k$th user's one set of bits (one symbol) using the signal model

$$s^{(k)}(t) = \sqrt{\frac{E_b}{N_s}} \sum_{i=1}^{N_p/N_s} \sum_{j=(i-1)N_s}^{iN_s-1} w\Big(t - jT_f - (c_n^{(k)})_jT_c - d_i{}^{(k)}\delta_d\Big) \tag{4.3}$$

[2]For simplicity, we assume $N_p/N_s$ to be an integer.

where $E_b$ is the energy of one bit modulated by BPPM for the duration $N_sT_f$, $\{c_n^{(k)}\}$ is the $k$th user's $n$th TH code and $N_p/N_s$ is the number of bits transmitted using BPPM for the duration of $\{c_n^{(k)}\}$. The signal structure given in (4.3) differs from (4.1) by:
(i) transmitting the bits using one of the $M$ TH codes, and
(ii) transmitting $N_p/N_s$ bits using the same TH code.
These differences between MCSK/BPPM and TH-BPPM are explained as follows:

*(i) Designing M TH codes per user:* The information rate increase of the proposed scheme is based on the increased number of TH codes per user. Therefore, the TH codes should be carefully designed to minimize the performance loss while increasing the information rate. The TH codes are designed such that $\{\mathbf{c}^{(k)}\}$'s are generated independently for $\{k = 1, ..., N_u\}$, where $\{\mathbf{c}^{(k)} \supset \{\mathbf{c}_0^{(k)}, \ldots, \mathbf{c}_{M-1}^{(k)}\}\}$, $N_u$ is the number of users and $M$ is the number of TH codes per user. For each user $k$, TH codes should also satisfy $\{(c_0^{(k)})_j \neq \ldots \neq (c_{M-1}^{(k)})_j, \forall j\}$, where $\mathbf{c}_n^{(k)} = \{(c_n^{(k)})_0, \ldots, (c_n^{(k)})_{N_p-1}\}$, $\{0 \leq (c_n^{(k)})_j < N_h, \forall n, \forall j\}$ and $N_h \geq M$. This condition is the key design constraint that generates orthogonal TH codes and ensures that each user's TH codes do not overlap within a frame time $T_f$, which improves the system performance. Based on these conditions, a decimal maximal-length sequence $\mathbf{S}_d$ is assigned to the TH codes, which can be generated using shift registers that produce a binary maximal-length sequence $\mathbf{S}_b$ [72], [73], where $\mathbf{S}_d = [s_1 \ldots s_{L_s}]$, $\mathbf{S}_b = [b_1 \ldots b_{(l \cdot L_s)}]$, $L_s$ is the length of the decimal maximal-length sequence, $l = \log_2 N_h$ is an integer, $(s_i)_{10} = (b_{l(i-1)+1} \cdots b_{l(i-1)+l})_2$, $b_i \in \{0, 1\}$ and $(\cdot)_x$ indicates base $x$.

*(ii) Transmit algorithm:* In MCSK/BPPM, $N_p/N_s$ bits are transmitted using the same TH code selected by $\log_2 M$-bit data. The signal transmit structure for the $k$th user's one-symbol is shown in Fig. 4.1 and the transmit algorithm is given as follows. Let $\mathbf{B}^{(k)} = \{d_i^{(k)} | i = 1, \ldots, (N_p/N_s) + \log_2 M\}$, $d_i^{(k)} \in \{0, 1\}$ represent the set of bits (i.e., the symbol) to be transmitted using the proposed modulation. Let $\mathbf{T}^{(k)} \subset \mathbf{B}^{(k)}$ and $\mathbf{C}^{(k)} \subset \mathbf{B}^{(k)}$, where $\mathbf{T}^{(k)} = \{d_1^{(k)}, \ldots, d_{(N_p/N_s)}^{(k)}\}$ is the set of bits to be transmitted using BPPM, and $\mathbf{C}^{(k)} = \{d_{(N_p/N_s)+1}^{(k)}, \ldots, d_{(N_p/N_s)+\log_2 M}^{(k)}\}$ is the input to MCSK to determine the index $n$ of the user-specific TH code $\mathbf{c}_n^{(k)}$. The relation between $n$ and $\mathbf{C}$ is given by

$$(n)_{10} = \left(d_{(N_p/N_s)+1}\, d_{(N_p/N_s)+2} \cdots d_{(N_p/N_s)+\log_2 M}\right)_2. \tag{4.4}$$

Once the TH code $\mathbf{c}_n^{(k)}$ is determined by the set $\mathbf{C}^{(k)}$, all the bits in the set $\mathbf{T}^{(k)}$ are transmitted with BPPM using the same TH code as expressed in (4.3). This process is repeated for all data blocks (i.e., symbols).

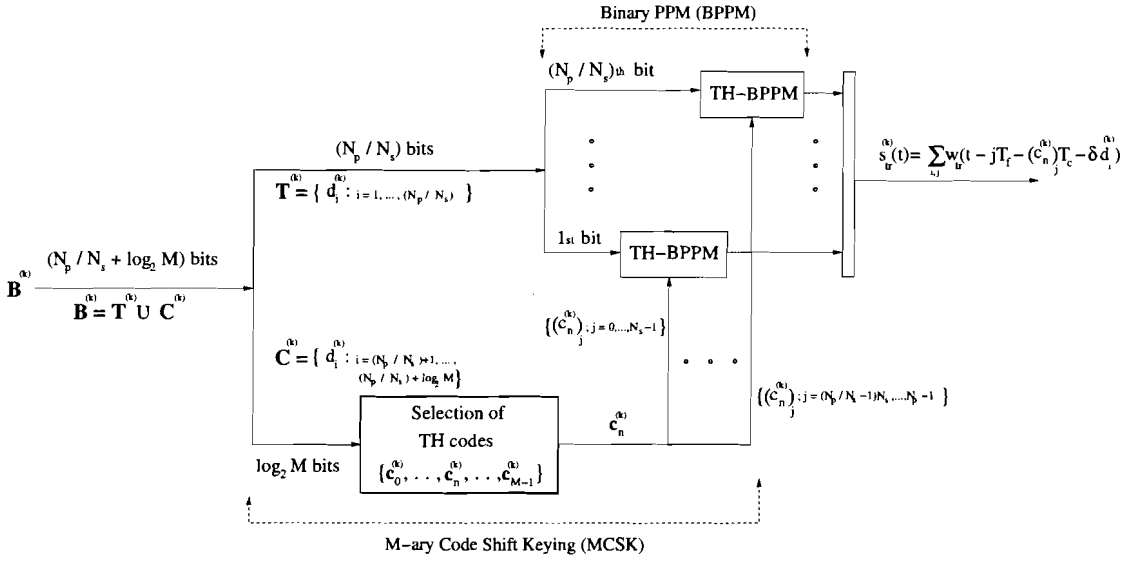


Figure 4.1: Proposed MCSK/BPPM modulation format for the $k$th user.

For a multiple-access system consisting of $N_u$ users, the received signal $r(t)$ at the output of the receive antenna can be modeled as

$$r(t) = \sum_{k=1}^{N_u} A_k \tilde{s}^{(k)}(t - \tilde{\tau}_k) + n(t) \tag{4.5}$$

where $n(t)$ is the additive white Gaussian noise (AWGN) with two-sided power spectral density $N_0/2$, $A_k$ is the channel attenuation parameter, $\tilde{\tau}_k$ is the time asynchronism between the users, and $\tilde{s}^{(k)}(t)$ is the signal received from the $k$th transmitter. $\tilde{s}^{(k)}(t)$ results from the waveform at the output of the receive antenna $s^{(k)}(t)$ being distorted by the channel $h_k(t)$ and is represented as

$$\tilde{s}^{(k)}(t) = s^{(k)}(t) \otimes h_k(t) \tag{4.6}$$

where $s^{(k)}(t)$ consists of received pulse shapes $w(t)$ and $\otimes$ is the convolution operator. $h_k(t)$ is the $k$th user's channel impulse response [56]

$$h_k(t) = \sum_{l=0}^{L-1} h_{k,l}\delta(t - \tau_{k,l}) \tag{4.7}$$

with the assumptions $\sum_{l=0}^{L-1} h_{k,l}^2 = 1$, $\forall k$ to remove the path loss effect, and $\{\tau_{k,l} \in nT_c\}$,

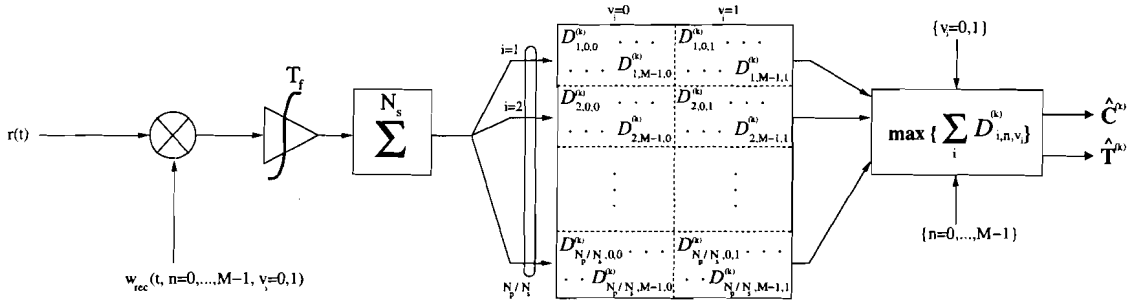


Figure 4.2: Receiver structure for the $k$th user.

where $n \geq 0$ is an integer, for simplicity in channel representation (i.e., $T_c$-spaced channel model). Here, $h_{k,l}$ is the $k$th channel's $l$th multipath coefficient, $\tau_{k,l}$ is the delay of the $k$th channel's $l$th multipath component and $\delta(\cdot)$ is the Dirac delta function. To note, the path delay $\tau_{k,l}$ is distinguished from the user delay $\tilde{\tau}_k$ by the sign "~".

As in agreement with previous works [7], the received pulse $w(t)$ is assumed to be the second derivative of a Gaussian monocycle given by

$$w(t) = \left[1 - 4\pi\left(\frac{t}{\tau_m}\right)^2\right] \exp\left[-2\pi\left(\frac{t}{\tau_m}\right)^2\right] \tag{4.8}$$

where $\tau_m = 0.2877ns$. Accordingly, $\delta_d = 0.15\,ns$ is chosen in order to maximize the performance of the conventional TH-BPPM [7].

The transmitted data of a single user $k$ can be recovered at the receiver using the optimum single-user receiver structure shown in Fig. 4.2 (illustrated for an AWGN channel), which consists of a single correlation receiver and a post-processing stage. At the receiver, the received signal $r(t)$ is correlated with the template signal $w(t)$ at each chip time determined by $M$ TH codes for both values of the binary data. In the presence of multipath fading, Rake receivers consisting of multiple correlators (fingers) are employed at locations separated by at least the chip time $T_c$ [74], where the correlator outputs are weighted by the multipath coefficients to form the decision statics. Assuming perfect synchronization between the $k$th user's transmitter and receiver, the correlator output statistics $\{D^{(k)}_{i,n,v_i}\}$

for the BPPM modulated $i$th bit transmitted in a multipath channel are computed as

$$D_{i,n,v_i}^{(k)} = \sqrt{\frac{N_s}{E_b}} \sum_{j=(i-1)N_s}^{iN_s-1} \sum_{l=0}^{L_p-1} h_{k,l} \int_{jT_f+\tilde{\tau}_k}^{(j+1)T_f+\tilde{\tau}_k} r(t) \times w\Big(t - \tilde{\tau}_k - \tau_{k,l} - jT_f - (c_n^{(k)})_j T_c - v_i\delta_d\Big)\, dt \quad (4.9)$$

for $\{n = 0, \ldots, M-1;\ v_i = 0, 1\}$ resulting in $2M$ values, where $L_p$ is the number of fingers used in the partial-Rake receiver. For a symbol of length $(N_p/N_s + \log_2 M)$ bits, $\{D_{i,n,v_i}^{(k)}\}$ is calculated for $\{i = 1, \ldots, N_p/N_s\}$ that results in $2M$ correlation output values for each of the $N_p/N_s$ bits transmitted using BPPM. $\{D_{i,n,v_i}^{(k)}\}$'s are then used to calculate the symbol decision statistics

$$L^{(k)}(n, \mathbf{v}) = \sum_{i=1}^{N_p/N_s} D_{i,n,v_i}^{(k)} \quad (4.10)$$

where $\{n = 0, \ldots, M-1\}$ and $\mathbf{v} = [v_1\, v_2 \ldots v_{(N_p/N_s)}]$, $v_i \in \{0, 1\}$ with $\left(2^{(N_p/N_s)}M\right)$ number of output values. This is equivalent to finding all possible (i.e., $2^{(N_p/N_s)}$) combinations of BPPM transmitted sequence for each of the user-specific TH code (i.e., $M$ times). The transmitted sets $\mathbf{T}^{(k)}$ and $\mathbf{C}^{(k)}$ are estimated by choosing

$$\begin{aligned} \max\left\{L^{(k)}(n, \mathbf{v})\right\} &\Rightarrow n \Rightarrow \hat{\mathbf{C}}^{(k)}, \\ &\Rightarrow \mathbf{v} \Rightarrow \hat{\mathbf{T}}^{(k)}, \\ &\Rightarrow [\hat{\mathbf{T}}^{(k)} | \hat{\mathbf{C}}^{(k)}] \Rightarrow \hat{\mathbf{B}}^{(k)}. \end{aligned} \quad (4.11)$$

## 4.3 Analysis of the Symbol-Error Rate

The performance analysis of the proposed MCSK/BPPM is based on the symbol decision statistics $\{L^{(k)}(n, \mathbf{v})\}$, which are formed by the correlator output statistics $\{D_{i,n,v_i}^{(k)}\}$. In this section, we analyze the correlator output statistics, followed by the SER analysis of the proposed system, where we assume the multipath coefficients to be $\{h_{k,0} = 1,\ \tau_{k,0} = 0,\ h_{k,l} = 0,\ l \neq 0, \forall k\}$, i.e., an AWGN channel, for convenience. In Section 4.4, MCSK/BPPM system performances will be reported for both AWGN and multipath fading channels.

Let $d_i^{(1)}$ be the first user's $i$th bit transmitted using the TH code $\mathbf{c}_0^{(1)}$ without loss of generality. For the $i$th bit interval, each of the $M$ TH codes in first user's receiver produces

two output values $D^{(1)}_{i,n,v_i}$ for $v_i \in \{0,1\}$, given $\{n = 0,\ldots,M-1\}$. Substituting (4.5) into (4.9) yields

$$D^{(1)}_{i,n,v_i} = S_{i,n,v_i} + I_{i,n,v_i} + \eta_{i,n,v_i} \tag{4.12}$$

where $S_{i,n,v_i}$ is the desired signal output, given by

$$S_{i,n,v_i} = A_1 \sum_{j=(i-1)N_s}^{iN_s-1} R\Big([(c_0^{(1)})_j - (c_n^{(1)})_j]T_c + [d_i^{(1)} - v_i]\delta_d\Big) \tag{4.13}$$

with $R(x) = \int_{-\infty}^{\infty} w(t-x)w(t)dt$ being the autocorrelation function of $w(t)$, $I_{i,n,v_i}$ denotes the multi-user interference (MUI) caused by other user signals, given by

$$I_{i,n,v_i} = \sqrt{\frac{N_s}{E_b}} \sum_{k=2}^{N_u} \sum_{j=(i-1)N_s}^{iN_s-1} \int_{jT_f+\tau_1}^{(j+1)T_f+\tau_1} A_k s^{(k)}(t-\tau_k) \times w\Big(t - \tau_1 - jT_f - (c_n^{(1)})_j T_c - v_i\delta_d\Big)dt, \tag{4.14}$$

and $\eta_{i,n,v_i}$ is the channel noise output. Note that $\eta_{i,n,v_i}$ is zero-mean Gaussian with variance $\sigma^2_{\eta_{i,n,v_i}} = \frac{N_0}{2E_b}N_s^2R(0)$. For the same $n$, $\eta_{i,n,v_i}$ and $\eta_{i,n,v_i'}$ are correlated, and their difference has a variance $\sigma^2_{\{\eta_{i,n,v_i}-\eta_{i,n,v_i'}\}} = \frac{N_0}{E_b}N_s^2[R(0) - R(\delta_d)]$ where $v_i' = |v_i - 1|$.

Using the time asynchronism model in [7] and the interference model in [15] that accounts for the bit change of the interfering signal during the transmission of $d_i^{(1)}$, we simplify the MUI $I_{i,n,v_i}$ in (4.14) and rewrite it in terms of $R(.)$ as

$$I_{i,n,v_i} = \sum_{k=2}^{N_u} A_k \Bigg[ \sum_{j=(i-1)N_s}^{(i-1)N_s+\gamma_k-1} R\Big(\alpha_k + [(c_{m_i}^{(k)})_j - (c_n^{(1)})_j]T_c + [d_i^{(k)} - v_i]\delta_d\Big) + \sum_{j=(i-1)N_s+\gamma_k}^{iN_s-1} R\Big(\alpha_k + [(c_{l_{(i+1)}}^{(k)})_j - (c_n^{(1)})_j]T_c + [d_{(i+1)}^{(k)} - v_i]\delta_d\Big) \Bigg] \tag{4.15}$$

where $d_i^{(k)}$ and $d_{(i+1)}^{(k)}$ represent two adjacent bits of the $k$th user that overlap with the transmission time of $d_i^{(1)}$, $\{c_{m_i}^{(k)}\}$ represents the $k$th user's $m$th TH code used in transmitting the $i$th bit and $\{c_l^{(k)}\}$ may or may not be same TH code as $\{c_m^{(k)}\}$, $\gamma_k$ is the index of the frame time that the bit change occurs and uniformly distributed over $[0, N_s - 1]$, and $\alpha_k = (\tau_k - \tau_1 - j_kT_f)$ is due to user asynchronism [7, eq. (55)] ($j_k$ is the value of the time difference rounded to the nearest frame time) and uniformly distributed over $[-T_f/2, T_f/2]$. It should be noted that the MUI in (4.15) is modeled with all the TH codes having the

same index, for simplicity. This assumption is valid if the TH codes in $[(c_{m_i}^{(k)})_j - (c_n^{(1)})_j]$ are independent and uniformly distributed for $\forall k$, which is the necessary condition to find the average MUI. Accordingly, the SER considered here will be the average SER.

The SER is evaluated based on the assumption $\mathbf{T}^{(1)} = \{d_1^{(1)}, \ldots, d_{(N_p/N_s)}^{(1)}\}$ is transmitted using the TH code $\mathbf{c}_0^{(1)}$ determined by $\mathbf{C}^{(1)}$, where a symbol error will occur if

$$\max\left\{L^{(1)}(n,\mathbf{v})\right\} \Rightarrow [\hat{\mathbf{T}}^{(1)}|\hat{\mathbf{C}}^{(1)}] \neq [\mathbf{T}^{(1)}|\mathbf{C}^{(1)}]. \tag{4.16}$$

To find the SER, denoted by $P(\epsilon)$, we derive the probability of correct decision $P_c$ defined by

$$\begin{aligned} P_c &= 1 - P(\epsilon) \\ &\triangleq \Pr\left[\max\left\{L^{(1)}(n,\mathbf{v})\right\} = L^{(1)}(0,\mathbf{T}^{(1)})\right]. \end{aligned} \tag{4.17}$$

Deriving $P_c$ requires the comparison of $L^{(1)}(0,\mathbf{T}^{(1)})$ to $\{L^{(1)}(n,\mathbf{v})\}$ for $(2^{(N_p/N_s)}M - 1)$ values, hence $P_c$ can be expressed as

$$P_c = \Pr\left[\bigcap_{\mathbf{v}\neq\mathbf{T}^{(1)}}\left\{L^{(1)}(0,\mathbf{T}^{(1)}) > L^{(1)}(0,\mathbf{v})\right\}\bigcap_{n=1}^{M-1}\bigcap_{\mathbf{v}}\left\{L^{(1)}(0,\mathbf{T}^{(1)}) > L^{(1)}(n,\mathbf{v})\right\}\right] \tag{4.18}$$

where $\bigcap_{\mathbf{v}}\left\{L^{(1)}(0,\mathbf{T}^{(1)}) > L^{(1)}(n,\mathbf{v})\right\}$ represents the event when $L^{(1)}(0,\mathbf{T}^{(1)})$ is greater than all the symbol decision statistics formed by the $n$th TH code for all the combinations of the BPPM-transmitted sequence. Due to the independence of the TH codes,

$$P_c = \prod_{n=0}^{M-1} P_{c_n} \tag{4.19}$$

where $P_{c_n} \triangleq \Pr\left[\bigcap_{\mathbf{v}}\left\{L^{(1)}(0,\mathbf{T}^{(1)}) > L^{(1)}(n,\mathbf{v})\right\}\right]$ ($\mathbf{v} \neq \mathbf{T}^{(1)}$ for $n = 0$) and $P_{c_1} = \cdots = P_{c_{(M-1)}}$ because the TH codes $\{c_n^{(1)}\}$ for $\{n = 1, \ldots, M-1\}$ are statistically identical.

Comparison of $L^{(1)}(0,\mathbf{T}^{(1)})$ to $\{L^{(1)}(0,\mathbf{v})\}$ requires that $\{\hat{d}_i \,|\, i = 1, \ldots, N_p/N_s\}$ should be correct such that

$$\begin{aligned} P_{c_0} &= \Pr\left[\bigcap_{\mathbf{v}\neq\mathbf{T}^{(1)}}\left\{L^{(1)}(0,\mathbf{T}^{(1)}) > L^{(1)}(0,\mathbf{v})\right\}\right] \\ &= \prod_{i=1}^{N_p/N_s}\Pr\left[D_{i,0,d_i}^{(1)} - D_{i,0,d_i'}^{(1)} > 0\right]. \end{aligned} \tag{4.20}$$

Since the correlator outputs are statistically independent and identical for each bit transmitted using BPPM, using (4.12) we rewrite (4.20) as

$$P_{c_0} = \left\{ \Pr\left[ S_0 + I_0 + \eta_0 > 0 \right] \right\}^{N_p/N_s} \tag{4.21}$$

where $S_0 = A_1 N_s[R(0) - R(\delta_d)]$, $I_0 = I_{i,0,d_i} - I_{i,0,d_i'}$, and $\eta_0 = \eta_{i,0,d_i} - \eta_{i,0,d_i'}$.

To derive $P_{c_n}$ for $\{n = 1, \ldots, M-1\}$, we evaluate $P_{e_n}$, the probability of the event when $L^{(1)}(0, \mathbf{T}^{(1)})$ is not greater than all the symbol decision statistics formed by the $n$th TH code, such that

$$\begin{aligned} P_{e_n} &= 1 - P_{c_n} \\ &\triangleq \Pr\left[ \bigcup_{\mathbf{v}} \left\{ L^{(1)}(0, \mathbf{T}^{(1)}) < L^{(1)}(n, \mathbf{v}) \right\} \right]. \end{aligned} \tag{4.22}$$

Since each comparison of $L^{(1)}(0, \mathbf{T}^{(1)})$ to $L^{(1)}(n, \mathbf{v})$ is not independent of each other, an exact evaluation of $P_{e_n}$ is not allowed, and hence we derive the lower and upper bounds on (4.22) as

$$\begin{aligned} P_{e_n}^{(L)} &= \max_{\mathbf{v}} \left\{ \Pr\left[ L^{(1)}(0, \mathbf{T}^{(1)}) < L^{(1)}(n, \mathbf{v}) \right] \right\} \leq P_{e_n} \\ P_{e_n}^{(U)} &= \sum_{\mathbf{v}} \Pr\left[ L^{(1)}(0, \mathbf{T}^{(1)}) < L^{(1)}(n, \mathbf{v}) \right] \geq P_{e_n}. \end{aligned} \tag{4.23}$$

Here, the lower bound $P_{e_n}^{(L)}$ can be derived from the fact that the union of all comparisons includes the comparison yielding the highest probability, as a subset, and the upper bound $P_{e_n}^{(U)}$ is obtained by observing the fact that the total sum of individual probabilities (associated with each comparison) is greater than or equal to the probability of the union of all comparisons, because such comparisons are not mutually exclusive [75]. Using (4.10) and (4.12), $\Pr\left[ L^{(1)}(0, \mathbf{T}^{(1)}) < L^{(1)}(n, \mathbf{v}) \right]$ can be written as

$$\Pr\left[ L^{(1)}(0, \mathbf{T}^{(1)}) < L^{(1)}(n, \mathbf{v}) \right] = \Pr\left[ S_n + I_n + \eta_n < 0 \right] \tag{4.24}$$

where $S_n = A_1 N_p R(0)$, $I_n = \sum_{i=1}^{N_p/N_s} I_{i,0,d_i} - I_{i,n,v_i}$, and $\eta_n = \sum_{i=1}^{N_p/N_s} \eta_{i,0,d_i} - \eta_{i,n,v_i}$.

To find the SER $P(\epsilon)$, (4.21) and (4.24) should be evaluated by appropriately modelling the MUI. While Gaussian approximation is mostly used to model the MUI, it does not provide accurate performance results in the medium and high SNR regions [15]. For this

reason we resort to the characteristic function (CF) method [15] to accurately evaluate the SER performance. The CF's of $I_0$ and $I_n$ given in (4.21) and (4.24), denoted by $\Phi_{I_0}(\omega)$ and $\Phi_{I_n}(\omega)$, are derived in Appendix B. Once the CF's of $I_0$ and $I_n$ are obtained, we define $\Lambda_0 = I_0 + \eta_0$ and $\Lambda_n = I_n + \eta_n$. Due to the independence of the MUI and noise terms, the CF of $\Lambda$ can be expressed as

$$\Phi_{\Lambda_0}(\omega) = \Phi_{I_0}(\omega)\Phi_{\eta_0}(\omega), \quad \Phi_{\Lambda_n}(\omega) = \Phi_{I_n}(\omega)\Phi_{\eta_n}(\omega) \tag{4.25}$$

where the CF's of the noise terms are $\Phi_{\eta_n}(\omega) = e^{-\sigma_{\eta_n}^2\omega^2/2}$ with $\sigma_{\eta_0}^2 = \frac{N_0}{E_b}N_s^2[R(0) - R(\delta_d)]$ $(n = 0)$ and $\sigma_{\eta_n}^2 = \frac{N_0}{E_b}N_sN_pR(0)$ $(n \neq 0)$, and $\Phi_{\Lambda_0}$ and $\Phi_{\Lambda_n}$ are the CF's of the total interference. Taking the inverse transform of (4.25) as in [15], the cumulative distribution function of $\Lambda$ can be expressed as

$$F_\Lambda(x) = \frac{1}{2} + \frac{1}{\pi}\int_0^\infty \frac{\sin(x\omega)}{\omega}\Phi_\Lambda(\omega)\,d\omega. \tag{4.26}$$

Then $P_{c_0}$ in (4.21) can be evaluated as

$$P_{c_0} = \Big\{ \Pr[\,S_0 + \Lambda_0 > 0\,] \Big\}^{N_p/N_s} = \Big[ F_{\Lambda_0}(S_0) \Big]^{N_p/N_s}. \tag{4.27}$$

The bounds $P_{e_n}^{(L)}$ and $P_{e_n}^{(U)}$ depending on the transmitted sequence $\mathbf{T}^{(1)}$ are calculated as

$$\begin{aligned} P_{e_n}^{(L)} &= \max_{\mathbf{v}} \left\{ \sum_{\mathbf{T}^{(1)}} \Pr\Big[\mathbf{T}^{(1)}\Big] \Pr[\,S_n + \Lambda_n < 0\,] \right\} \\ &= \max_{\mathbf{v}} \left\{ \sum_{\mathbf{T}^{(1)}} \Pr\Big[\mathbf{T}^{(1)}\Big] \Big[1 - F_{\Lambda_n}(S_n)\Big] \right\} \qquad (4.28) \\ P_{e_n}^{(U)} &= \sum_{\mathbf{v}} \sum_{\mathbf{T}^{(1)}} \Pr\Big[\mathbf{T}^{(1)}\Big] \Pr[\,S_n + \Lambda_n < 0\,] \\ &= \sum_{\mathbf{v}} \sum_{\mathbf{T}^{(1)}} \Pr\Big[\mathbf{T}^{(1)}\Big] \Big[1 - F_{\Lambda_n}(S_n)\Big] \qquad (4.29) \end{aligned}$$

where $\Pr\Big[\mathbf{T}^{(1)}\Big]$ is the probability of each equally likely transmitted $(N_p/N_s)$-length sequence. Finally, the lower and upper bounds on the SER, denoted by $P_L(\epsilon)$ and $P_U(\epsilon)$, are evaluated as

$$\begin{aligned} P_L(\epsilon) &= 1 - P_{c_0} \prod_{n=1}^{M-1} \Big[1 - P_{e_n}^{(L)}\Big], \\ P_U(\epsilon) &= 1 - P_{c_0} \prod_{n=1}^{M-1} \Big[1 - P_{e_n}^{(U)}\Big]. \end{aligned} \tag{4.30}$$

## 4.4 Results

In this section, we present the numerical and simulation results, where MCSK/BPPM and TH-BPPM are compared under different conditions. Initially, the theoretical upper and lower bounds on the SER for MCSK/BPPM are evaluated at various information rates using (4.30). The SER obtained from simulations is compared to the upper and lower bounds for verification. For performance comparison of MCSK/BPPM and TH-BPPM systems, (4.12) is simulated to calculate the symbol decision statistics given in (4.10) for various information rates determined by $M$ and $N_p/N_s$ in both an AWGN channel and the IEEE 802.15.3a channel model [54]. For simplicity in the IEEE channel model, the $T_c$-spaced channel model is used, where channel delays are quantized to nearest chip time, and the associated multipath coefficients are summed up linearly before the channel coefficients are normalized. Then, the BER is found by evaluating (4.11) and compared to the BER of the TH-BPPM under the same power constraint. The SNR defined for the "same power constraint" is the one subject to the same average transmit power per frame time, i.e., SNR is defined as $E_b/N_0$. At the end of the section, the receiver complexities of MCSK/BPPM and TH-BPPM are discussed.

### 4.4.1 MCSK/BPPM vs. TH-BPPM

The system parameters $T_f = 50\,ns$, $T_c = 0.9\,ns$, $\delta_d = 0.15\,ns$, $N_h = 8$, $N_u = 8$ and $N_s = 2$ are commonly used for both MCSK/BPPM and TH-BPPM systems with perfect power control, unless otherwise stated. Accordingly, the information rate of TH-BPPM is $R_b = 10$ Mbits/s. For MCSK/BPPM, the number of TH codes per user $M$, and the TH code period $N_p$ are varied to control the information rate given in (4.2), which is greater than $R_b$. The TH codes of MCSK/BPPM are generated based on the TH code design criteria explained in Section 4.2. The TH code elements of TH-BPPM are assumed to be uniformly distributed random variables in $[0, N_h - 1]$.

In Figs. 4.3 and 4.4, the theoretical upper and lower bounds on SER in an AWGN channel are plotted for $\{N_p/N_s = 1, M = 2, 4\}$ and $\{N_p/N_s = 2, M = 2, 4\}$, respectively. The theoretical bounds are calculated based on randomly changing the TH code sets, hence resulting in the average system performance. For comparison, the simulation SER is obtained by using the corresponding parameter sets above when non-overlapping TH codes are used, randomly changing every $100N_pT_f$ (i.e., 100 symbols). Changing the TH code set helps

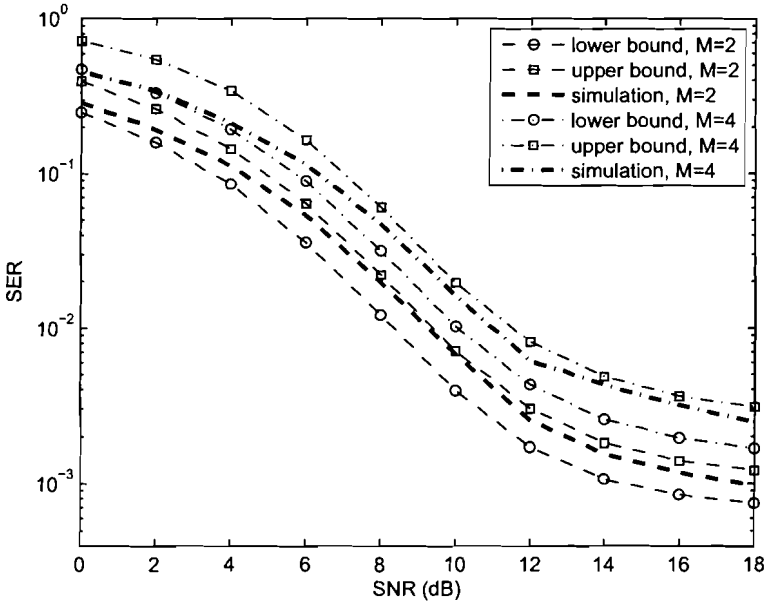


Figure 4.3: Lower and upper bounds on SER for $N_p/N_s = 1$.

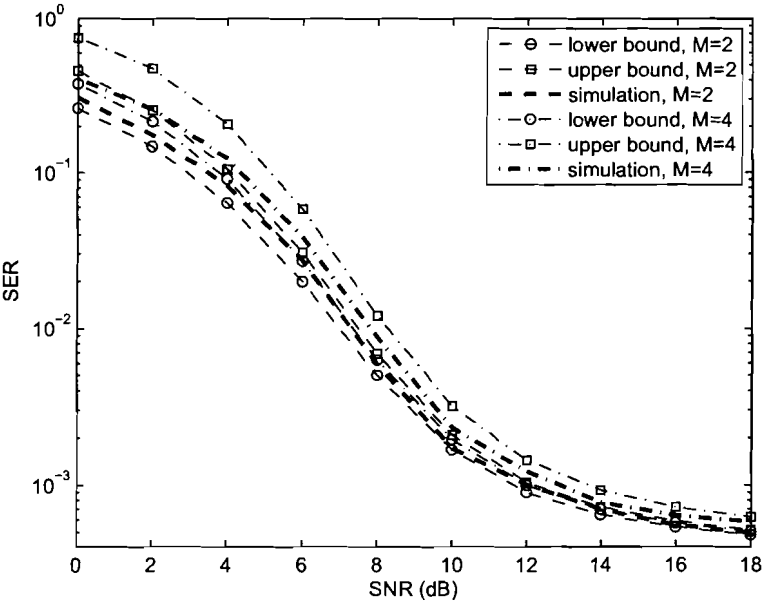


Figure 4.4: Lower and upper bounds on SER for $N_p/N_s = 2$.

finding the average system performance, whereas using a single TH code set repeatedly may have better or worse performance than the average. In (4.30), upper and lower bounds depend on $P_{e_0}$ and $P_{e_n}$ $(n \neq 0)$, where $\{P_{e_n}, (n \neq 0)\}$ are identical. When $N_p/N_s = 1$, the observation space used for symbol detection is limited, therefore the symbol errors are similarly contributed by $P_{e_0}$ (detecting the same TH code but different BPPM-bit) and $P_{e_n}$ $(n \neq 0)$ (detecting different TH codes). When the observation space is enlarged with $N_p/N_s = 2$, where 2 BPPM-bits are transmitted with the same TH code, most symbol errors occur due to detecting the wrong BPPM-bit or -bits but the correct TH code. Hence, $P_{e_0} >> P_{e_n}$ $(n \neq 0)$ as a result of the MLSE detector. According to the explained conditions on $P_{e_0}$ and $P_{e_n}$ $(n \neq 0)$ for two cases $(\{N_p/N_s = 1, 2\})$ being evaluated in (4.30), the bounds of $N_p/N_s = 2$ case should be tighter than that of $N_p/N_s = 1$ case. This is observed in Figs. 4.3 and 4.4. It can also be observed that the simulation results are within the upper and lower bounds, confirming the validity of the analysis.

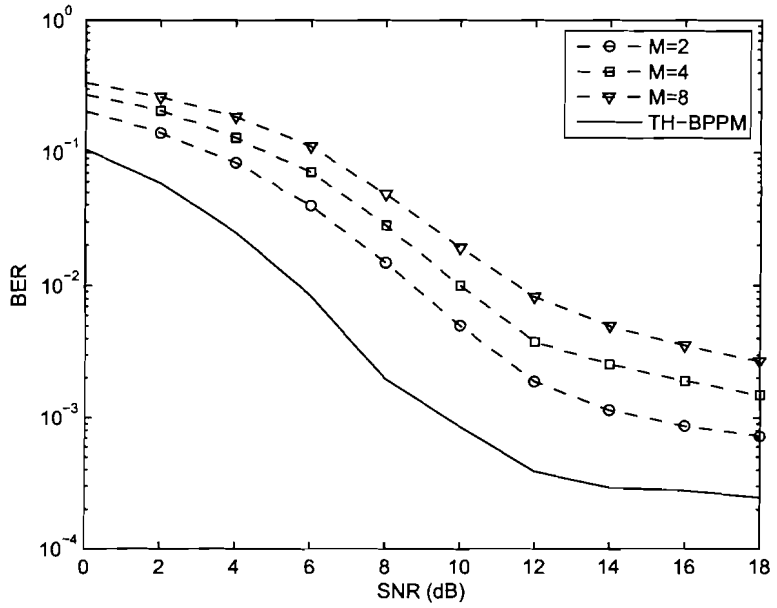


Figure 4.5: BER curves for the same power constraint when $N_p/N_s = 1$.

Figs. 4.5, 4.6 and 4.7 show the BER curves of MCSK/BPPM and TH-BPPM systems in an AWGN channel when their transmit powers are the same for $\{N_p/N_s = 1; M = 2, 4, 8\}$, $\{N_p/N_s = 2; M = 2, 4, 8\}$ and $\{N_p/N_s = 4; M = 2, 4, 8\}$, respectively. In Fig. 4.5, when $N_p/N_s = 1$, the MCSK/BPPM shows the worst performance for every value of SNR at different information rates. The MCSK/BPPM with $\{N_p/N_s = 1; M > 1\}$ resembles the TH-BPPM as it transmits one bit with one of the $M$ TH codes fixed. Because of fixed transmit power per frame time, the high-order modulation of MCSK/BPPM effectively reduces the SNR per bit as $M$ increases. Furthermore, the observation time (i.e., $N_pT_f = N_sT_f$) for the MCSK/BPPM remains the same as the TH-BPPM, so that there is no additional detection gain even with the MLSE receiver structure. Therefore, there is no performance gain when $N_p/N_s = 1$, and while the information rate is increased with the increase of $M$, the performance degrades further.

As $N_p/N_s$ increases, resulting in enlarged observation space and slight increase in the SNR per bit, the MLSE receiver structure increases the system performance significantly with respect to the same $M$ values, and with respect to the $\{N_p/N_s = 1\}$ case as shown in

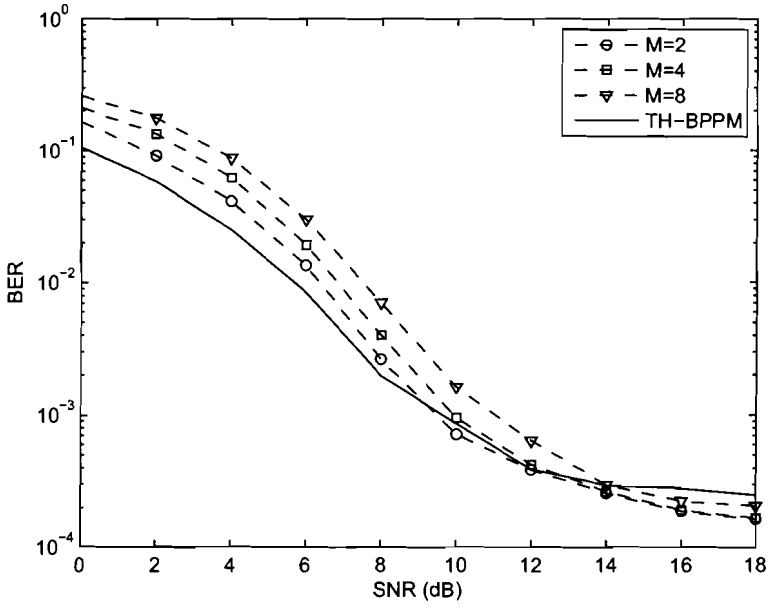


Figure 4.6: BER curves for the same power constraint when $N_p/N_s = 2$.

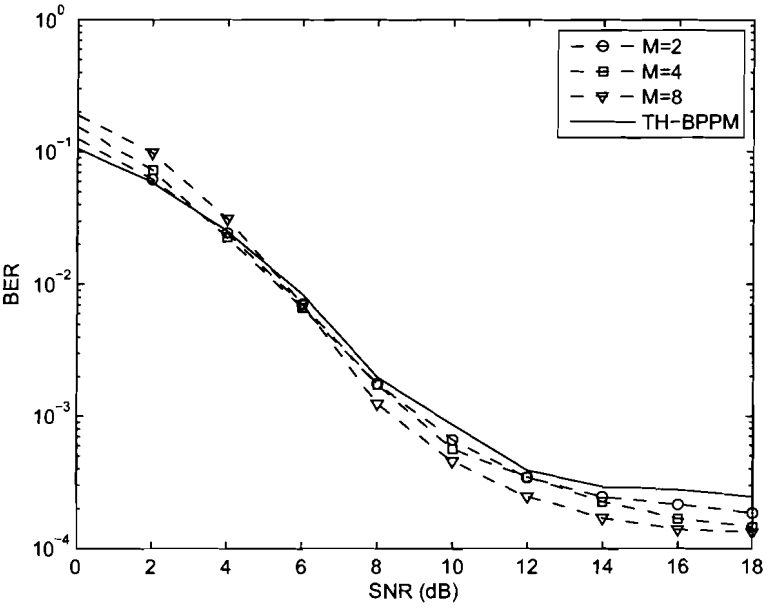


Figure 4.7: BER curves for the same power constraint when $N_p/N_s = 4$.

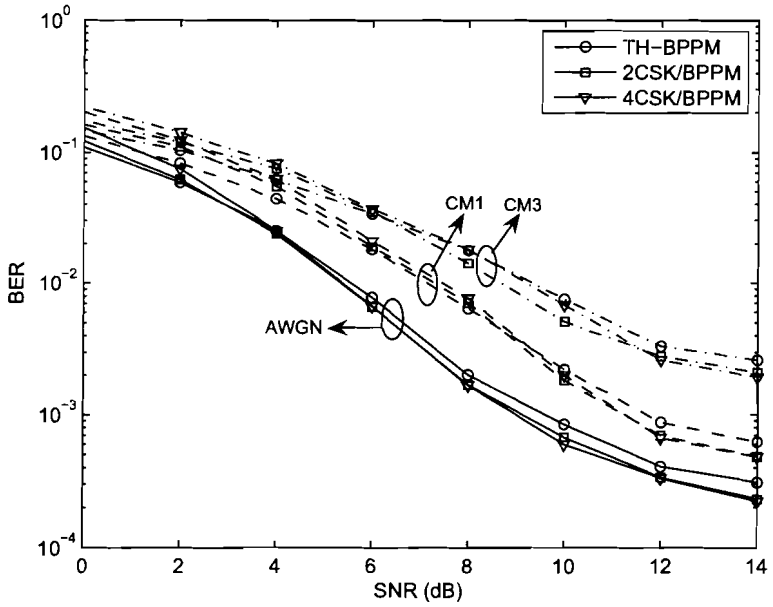


Figure 4.8: BER curves in AWGN, LOS (CM1) and NLOS (CM3) channel types when $N_p/N_s = 4$.

Figs. 4.6 and 4.7. For a fixed $N_p/N_s$ value $\geq 2$, increasing $M$ degrades the performance in low (SNR $<$ 5dB) and medium (5dB $<$ SNR $<$ 12dB) SNR regions, however the performances are similar in high SNR region (SNR $>$ 12dB). While $\{N_p/N_s = 2, \forall M\}$ shows better performance than the TH-BPPM only for the high SNR region, $\{N_p/N_s = 4, \forall M\}$ shows better performance for both medium and high SNR regions. Also, the performance of MCSK/BPPM does not improve much in the high SNR region with further increasing $N_p/N_s$.

After studying the effects of $N_p/N_s$ and $M$ on MCSK/BPPM in an AWGN channel, the effect of multipath fading on the system performance is considered. For the performance comparison of MCSK/BPPM and TH-BPPM, IEEE 802.15.3a line-of-sight (LOS) and non-LOS (NLOS) channel types CM1 and CM3 [54] are considered, respectively. For both channel types, a partial-Rake receiver ($L_p = 10$) is used. Since MCSK/BPPM $\{N_p/N_s = 4;\ M = 2, 4\}$ performs similar (i.e., slightly better or worse depending on the SNR value) to TH-BPPM in an AWGN channel as shown in Fig. 4.7, the same cases $\{N_p/N_s = 4;\ M = 2, 4\}$ are considered for the multipath fading channels as plotted in Fig. 4.8. It can be

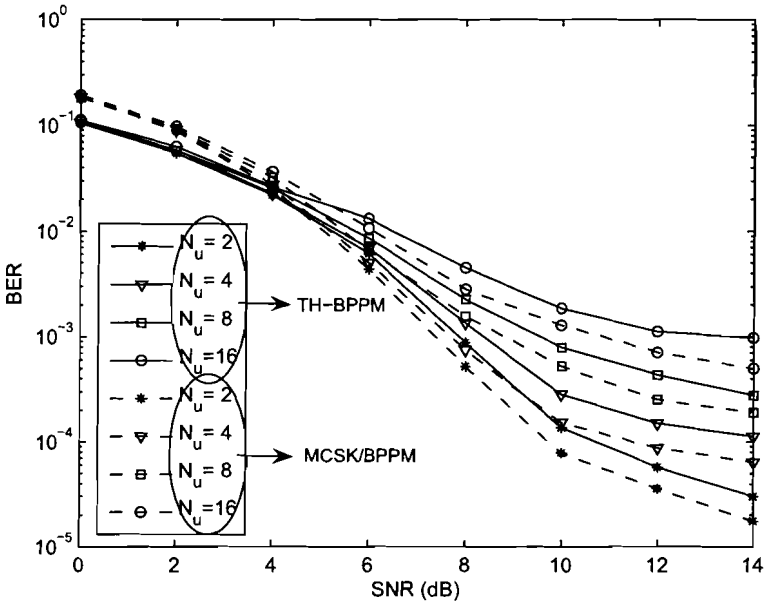


Figure 4.9: BER curves in the presence of $(N_u - 1)$ interfering users when $N_p/N_s = 4$ and $M = 8$.

observed that the MCSK/BPPM and TH-BPPM performances in CM1 and CM3 degrade about 2dB and 4dB with respect to their performances in the AWGN channel, respectively. On the other hand, MCSK/BPPM and TH-BPPM perform similar in CM1 and CM3 channel types, where their performances are slightly different depending on the SNR.

In Fig. 4.9, the effect of $(N_u - 1)$ interfering users on the performance of a single user is studied. For different number of active users $\{N_u = 2, 4, 8, 16\}$ considered in the system, MCSK/BPPM $\{N_p/N_s = 4;\ M = 8\}$ outperforms TH-BPPM for all cases in the medium and high SNR regions. This means that when the same number of users are active in both systems, each user of MCSK/BPPM shows improved performance at increased data rate.

The performance improvement of MCSK/BPPM over TH-BPPM for different cases presented is mainly due to the MLSE receiver structure used. For that reason, the receiver complexities are compared in the next subsection.

### 4.4.2 Receiver complexity

The receiver complexities of MCSK/BPPM and TH-BPPM are compared in this subsection in terms of the number of correlations and decision statistics, and the data rate increase.

MCSK/BPPM transmits and detects a $(N_p/N_s + \log_2 M)$-bit symbol using an MLSE structure for the duration of $(N_p/N_s)$ bits that are transmitted and detected individually by TH-BPPM. For the same transmit time, both modulations are compared in Table 4.1. When MCSK/BPPM is used, while the number of decision statistics grow exponentially

Table 4.1: Complexity comparison of MCSK/BPPM and TH-BPPM.

| | data rate | no. of correlations | no. of decision statistics |
|---|---|---|---|
| MCSK/BPPM | $\left(1+\frac{\log_2 M}{(N_p/N_s)}\right)\cdot R_b$ | $2M\cdot\left(\frac{N_p}{N_s}\right)$ | $2^{\left(\frac{N_p}{N_s}\right)}\cdot M$ |
| TH-BPPM | $R_b$ | $\frac{N_p}{N_s}$ | $\frac{N_p}{N_s}$ |

with $(N_p/N_s)$, the data rate is reduced, however the BER performance is improved. On the other hand, $M$ increases the number of decision statistics linearly, the data rate by $\log_2 M$, and improves the BER for a properly selected $N_p/N_s$ (e.g., improved MCSK/BPPM performances in Fig. 4.7). Considering Table 4.1 and the BER performance results presented in this section, a desired implementation for MCSK/BPPM can be made by appropriately selecting the system design parameters.

## 4.5 Conclusion

MCSK/BPPM, a new modulation format for UWB-IR communications, was proposed and analyzed. An orthogonal set of user-specific TH codes was employed for the MCSK to increase the information rate, while the system performance was controlled by a proper selection of TH codes and their periods. The proposed modulation format was studied from both the performance and implementation viewpoint, and compared to the conventional TH-BPPM under the same transmit power constraint. It was shown that the proposed modulation format can achieve better BER performance at increased information rate with a modest increase in the receiver structure. Considering these advantages, MCSK/BPPM can be implemented for both high-rate applications of IEEE 802.15.3a and low-rate applications of IEEE 802.15.4a.

# Chapter 5

# PSD Characteristics of MCSK Based Impulse Radios

In the previous two chapters, $M$-ary code shift keying (MCSK) impulse modulation and the combined MCSK/binary pulse position modulation (BPPM) were presented. It was shown that both modulations provided system performance improvements over the conventional time-hopping $M$-ary PPM (TH-MPPM) and TH-BPPM, respectively. In this chapter, power spectral density (PSD) characteristics of MCSK based impulse radios are given as the third main contribution of this dissertation.[1] The main motivation of the PSD study and the TH code set design of MCSK based impulse radios presented here is to increase the effective TH code period of conventional TH ultra wideband impulse radios (UWB-IRs) in order to suppress undesired peaks in the PSD resulting from finite-length TH codes.

## 5.1 Introduction

One of the main features of UWB communications is its overlaying structure with the existing systems due to its low power emission per unit bandwidth [77]. This feature, however, has raised a concern for UWB systems creating interference to co-existing systems. In Section 2.2, the PSD that depends on the spectrum of the unmodulated pulse [17], [20] and the modulation effects due to data transmission and TH codes [11], [39] was presented. When the effects of modulation on the PSD are considered, it is shown that due to the *periodicity* of

[1]The material presented here is a combination of the works published in [67] and [76].

the finite-length TH codes used in conventional UWB-IRs, the spectrum exhibits undesired peaks for both continuous and discrete spectrum that may create significant interference to co-existing systems [11]. These peaks can be smoothed and suppressed if the TH code length can be made *infinite*, however, this approach is infeasible considering the TH code design issues and the realization of TH codes at the receiver.

$M$-ary code shift keying (MCSK) was introduced to BPPM modulated UWB-IRs (i.e., MCSK/BPPM) in [70] to increase the data rate of conventional BPPM IRs as also presented in Chapter 4. MCSK can also be applied to BPAM (i.e., MCSK/BPAM) to include all the IRs (i.e., MCSK-IR). MCSK-IRs randomly select a code from a set of $M$ distinct TH codes per user every TH code period. This selection results in increased *effective* TH code period, which helps smoothing the continuous spectrum and suppressing the discrete spectral components as presented in [40]. Although the general PSD of MCSK-IRs was presented in that paper, the PSD was derived based on [39], where the change of TH codes within a code period was neglected, resulting in the TH code *edge effect*. In this chapter, in order to evaluate accurately the effects of TH code design on the spectrum, the exact PSD of MCSK-IRs is derived by considering the changes in the TH code within each frame time. In addition to exact PSD analysis, the code design issues of MCSK based IRs are addressed, which are important for real system implementation. Accordingly, the trade-off between multiple-access (MA) capability and efficient spectrum shaping is discussed for different code design criteria. It is shown that either random TH code effect or improved spectrum with relatively high MA capability can be achieved using appropriate code design techniques. The results of the code design techniques used for MCSK-IRs are then extended to *conventional* IRs in order to improve their PSD.

The rest of the chapter is organized as follows. A general signalling structure for MCSK-IRs is given in Section 5.2. The exact PSD of MCSK based IRs is derived and compared to the PSD of conventional IRs in Section 5.3. Two main code design techniques are introduced and their effects on spectrum shaping and MA capability are discussed in Section 5.4. Concluding remarks are given in Section 5.5.

## 5.2 Signal Model

MCSK-IRs are designed based on TH-IR systems (TH-BPPM and TH-BPAM), hence initially the signalling structure of conventional TH-IR systems will be given.[2] A TH-IR is designed to transmit a single pulse per user within a frame time $T_f$. The location of the pulse is determined by data modulation (for only PPM) and TH codes (for PPM and PAM) with period $N_pT_f$. For reliable communications, each pulse is repeated $N_s$ times for each data bit, where $N_s < N_p$. That means a TH code transmits $N_p/N_s$ data bits for its period and repeats itself every $N_pT_f$ for each new data set. For $N_p/N_s = L$ being an integer, the TH-IR signal that transmits $N_p/N_s$ bits during one period of the TH code can be modeled as

$$s_p(t) = \sum_{l=0}^{L-1} \sum_{h=0}^{N_s-1} a_l \cdot w_{tr}\Big(t - lT_b - hT_f - (c_0)_{(lN_s+h)}T_c - d_l\delta_d\Big) \tag{5.1}$$

where $s_p(t)$ is the transmitted signal for the duration of the TH code, $w_{tr}(t)$ is the transmitted pulse, $T_b = N_sT_f$ is the one-bit transmit time, and $T_c$ is the chip time. $N_p/N_s$ bits are transmitted for the duration of the deterministic TH code $\mathbf{c}_0$, where $(c_0)_{(lN_s+h)}$ determines the location of the pulse transmitted for the $l$th bit's $h$th frame time. $\mathbf{c}_0$ is a deterministic TH code consisting of $N_p$ integers whose element satisfies $0 \leq (c_0)_j < N_h$, $\forall j$ and $N_hT_c \leq T_f$. For the data transmission of a TH-BPPM system, $d_l \in \{0, 1\}$ is the $l$th transmitted bit and $\delta_d$ is the PPM shift parameter, where $a_l = 1$ throughout the transmission; while for a TH-BPAM system, $a_l \in \{-1, 1\}$ is the $l$th transmitted bit, where $d_l = 0$.

In the MCSK/BPPM scheme introduced in [70], each user is assigned $M$ user-specific TH codes, as opposed to one TH code assignment per user as in TH-IR. While one-bit data is being transmitted using BPPM, additional $\log_2 M$-bit data selects a particular TH code from the set of $M$ user-specific TH codes, which is the $M$-ary CSK. For $N_p/N_s > 1$, the same TH code is used until $N_p$ pulses are transmitted. Accordingly, a new TH code will be selected randomly every $N_pT_f$ to transmit the new data sequence. A general MCSK signalling for MCSK/BPPM and MCSK/BPAM can be modeled by replacing $(c_0)$ by $(c_m)$ in (5.1), $m \in \{0, ..., M-1\}$, which gives

$$s_{p,m}(t) = \sum_{l=0}^{L-1} \sum_{h=0}^{N_s-1} a_l \cdot w_{tr}\Big(t - lT_b - hT_f - (c_m)_{(lN_s+h)}T_c - d_l\delta_d\Big) \tag{5.2}$$

[2]For the PSD analysis, the combined signalling structure given in (5.1) is considered as it is more appropriate for spectrum analysis than the signalling structures given in (2.1) and (2.2).

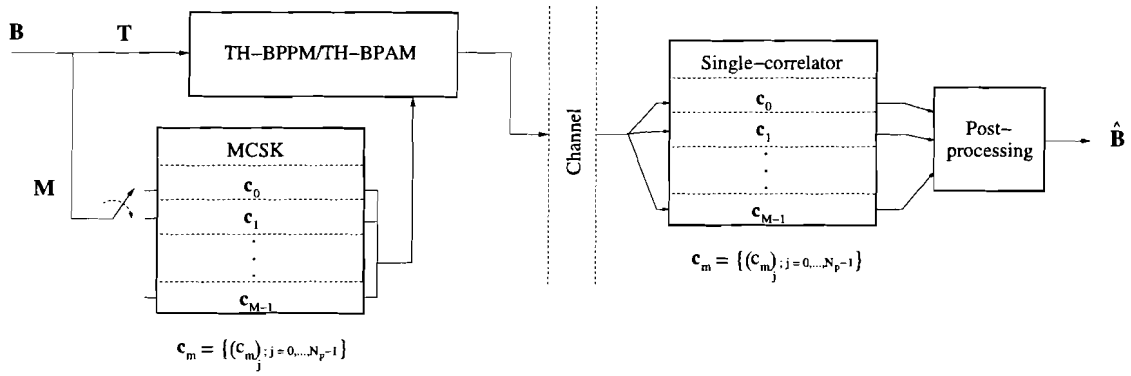


Figure 5.1: MCSK based transceiver.

where the index $m$ of $s_{p,m}(t)$ denotes the TH code information for every TH code period. The waveform in (5.2) transmits one set of bits (one symbol) $\{b_l\}$, $\mathbf{B} = \{b_l | l = 0, \ldots, (N_p/N_s) + \log_2 M - 1\}$, where $b_l = d_l$ and $b_l = a_l$, $0 \leq l < N_p/N_s$, for MCSK/BPPM and MCSK/BPAM, respectively. Let $\mathbf{T} \subset \mathbf{B}$ and $\mathbf{M} \subset \mathbf{B}$, where $\mathbf{T} = \{b_0, \ldots, b_{(N_p/N_s)-1}\}$ is the set of bits to be transmitted using BPPM or BPAM, and $\mathbf{M} = \{b_{(N_p/N_s)}, \ldots, b_{(N_p/N_s)+\log_2 M-1}\}$ is the input to MCSK to determine the index $m$ of the user-specific TH code $\mathbf{c}_m$. For independent identically distributed (i.i.d.) $b_l$, $\mathbf{M}$ will select one of the TH codes from the set $\mathbf{C} = \{\mathbf{c}_0, \mathbf{c}_1, \ldots, \mathbf{c}_{M-1}\}$ with equal probability of $\frac{1}{M}$. This procedure is repeated every $N_p T_f$, where the TH code and modulation data change accordingly. For illustration purposes, the transceiver structure of an MCSK based IR is depicted in Fig. 5.1 for the transmission of symbol $\mathbf{B}$. While $\mathbf{B}$ is transmitted with the procedure explained above, $M$ correlations performed by a single correlator followed by post-processing of the correlation outputs at the receiver detects the transmitted symbol. The receiver details can be found in [70], [71] and in Chapter 4 for system performance evaluation purposes.

With the above transmit structure and procedure, the continuously transmitted UWB signal $y(t)$ takes the form

$$y(t) = \sum_{k=-\infty}^{\infty} s_{p_k,m_k}\Big(t - k(N_p T_f)\Big) \tag{5.3}$$

where $p_k$ and $m_k$ represent the information transmitted for the $k$th information sets $\mathbf{T}_k$ and $\mathbf{M}_k$, respectively.

## 5.3 Spectrum Analysis

The signal $y(t)$ in (5.3) can be represented as $y(t) = w_{tr}(t) \otimes c(t)$, where

$$c(t) = \sum_{k=-\infty}^{\infty} \sum_{l=0}^{L-1} \sum_{h=0}^{N_s-1} a_l \, \delta\Big(t - k(N_p T_f) - lT_b - hT_f - (c_m)_{(lN_s+h)} T_c - d_l \delta_d\Big) \tag{5.4}$$

represents the overall modulation effects (both TH code and data) with $\delta(\cdot)$ being the Dirac delta function and $\otimes$ is the convolution operator. The PSD of $y(t)$ is $S_{yy}(f) = |W_{tr}(f)|^2 \cdot S_{cc}(f)$, where $|W_{tr}(f)|^2$ is the squared-magnitude spectrum of the unmodulated pulse and $S_{cc}(f)$ is the PSD of the modulation effects. To find $S_{cc}(f) = \mathcal{F}\{R_{cc}(\tau)\}$, where $\mathcal{F}\{\cdot\}$ denotes the Fourier transform and $R_{cc}(\tau)$ is the autocorrelation function (ACF) of $c(t)$, initially $R_{cc}(\tau)$ should be calculated. $R_{cc}(\tau)$ given in (5.5) is evaluated in Appendix C, and simplifies to (5.6) given below as

$$R_{cc}(\tau) = \frac{1}{N_p T_f} \int_0^{N_p T_f} \mathbf{E}\{c(t)c(t+\tau)\}dt \tag{5.5}$$

$$= \frac{1}{N_p T_f} \mathbf{E}\Bigg\{ \sum_{k'=-\infty}^{\infty} \sum_{l'=0}^{L-1} \sum_{l=0}^{L-1} \sum_{h'=0}^{N_s-1} \sum_{h=0}^{N_s-1} a_{l'} a_l \cdot \delta\Big(\tau - k'(N_p T_f) - (l'-l)T_b - (h'-h)T_f - [(c_{m_{k'}})_{(l'N_s+h')} - (c_{m_0})_{(lN_s+h)}]T_c - [d_{l'} - d_l]\delta_d\Big)\Bigg\} \tag{5.6}$$

where $\mathbf{E}\{\cdot\}$ is the expectation operator. A similar representation for $R_{cc}(\tau)$ was given in [11, eq. (13)] where $(c_{m_k})$ was assumed to be a single infinite-length TH code sequence. This allowed them to evaluate the PSD with a simple representation. The exact PSD for the signal in (5.3) is more complex due to accounting for TH code changes within each frame time $T_f$ when $M$-ary code shift keying is used. Accordingly, $R_{cc}(\tau)$ should be evaluated for every $T_f$-shift. In order to do so, let $k' = 0$, $l' = l$, $h' = h$ and let $z$ be the new variable to accommodate the changes in every code shift $zT_f$.

Then, $R_{cc}(\tau)$ becomes

$$R_{cc}(\tau) = \frac{1}{N_p T_f} \mathbf{E}\Bigg\{ \sum_{z=-\infty}^{\infty} \sum_{l=0}^{L-1} \sum_{h=0}^{N_s-1} a_{\lfloor (lN_s+h+z)/N_s \rfloor} a_l \cdot \delta\Big(\tau - zT_f - \big[d_{\lfloor (lN_s+h+z)/N_s \rfloor} - d_l\big]\delta_d - \Big[\big(c_{m_{(\lfloor (lN_s+h+z)/N_p \rfloor)}}\big)_{((lN_s+h+z) \bmod N_p)} - (c_{m_0})_{(lN_s+h)}\Big]T_c\Big)\Bigg\} \tag{5.7}$$

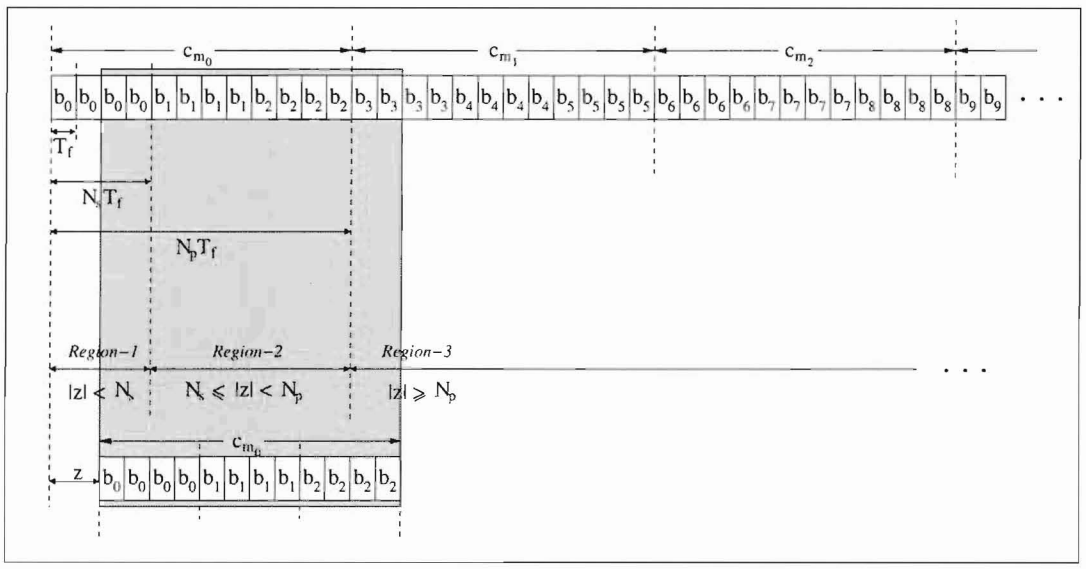


Figure 5.2: Illustration of ACF regions for $z \geq 0$.

where $\lfloor x \rfloor$ is the integer part of $x$. Calculation of $R_{cc}(\tau)$ can be illustrated as in Fig. 5.2. According to this illustration[3], each frame time $T_f$ in the signal carries the information bit $b_l$ for $N_s$ consecutive frames, where $L = N_p/N_s$ different bits are transmitted with the randomly selected code $c_{m_k}$ of length $N_p$. This structure repeats every $N_pT_f$ as seen in the first row. Since (5.7) equals the expectation value of the $N_p$-frame long summation of the data and code correlation of the signal for every integer shift value $z$ (here, the grey area represents the region of correlation and summation of the signal with its time shifted version), $N_p$-frame long signal in the second row is drawn to visualize the effect of $z$-shift on the data and code correlation values in order to define the regions, where the data and code correlation properties change. Based on the correlation properties of the signals in the first and the second row, three disjoint regions can be defined as $|z| < N_s$, $N_s \leq |z| < N_p$ and $|z| \geq N_p$, where they will be elaborated on more for the corresponding region conditions.

Accordingly, let us define $R_{cc}(\tau)$ as a summation of region-based ACFs

$$R_{cc}(\tau) = \frac{1}{N_pT_f} \sum_{i=1}^{3} \phi_i(\tau) \tag{5.8}$$

[3]Here, the data and code information is illustrated for 3 code periods $\{k = 0, 1, 2\}$, $N_s = 4$ and $L = N_p/N_s = 3$.

where $\phi_i(\tau)$ is the ACF in the corresponding region $i$. A general simplified representation for $\phi_i(\tau)$ associated with data and code changes can be written based on (5.7) as

$$\phi_i(\tau) \equiv \sum_{z} \sum_{(l,h)_{(i)}} \mathbf{E}\Big\{a_x a_y\Big\} \cdot \mathbf{E}\Big\{\delta\Big(\tau - zT_f - c_{m_k}(z)T_c - \big[d_x - d_y\big]\delta_d\Big)\Big\} \tag{5.9}$$

where $\sum_z$ represents the corresponding region with respect to $z$, $\sum_{(l,h)_{(i)}}$ represents the sub-regions where the data and code change, and indices $x$ and $y$ indicate different data for $x \neq y$. $c_{m_k}(z)$ represents the code term and is given as

$$c_{m_k}(z) = \Big[(c_{m_k})_{\left((lN_s+h+z\cdot[(sgn(z)+1)/2])\, mod\, N_p\right)} - (c_{m_0})_{\left((lN_s+h+z\cdot[(sgn(z)-1)/2])\, mod\, N_p\right)}\Big] \tag{5.10}$$

where $sgn(z)$ indicates the sign of $z$ and $c_{m_0}(z)$ refers to both codes being the same in the sub-region, whereas $c_{m_k}(z)$, $k \neq 0$ represents the presence of different codes in the given sub-region.

In *Region-1* ($|z| < N_s$), there are three sub-regions due to different data and code representations in the ACFs. Accordingly,

$$\phi_1(\tau) = \sum_{i=1}^{3} \phi_{1,i}(\tau) \tag{5.11}$$

where $\{\phi_{1,i}(\tau)\}$'s refer to ACFs in the sub-regions. These sub-regions can be best understood by studying *Region-1* depicted in Fig. 5.2. According to this figure, when $|z| < N_s$, the corresponding data bits of the correlation in the grey shaded area can either be

i) same for the same code (e.g., $b_0$ of the top signal and $b_0$ of the bottom signal are aligned for the same code $c_{m_0}$), *or*

ii) different for the same code (e.g., $b_1$ and $b_0$ are aligned for $c_{m_0}$), *or*

iii) different for the different code (e.g., $b_3$ and $b_2$ are aligned for codes $c_{m_1}$ and $c_{m_0}$, respectively).

For these sub-regions, the same correlation statistics that are aligned can be summed up by appropriately defining $\sum_{(l,h)_{(i)}}$. Mathematically, $\{\phi_{1,i}(\tau)\}$'s can be represented by evaluating (5.9) with the substitution of data, code and sub-region conditions, where $\Big(b_x = b_y$ (i.e., $a_x = a_y$, $d_x = d_y$), $c_{m_k}(z) = c_{m_0}(z)$ and $\sum_{(l,h)_{(1,1)}} \equiv \sum_{l=0}^{L-1} \sum_{h=0}^{N_s-1-|z|}\Big)$ for $\phi_{1,1}(\tau)$; $\Big(b_x \neq b_y$, $c_{m_k}(z) = c_{m_0}(z)$ and $\sum_{(l,h)_{(1,2)}} \equiv \sum_{l=0}^{L-2} \sum_{h=N_s-|z|}^{N_s-1}\Big)$ for $\phi_{1,2}(\tau)$; and $\Big(b_x \neq b_y$, $c_{m_k}(z) = c_{m_1}(z)$ and $\sum_{(l,h)_{(1,3)}} \equiv \sum_{l=L-1}^{L-1} \sum_{h=N_s-|z|}^{N_s-1}\Big)$ for $\phi_{1,3}(\tau)$.

Similarly, in *Region-2* ($N_s \leq |z| < N_p$),

$$\phi_2(\tau) = \sum_{i=1}^{2} \phi_{2,i}(\tau) \tag{5.12}$$

where this can be visualized by shifting the signal in the second row of Fig. 5.2 to *Region-2*. According to the correlation properties of the aligned signals after the $z$-shift, the sub-region conditions for each ACF can be represented as $\Big(b_x \neq b_y,\ c_{m_k}(z) = c_{m_0}(z)$ and $\sum_{(l,h)_{(2,1)}} \equiv \sum_{l=0}^{L-\lfloor \frac{|z|}{N_s} \rfloor - 2} \sum_{h=0}^{N_s-1} \bigcup \sum_{l=L-\lfloor \frac{|z|}{N_s} \rfloor - 1}^{L-\lfloor \frac{|z|}{N_s} \rfloor - 1} \sum_{h=0}^{N_s-(|z| \bmod N_s)-1} \Big)$ for $\phi_{2,1}(\tau)$; and $\Big(b_x \neq b_y,\ c_{m_k}(z) = c_{m_1}(z)$ and $\sum_{(l,h)_{(2,2)}} \equiv \sum_{l=L-\lfloor \frac{|z|}{N_s} \rfloor - 1}^{L-\lfloor \frac{|z|}{N_s} \rfloor - 1} \sum_{h=N_s-(|z| \bmod N_s)}^{N_s-1} \bigcup \sum_{l=L-\lfloor \frac{|z|}{N_s} \rfloor}^{L-1} \sum_{h=0}^{N_s-1} \Big)$ for $\phi_{2,2}(\tau)$.

*Region-3* can be redefined as $\Big\{(0 < |z| < \infty) - (|z| < N_p)\Big\}$, where

$$\phi_3(\tau) = \left(\frac{1}{2} \sum_{k=-\infty}^{\infty} \delta\Big(\tau - k(N_p T_f)\Big) - 1\right) \cdot \Big(\phi_{3+}(\tau) + \phi_{3-}(\tau)\Big) + \phi_{3(0)}(\tau) \tag{5.13}$$

represents the ACF due to periodically repeating sub-regions excluding the region ($|z| < N_p$). $\phi_{3+}(\tau)$ and $\phi_{3-}(\tau)$ are the repeating ACFs every $N_p T_f$, respectively, for $z \geq 0$ and $z \leq 0$. $\phi_{3(0)}(\tau)$ is the ACF when $z = 0$, and is included as the last term in (5.13) since it is subtracted *twice* for the region ($|z| < N_p$). $\phi_{3+}(\tau)$, $\phi_{3-}(\tau)$ and $\phi_{3(0)}(\tau)$ can be found with the substitutions $\Big\{\Big(\sum_z \equiv \sum_{z=0}^{N_p-1}\Big) \bigcap \mathcal{L}\Big\}$, $\Big\{\Big(\sum_z \equiv \sum_{z=-(N_p-1)}^{0}\Big) \bigcap \mathcal{L}\Big\}$ and $\Big\{\Big(\sum_z \equiv \sum_{z=0}^{0}\Big) \bigcap \mathcal{L}\Big\}$, respectively, where $\mathcal{L}$ is the set of conditions, that is, $\mathcal{L} \equiv \Big\{(b_x \neq b_y) \bigcap \Big(c_{m_k}(z) = c_{m_1}(z) \bigcap \sum_{(l,h)_{(3,1)}} \equiv \sum_{lh=0}^{N_p-|z|-1}\Big)\Big\} \bigcup \Big\{(b_x \neq b_y) \bigcap \Big(c_{m_k}(z) = c_{m_2}(z) \bigcap \sum_{(l,h)_{(3,2)}} \equiv \sum_{lh=N_p-|z|}^{N_p-1}\Big)\Big\}$.

Using (5.11) – (5.13), $S_{cc}(f)$ can be represented as

$$S_{cc}(f) = \frac{1}{N_p T_f} \sum_{i=1}^{3} \Phi_i(f) \tag{5.14}$$

where $\Phi_i(f) = \mathcal{F}\{\phi_i(\tau)\}$. The explicit form of (5.14) is not given in the text due to lengthy representation of multiple terms resulting from TH code changes represented by $m_0$, $m_1$, and $m_2$ in the index of $c_{m_k}(z)$. However, $\{\Phi_i(f)\}$ terms in (5.14) are presented in Appendix D for convenience.

For $M = 1$, (5.14) becomes the general PSD representation of a conventional IR with a single deterministic TH code, which can be obtained by substituting $M = 1$ into (D.4).

With this substitution, (5.14) reduces to a similar expression to those reported in [11, eq. (3)] and [39, eq. (13)]. For $M > 1$, the PSD in (5.14) is averaged over $M$ TH codes with the averaging effect of (D.4) on (D.5) – (D.7). This helps smoothing the continuous spectrum and suppressing the discrete spectrum, and will be further investigated in the next section.

For MCSK/BPAM, the expectation values given in (D.2) – (D.3) become

$$R_0^a = R_0^d(f) = R_1^d(f) = 1, \qquad R_1^a = 0, \tag{5.15}$$

therefore, the PSD of the modulation effects reduces to

$$S_{cc}^{PAM}(f) = \frac{1}{N_p T_f}\Phi_{1,1}(f) \tag{5.16}$$

where $\Phi_{1,1}(f)$ is the first term of (D.5). For MCSK/BPPM, the expectation values given in (D.2) – (D.3) become

$$R_0^a = R_1^a = R_0^d(f) = 1, \qquad R_1^d(f) = \frac{1+\cos(2\pi f \delta_d)}{2}. \tag{5.17}$$

Therefore, $S_{cc}^{PPM}(f) = S_{cc}(f)$ as given in (5.14) with the substitution of the corresponding expectation values in (5.17).

As reported in [78], most of the previous UWB PSD studies are based on either only analysis or simulation. In this work, derived PSDs are validated by simulations for different TH code sets using the periodogram-based simulation method, which is also considered in [78]. Accordingly, the PSD resulting from MCSK/BPAM and the continuous spectrum of MCSK/BPPM are *exactly* validated, whereas all the discrete spectral components of the simulated MCSK/BPPM are 40 dB less than the analysis results. This is an expected result as explained in [78], due to the product of the selected simulation parameters, $N \cdot T_s = 10^{-4}$ s, where $N$ is the number of samples in the signal and $T_s$ is the sampling time. Therefore, it can be claimed that the analysis is exact. In Fig. 5.3, a portion of the PSD of MCSK/BPPM is plotted to verify the analysis results. It can be seen that the continuous spectra are in perfect agreement and the discrete spectral components resulting from simulation are 40 dB less than the analysis results.

In the following sections, only analysis results will be plotted for convenience. The next section will continue with the code set design and the analysis of the resulting PSDs.

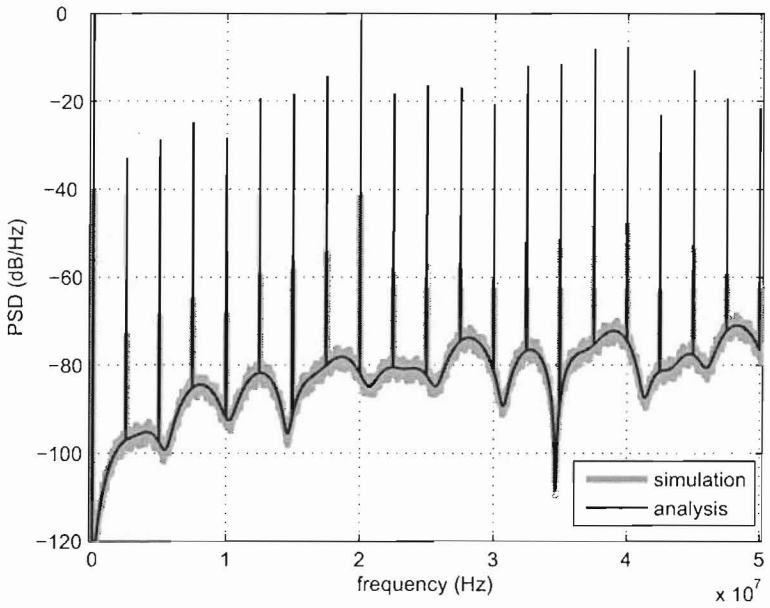


Figure 5.3: Comparison between analysis and simulation results.

## 5.4 TH Code Set Design

TH code set design affects the PSD as well as the MA capability. Considering these two criteria, two major code design techniques are studied. In these techniques, TH code sets are given in the form of a matrix, where

$$\mathbf{C} = \begin{bmatrix} (c_0)_0 & (c_0)_1 & \cdots & (c_0)_{N_p-1} \\ \vdots & \vdots & \cdots & \vdots \\ (c_{M-1})_0 & (c_{M-1})_1 & \cdots & (c_{M-1})_{N_p-1} \end{bmatrix} \tag{5.18}$$

is the designed TH code set with each row representing a TH code sequence $\mathbf{c}_m$, $m \in \{0, \ldots, M-1\}$ of length $N_p$, and each column representing the entries of $M$ distinct user-specific TH codes corresponding to the same frame time duration. Accordingly, the two code design techniques are as follows:

### 5.4.1 Code design technique-1

The first code set design technique is mainly considered for MCSK/BPPM, where the PSD suffers from multiple discrete spectral components. With this design, it is intended to eliminate most of the discrete spectral components (for PPM only), and to smooth the continuous spectrum (for PAM and PPM). This code design technique uses Corollary 1 given below to generate user-specific TH code sets.

*Corollary 1:* Given the set $\left\{0, \ldots, N_h - 1\right\}$ associated with possible time-hopping locations, determine an $M$ element subset $\mathbf{c}_{sub}$ from ${}_{N_h}C_M$ possible subsets, where ${}_nC_r = \frac{n!}{r!(n-r)!}$. Using the subset $\mathbf{c}_{sub}$, determine the vectors $\left[(c_0)_i \cdots (c_{M-1})_i\right]^T$ independently for $\forall i$ from ${}_MP_M$ possible arrangements, where ${}_nP_r = \frac{n!}{(n-r)!}$. The resulting code set $\mathbf{C}_1 = \left\{(c_j)_i \,|\, \forall j, \forall i\right\}$ used with MCSK-IRs generates discrete spectral components every $\frac{1}{T_f}$ instead of $\frac{1}{N_p T_f}$.

Let us evaluate the code design technique based on this corollary for MCSK/BPPM and MCSK/BPAM separately in order. The discrete spectral components of MCSK/BPPM result from (5.13), where they should occur at multiples of $\frac{1}{N_p T_f}$ due to the periodicity of TH codes for a given TH code set $\mathbf{C}$. However, the TH code set $\mathbf{C}_1$ designed according to the corollary above is similar to an infinite-length TH code used in a conventional TH-IR, where the discrete spectral components occur at multiples of $\frac{1}{T_f}$. Accordingly, in every column in $\mathbf{C}_1$, there exists the same set $\mathbf{c}_{sub}$ where each of the entries may be selected with equal probability every $T_f$. Therefore, the discrete spectral components occur every $\frac{1}{T_f}$, as same as a PSD resulting from a conventional TH-IR that uses an infinite-length TH code with equiprobable values for each frame time (also referred to as *random time hopping*). This phenomenon can be explained by the randomization of codes for every $T_f$, which yields the *effective* $N_p$ to be unity. With the substitution of effective $N_p$ into (D.7), it can be concluded that the number of discrete spectral components is reduced. In addition to reduced discrete PSD components, the averaging effect of $M$ TH codes suppresses the magnitude of the discrete spectral components which can be deduced from (D.4). The continuous spectrum of MCSK/BPPM, which results from (5.11) and (5.12), is also smoothed with the same averaging effect.

For $M = 8$, $N_h = 16$ and a randomly chosen subset $\mathbf{c}_{sub} = \left\{0, 2, 4, 6, 7, 8, 9, 12\right\}$, the

code set $\mathbf{C}_1$ is generated based on Corollary 1 for analysis and simulation.

$$\mathbf{C}_1 = \begin{bmatrix} 6 & 4 & 8 & 6 & 4 & 12 & 9 & 6 \\ 9 & 7 & 9 & 4 & 0 & 2 & 7 & 2 \\ 8 & 8 & 12 & 7 & 9 & 9 & 4 & 0 \\ 4 & 2 & 4 & 12 & 7 & 0 & 6 & 8 \\ 7 & 9 & 0 & 9 & 2 & 8 & 12 & 9 \\ 2 & 12 & 6 & 2 & 12 & 4 & 2 & 4 \\ 12 & 6 & 2 & 0 & 8 & 7 & 0 & 7 \\ 0 & 0 & 7 & 8 & 6 & 6 & 8 & 12 \end{bmatrix} \tag{5.19}$$

$\mathbf{C}_1$ is used with the system parameters $T_f = 50\,ns$, $T_c = 2\,ns$, $N_p = 8$, $N_s = 4$, $\delta_d = 0.15\,ns$ and $w_{tr}(t)$ with the frequency response $|W_{tr}(f)|^2 = 1$ (these parameters are used for the rest of the plots unless otherwise stated) to generate the PSD of MCSK/BPPM modulated signal. The assumption $|W_{tr}(f)|^2 = 1$ is made in order to evaluate explicitly the modulation effects on the PSD. Accordingly, Figs. 5.4 and 5.5 show the PSDs of the conventional TH-BPPM with the TH code $\mathbf{c}_0$ (the first row of $\mathbf{C}_1$) and of 8-CSK/BPPM with the TH code set $\mathbf{C}_1$ over the $[0, \frac{1}{T_c}]$ frequency range for dB/Hz and dB/MHz resolutions[4], respectively. Figures with different PSD resolutions are generated in order to better understand the effects of code design with the ongoing UWB spectral mask definition discussions (especially for magnitude and resolution) within Europe and Asia. It can be seen from Fig. 5.4 that 8-CSK/BPPM (lower plot) exhibits discrete PSD components at multiples of $\frac{1}{T_f}$ with smoothed continuous spectrum and suppressed discrete magnitudes compared to the conventional TH-BPPM (upper plot) exhibiting discrete components at the multiples of $\frac{1}{N_p T_f}$. Fig. 5.5 serves as a reference to FCC UWB spectral mask with its dB/MHz resolution. For this resolution, while the 8-CSK/BPPM ($M = 8$) resolves most of the discrete components, resulting in a large bandwidth of smooth spectrum, TH-BPPM ($M = 1$) exhibits peaky high magnitude power components due to the discrete PSD components. An observation similar to the PSD of 8-CSK/BPPM was made for TH-BPPM with random TH in [11], where 8-CSK/BPPM with code design technique-1 exhibits the similar *infinite* length TH code effect.

At this point, some notes should be made with regard to the compliance of three

[4]For the dB/MHz resolution, the total transmission power is calculated for each non-overlapping bandwidth of 1 MHz and averaged over the whole bandwidth.

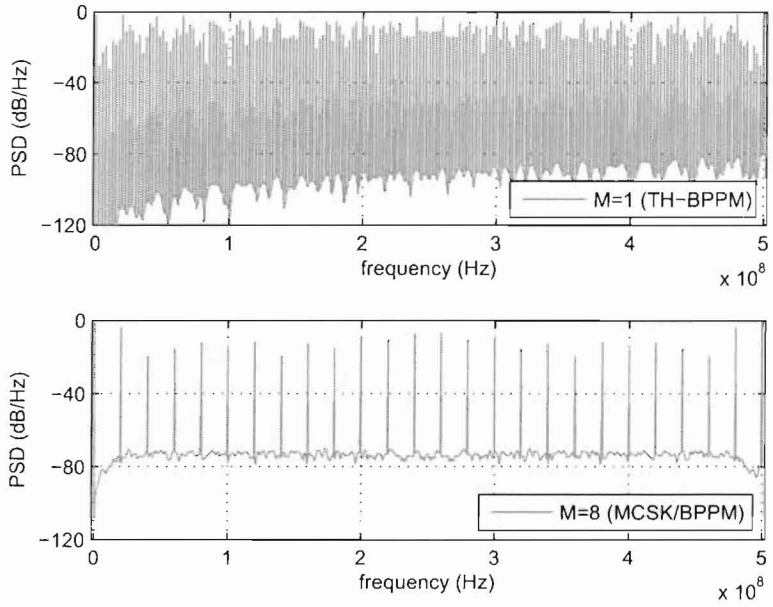


Figure 5.4: Effects of code design-1 on the PPM for *dB/Hz resolution*. Upper plot: PSD resulting from TH-BPPM. Lower plot: PSD resulting from 8-CSK/BPPM.

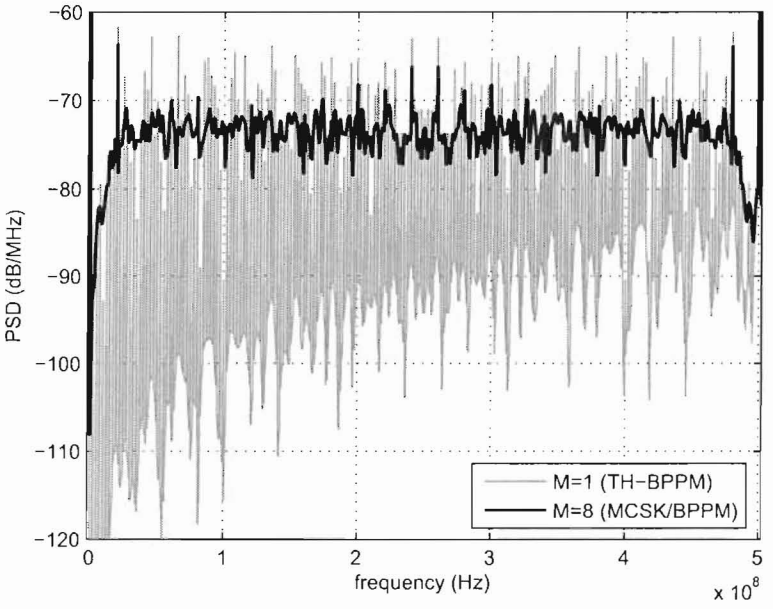


Figure 5.5: Effects of code design-1 on the PPM for *dB/MHz resolution*.

cases, namely TH-BPPM with a finite length TH code, TH-BPPM with random TH and MCSK/BPPM with $M$ finite length TH codes, to the FCC spectrum mask. First of all, all three cases experience large discrete spectral components at the multiples of the chip rate (or TH rate) $1/T_c$, where code design or random hopping does not help to reduce these components [44]. The PSD components that have the highest magnitude can be observed for TH-BPPM and MCSK/BPPM in Fig. 5.5 at the frequencies $k\frac{1}{T_c}$ for $T_c = 2\,ns$ and $\{k = 0, 1\}$. The transmit powers of these modulations are accordingly adjusted to meet the spectrum mask for the maximum value components at $1/T_c$. On the other hand, *random hopping* used with TH-BPPM smooths the continuous spectrum and suppresses the discrete spectral components in between the frequency components that are at the multiples of the TH rate [11]. For this *ideal* case, suppressed continuous and discrete components have more uniform distribution and create less interference to co-existing systems. For MCSK/BPPM, which is a realistic implementation of random TH, the discrete spectrum components are mostly dissolved for the *MHz*-bandwidth resolution and the continuous spectrum has less peaks compared to TH-BPPM as seen in Fig. 5.5. For MCSK/BPPM to exhibit the *ideal* spectrum resulting from random TH, the code length should be $N_p = 1$ and $M$ orthogonal codes should be generated for each possible $N_h$ TH locations, which is unrealistic from the implementation point of view. In any case, MCSK/BPPM improves the spectrum much compared to TH-BPPM and generates less interference to co-existing systems.

Let us now look at the effects of code design technique-1 on PAM. When MCSK is applied to BPAM, it is observed that the resulting PSD is smoothed compared to the PSD of conventional TH-BPAM. Further discussions for this comparison will follow the presentation of code design technique-2.

With the code design technique-1, it is shown that the MCSK-IR shows improved PSD characteristics, especially for BPPM, where it reduces the number of discrete components, resolves most of the remaining discrete components over a MHz bandwidth defined by FCC and exhibits a PSD with the ideal infinite TH code effect. On the other hand, with the limiting constraint of $M$ on $\mathbf{c}_{sub}$, not many users can be simultaneously accommodated due to the limited number of TH codes. Accordingly, two criteria will be considered to evaluate the MA capability, namely the number of distinct code sets and the probability of collision repetition.

Let $\bar{\mathbf{C}}_1 = \left\{\mathbf{C}_1^{(k)} \middle| k = 1, \ldots, N_1\right\}$ be the set that contains all possible distinct sets generated based on Corollary 1. Accordingly, it can be shown that $N_1 = \frac{N_h!}{(N_h-M)!M!}(M!)^{N_p}$.

Let $\{(c_0^{(1)})_0, (c_0^{(1)})_1\}$ and $\{(c_0^{(2)})_0, (c_0^{(2)})_1\}$ be the elements of the code sets $\mathbf{C}_1^{(1)}$ and $\mathbf{C}_1^{(2)}$, respectively, generated independently. It can be shown that $\Pr\left[\left\{(c_0^{(1)})_0 = (c_0^{(1)})_1\right\} \bigcap \left\{(c_0^{(2)})_0 = (c_0^{(2)})_1\right\}\right] = \frac{1}{M^2}$, where the given probability represents the probability of repetition of a possible collision among two code sets (i.e., two users) for two consecutive frame times. It can be deduced from these two criteria that the number of distinct code sets and the probability of collision repetition will depend on $M$, where a small value of $M$ will limit the number of code sets and increase the possibility of collision among two chips, which will indirectly affect the MA capability. To achieve a relatively higher MA capability, let us study another code design technique that does not restrict the use of *different* $M$ TH values per frame time.

### 5.4.2 Code design technique-2

The second code set design technique is mainly considered to allow higher MA capability than code design technique-1, while improving the spectrum with the averaging effect of $M$ TH codes. This technique is based on Corollary 2 given below.

*Corollary 2:* Given the set $\{0, \ldots, N_h - 1\}$ associated with possible time-hopping locations, determine the vectors $\left[(c_0)_i \cdots (c_{M-1})_i\right]^T$ independently for $\forall i$ from ${}_{N_h}P_M$ possible arrangements. Let $\mathbf{C}_2 = \left\{(c_j)_i \,|\, \forall j, \forall i\right\}$ be the resulting code set. Accordingly, MCSK-IRs will have higher MA capability when they use code sets $\{\mathbf{C}_2\}$ compared to using $\{\mathbf{C}_1\}$.

Let us initially compare the MA capabilities of design techniques 1 and 2, followed by the PSD evaluation of design technique-2. Similar to the definition of $\bar{\mathbf{C}}_1$, $\bar{\mathbf{C}}_2 = \{\mathbf{C}_2^{(k)} | k = 1, \ldots, N_2\}$ is the set that contains all possible distinct sets generated based on Corollary 2. Accordingly, it can be shown that $N_2 = \left(\frac{N_h!}{(N_h-M)!}\right)^{N_p}$ and $\bar{\mathbf{C}}_1 \subset \bar{\mathbf{C}}_2$. Moreover, for $\mathbf{C}_2^{(1)}$ and $\mathbf{C}_2^{(2)}$, $\Pr\left[\left\{(c_0^{(1)})_0 = (c_0^{(1)})_1\right\} \bigcap \left\{(c_0^{(2)})_0 = (c_0^{(2)})_1\right\}\right] = \frac{1}{{N_h}^2}$, where $N_h > M$ for typical system parameters. Considering the number of distinct code sets and probability of collision repetition comparisons for the two techniques, it can be concluded that code design technique-2 can provide higher MA capability. For more accurate analysis of MA capabilities, system performances should be evaluated under multi-user scenario, which is beyond the scope of this chapter.

While the code design technique-2 improves the MA capability, it does not reduce the number of discrete spectral components, where the discrete components of MCSK/BPPM under Corollary 2 occur at multiples of $\frac{1}{N_p T_f}$ contrary to the discrete components occurring

at $\frac{1}{T_f}$ under Corollary 1. This can be explained by *effective* $N_p$ to be the same as the parameter $N_p$. On the other hand, the averaging effect will smooth the continuous spectrum and suppress the discrete PSD components similar to Corollary 1.

For $M = 8$ and $N_h = 16$, the code set $\mathbf{C}_2$ is generated based on Corollary 2.

$$\mathbf{C}_2 = \begin{bmatrix} 6 & 3 & 11 & 2 & 11 & 13 & 10 & 1 \\ 4 & 15 & 12 & 15 & 0 & 9 & 9 & 7 \\ 3 & 1 & 8 & 12 & 4 & 2 & 15 & 9 \\ 13 & 5 & 8 & 6 & 14 & 0 & 13 & 8 \\ 5 & 0 & 7 & 8 & 10 & 11 & 2 & 11 \\ 12 & 8 & 10 & 2 & 9 & 4 & 12 & 4 \\ 9 & 14 & 3 & 5 & 1 & 14 & 4 & 13 \\ 10 & 6 & 4 & 7 & 8 & 15 & 3 & 0 \end{bmatrix} \tag{5.20}$$

Figs. 5.6 and 5.7 show the PSDs of the conventional TH-BPPM ($M = 1$) with the TH code $\mathbf{c}_0$ (the first row of $\mathbf{C}_2$) and of 8-CSK/BPPM ($M = 8$) with the TH code set $\mathbf{C}_2$ for two different PSD resolutions. In Fig. 5.6, it is observed that 8-CSK/BPPM (lower plot) shows similar PSD characteristics with respect to 8-CSK/BPPM in Fig. 5.4 (i.e., smooth continuous spectrum, suppressed discrete components) except for more discrete components. Contrary to more components, it is measured that the average power of each discrete spectral component in Fig. 5.6 is $(10 \log_{10} N_p)$ dB less than the average power of each discrete spectral component in Fig. 5.4. As a result, the total power of discrete spectral components is conserved. With the FCC constraints in Fig. 5.7, it can be seen that almost all of the discrete components are resolved for the given resolution for 8-CSK/BPPM, whereas the PSD in Fig. 5.5 exhibits noticeable peaky power components due to discrete components in the $[200, 300]$ MHz range. Although code design technique-2 may seem more advantageous for BPPM when FCC resolution is considered, code design technique-1 may be preferred to accommodate narrowband systems over its $\frac{1}{T_f}$ bandwidth (typically 10-20 MHz).

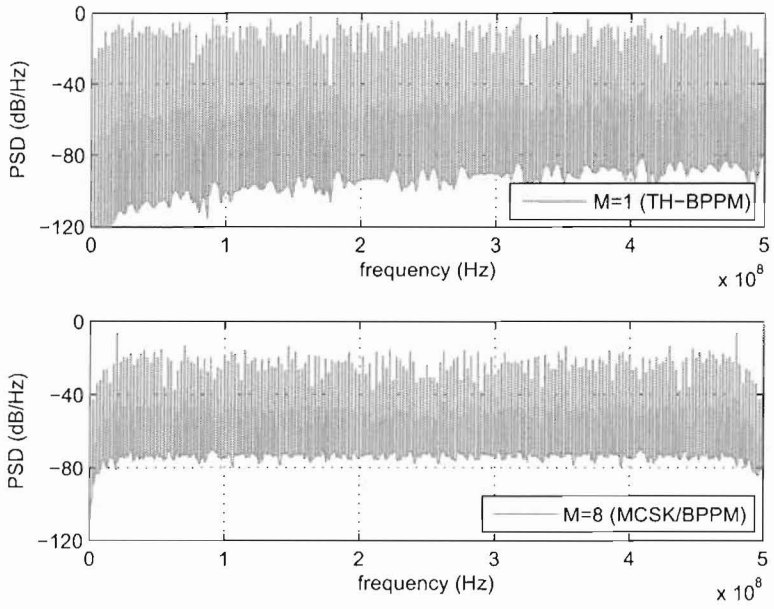


Figure 5.6: Effects of code design-2 on the PPM for *dB/Hz resolution*. Upper plot: PSD resulting from TH-BPPM. Lower plot: PSD resulting from 8-CSK/BPPM.

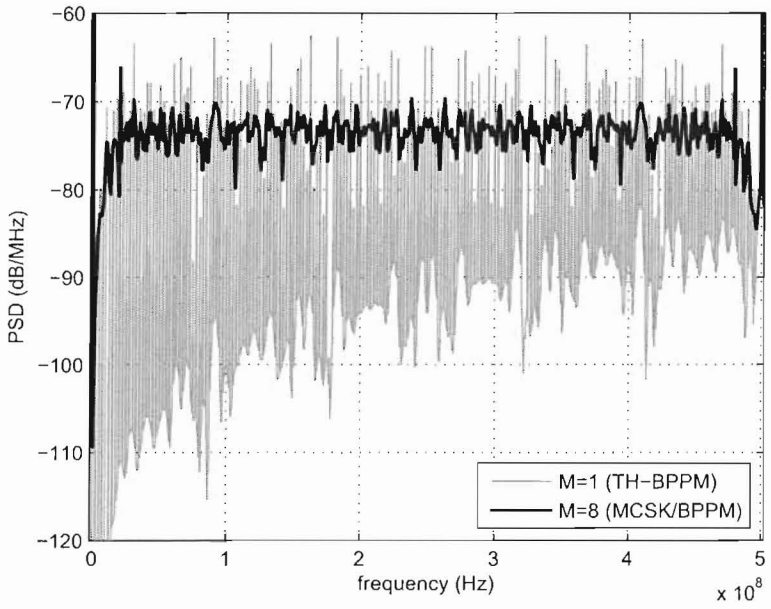


Figure 5.7: Effects of code design-2 on the PPM for *dB/MHz resolution*.

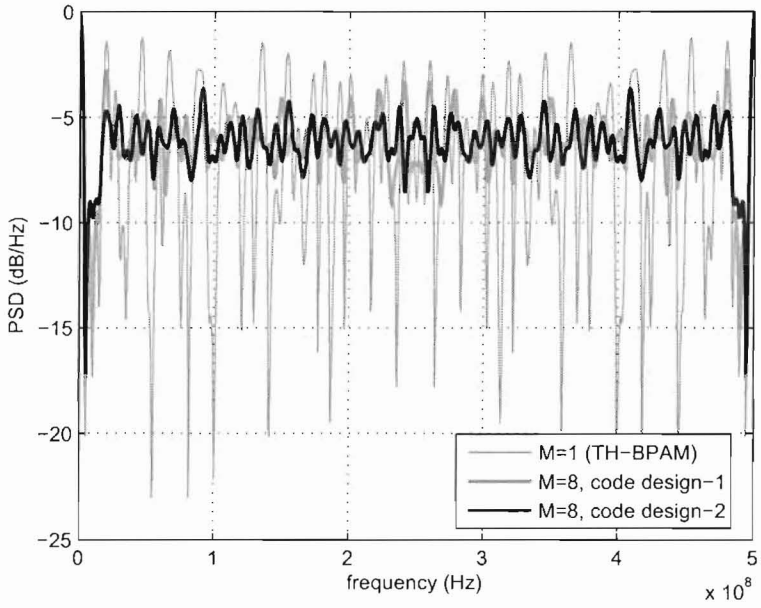


Figure 5.8: Effects of code design on the PAM for two different code sets.

In Fig. 5.8, the PSDs resulting from the two different code sets, $\mathbf{C}_1$ and $\mathbf{C}_2$, are compared to the PSD resulting from TH-BPAM ($M = 1$) when 8-CSK/BPAM ($M = 8$) is used. It is observed that PSDs resulting from 8-CSK/BPAM exhibit the similar averaging effect, resulting in a smoother spectrum compared to the conventional TH-BPAM ($M = 1$). It is to be noted that code design technique-2 can support higher MA capability for similar PSD characteristics for PAM. Therefore, it may be preferred to code design technique-1 for MCSK/BPAM.

### 5.4.3 Code design for TH-IRs

TH code sets designed for MCSK-IRs can also be used for conventional TH-IRs in order to improve their spectrum. While MCSK-IRs were designed to increase the data rate with a slightly increased receiver structure [70], conventional TH-IRs can retain their main transceiver structure [40], use a TH code synchronization procedure that is known to both the transmitter and the receiver, and randomly select one of the TH codes every $N_p T_f$ as

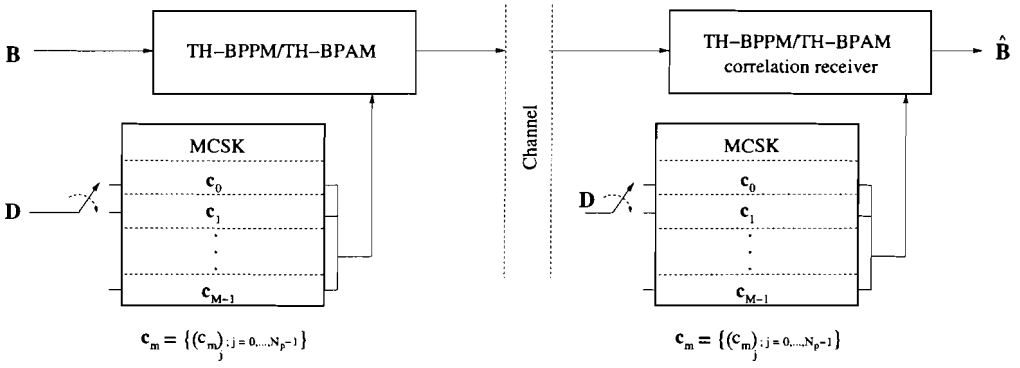


Figure 5.9: Modified TH-IR transceiver.

MCSK-IRs. Accordingly, the conventional TH-IRs can achieve the same spectral characteristics as MCSK-IRs. The transceiver structure of a modified TH-IR is depicted in Fig. 5.9 for the transmission of **B** with the pseudorandom sequence **D** that controls the selection of a TH code from a set of $M$ distinct TH codes. **D** should be synchronized at the transmitter and receiver for data detection purposes. With the transmit/receive structures retained the same, the *modified* TH-IR transceiver can provide improved PSD characteristics over the conventional IR.

## 5.5 Conclusion

In this chapter, the effects of different code design techniques on the PSD and the MA capability of MCSK based IRs were investigated. Initially, the PSD that accounts for TH code changes within a frame time was derived and verified, followed by the evaluation of two different TH code set design techniques. The first technique significantly reduces the number of discrete spectral components for the MCSK/BPPM format with a limited MA capability. The second technique increases the MA capability with a smoothed continuous spectrum. Moreover, these techniques can be adopted to conventional TH-IRs without much increasing the hardware complexity in order to improve their spectrum.

The next chapter summarizes the contributions of the investigations covered in Chapters 3–5 and concludes this dissertation.

# Chapter 6

# Conclusions

In this dissertation, a new ultra wideband impulse radio (UWB-IR) modulation format, namely $M$-ary code shift keying (MCSK) impulse modulation, was presented. The main motivation for proposing a new modulation format was to address some of the problems associated with the conventional UWB-IR modulations. Based on the proposed MCSK impulse modulation, three main investigations were conducted. In each investigation, specific considerations of MCSK impulse modulation were analyzed and compared to the conventional UWB-IR modulations to show the system improvements provided. In the following, a summary of the contributions of the proposed MCSK impulse modulation and the future research directions are presented.

## 6.1 Summary of Contributions

By proposing MCSK impulse modulation, three main contributions are made to the UWB-IR communications area as summarized below:

1. In Chapter 3, MCSK impulse modulation is shown to improve the system performance of UWB-IRs by randomizing pulse transmit locations, when compared to the conventional time-hopping $M$-ary pulse position modulation (TH-MPPM) that uses consecutive pulse transmit locations.

2. In Chapter 4, MCSK impulse modulation combined with binary PPM (BPPM) is shown to increase the data rate of the conventional TH-BPPM and improve the system performance at the same time by appropriately selecting system design parameters.

3. In Chapter 5, MCSK impulse modulation combined with BPPM and binary pulse amplitude modulation (BPAM) is shown to improve the power spectral density (PSD) characteristics of the conventional TH-BPPM and TH-BPAM by increasing the effective TH code period and suppressing the undesired peaks in the PSD.

Specific contributions in each investigation are detailed in the following.

**MCSK Impulse Modulation**

MCSK impulse modulation was proposed and studied as the first investigation. The main property of MCSK impulse modulation is that it is designed to randomize the consecutive pulse transmit locations used in the conventional TH-MPPM. When practical implementations of MCSK and TH-MPPM were considered, it was shown that MCSK can provide about *2 dB performance gain over TH-MPPM* as it reduces the effects of multipath delays on the decision variables by randomizing pulse transmit locations. This performance gain is mainly a result of the separated $M$ decision variables experiencing less interference terms due to the decaying power delay profile. In addition to the improved system performance provided by MCSK, some other contributions are summarized as follows:

- Lower and upper bounds on the symbol-error rate (SER) were derived in the commonly used approximate $T_c$-spaced channel model for both single- and multi-user cases. The effects of CM-1 and CM-3 channel types and the pulse repetition number $N_s$ on the system performances were discussed in detail.

- For the single-user case, the effect of multipath-delayed pulses on $M$ decision variables was explicitly provided in terms of channel impulse response coefficients.

- For the multi-user case, an accurate semi-analytic SER expression was derived based on modelling the multi-user interference (MUI) terms with the generalized Gaussian distribution (GGD), where some approximations to MUI modelling were made that increased the computational efficiency of numerical analysis significantly with respect to the simulation studies, while still providing accurate results.

- Simulation studies were conducted in the accurate $\tau$-spaced channel model, and an implementable partial-Rake receiver was used. Accordingly, the 2 dB performance gain reported in the dissertation is important since the study considered a realistic channel model and a practical Rake implementation.

### MCSK Combined with BPPM

MCSK impulse modulation combined with BPPM was proposed and studied as the second investigation. The main property of the combined MCSK/BPPM is that it is designed to transmit additional $\log_2 M$-bit data through the selection of one of the $M$ TH codes per user, in addition to the one-bit transmitted by TH-BPPM. By controlling the data rate with the appropriate selection of system design parameters $M$, the modulation order, $N_p$, the TH code length, and $N_s$, the pulse repetition number, and using a maximum-likelihood sequence estimation (MLSE) structure at the receiver, it is shown that the combined MCSK/BPPM can achieve *better bit-error-rate (BER) performance than the conventional TH-BPPM system with increased data rate.* In addition to the increased data rate with improved system performance provided by MCSK/BPPM, some other contributions are summarized as follows:

- Lower and upper bounds on the SER were derived in an additive white Gaussian noise (AWGN) channel for the multi-user case. The effects of system parameters $M$, $N_p$ and $N_s$ on the system performance were discussed in detail while verifying the analysis.
- In order to model the MUI accurately, characteristic functions of the MUI terms were derived. For that, characteristic functions used to model the MUI in TH-BPPM signalling [15] were extended to include the MUI in MCSK/BPPM signalling.
- Considering the performance result of MCSK/BPPM (i.e., increased data rate with improved system performance), it is suggested that the proposed modulation can be used for for high-rate applications of IEEE 802.15.3a or low-rate applications of IEEE 802.15.4a. While MCSK/BPPM can be implemented for high-rate applications with the structure it is presented in the dissertation, the data rate can be traded-off with the frame time in order to mitigate the worse effects of multipath and multiple access interference, providing more accurate time-of-arrival estimation for low-rate applications.

### PSD Characteristics of MCSK Based Impulse Radios

PSD characteristics of MCSK based impulse radios (i.e., MCSK impulse modulation combined with BPPM and BPAM) were studied as the third investigation. In a conventional UWB-IR system, finite-length TH codes used for multiple-access cause undesired peaks in

the PSD due to the periodicity of TH codes. On the other hand, MCSK randomly selects one of the $M$ TH codes every TH code period, which results in increased effective TH code period with respect to the conventional TH-BPPM and TH-BPAM. This increase in effective TH code period *improves the PSD of MCSK based IRs with respect to the PSD of conventional UWB-IRs* as it helps smoothing the continuous spectrum and suppressing the discrete spectral components. In addition to the improved PSD characteristics provided by MCSK based IRs, some other contributions are summarized as follows:

- In the literature, PSD characteristics are usually given only by analysis or simulation. For the PSD investigation in this dissertation, an exact PSD that accounts for every TH code change within a frame time was derived and verified. This way, the reliability of the presented results was increased.
- Two different TH code set design techniques were proposed and studied in order to assess the trade-off between multiple-access (MA) capability and efficient spectrum shaping. The first technique significantly reduces the number of discrete spectral components for the MCSK/BPPM format with a limited MA capability. The second technique increases the MA capability with a smoothed continuous spectrum.
- Finally, suggestions were made to adopt the MCSK structure to conventional UWB-IRs. The proposed structure can provide the same PSD as the MCSK based IRs without much increasing the hardware complexity.

In summary, proposing MCSK impulse modulation has resulted in several contributions including BER performance improvement, data rate increase and PSD improvement with respect to the conventional UWB-IRs. In the last part of the dissertation, some suggestions are made for future research work as an extension to the proposed MCSK impulse modulation considered in this dissertation.

## 6.2 Future Research

MCSK impulse modulation proposed in this dissertation has the potential to be used in some other investigations in UWB-IR communications. These investigations are not limited to, but include the following:

- MCSK impulse modulation was studied only for the implementation of the *basic* UWB-IR in this dissertation. Another suitable implementation of the MCSK impulse modulation is for the emerging IEEE 802.15.4a standard. The current implementation of the physical layer of IEEE 802.15.4a uses combined BPPM and BPAM with two orthogonal pulse transmit locations, limited time-hopping per user and fixed guard bands. In the presence of multiple simultaneously operating piconets, there may be catastrophic collisions due to limited TH and fixed guard bands. Depending on user asynchronism values, there may occur more collisions that may lead to many packet losses. In [79], we replaced BPPM with binary CSK (BCSK), and used a simple TH code design technique and *adaptive* guard bands. This approach made the collision event uniformly distributed and independent of the user asynchronism values. Accordingly, it was shown that the worst case collisions and performances can be prevented by replacing BPPM with BCSK. Although only BCSK was considered for that study, a general MCSK approach is of future interest. With the optional higher data rates allowed in the IEEE 802.15.4a standard [4], $M$-ary CSK is also an option to increase the data rate, in addition to preventing worst case collisions due to fixed guard bands. An investigation that studies the implementation of MCSK for IEEE 802.15.4a to increase the data rate and to analyze the outage probability (with respect to BPPM used with fixed guard bands) is a possible future investigation.

- In Chapter 4, it was concluded that the improved system performance at increased data rate provided by MCSK/BPPM can be used for low-rate applications. By trading-off the data rate, the frame time can be increased in order to increase the number of possible TH locations and to resolve the multipath-delayed pulses. With this approach, further improved system performances at various data rates can be studied. Also, different signal processing techniques can be employed to study the location and ranging capabilities of the MCSK modulation in order to compare to the other modulations. This study may be conducted for either basic UWB-IRs or for the physical layer of IEEE 802.15.4a.

- Two TH code set design techniques were presented in Chapter 5. Both techniques were proposed to suppress the undesired peaks in the PSD. Another interest is in generating spectral nulls for the frequency bands of co-existing systems. Based on the accurate PSD derived, TH code sets of MCSK based impulse radios may be designed

to generate spectral nulls and smooth the PSD at the same time.

- Only the IEEE 802.15.3a channel model was used in this dissertation. This model consists of four channel types (CM1–CM4), which cover only the indoor environment up to 10 m range. An interesting study would be to consider the IEEE 802.15.4a channel model for the comparison of MCSK and MPPM. With more measurement environments (e.g., indoor residential, indoor office, outdoor, industrial environments, etc.) given up to 28 m in this model, MCSK and MPPM may be studied to determine the specific environments and ranges, where MCSK outperforms MPPM.

- Independent of the study of MCSK impulse modulation, there are some other issues that should be considered in future UWB-IR research. These include

  (i) accurate modelling of the MUI for more accurate analysis,

  (ii) not neglecting the effect of inter-pulse interference for more realistic results,

  (iii) proposing different transceiver structures for performance improvements, and

  (iv) further studies for achieving closed-form BERs.

# Appendix A

# Modelling MUI Using the GGD

In the following, the procedure of representing the MUI term $I_{d_0,m}$ with its equivalent GGD $f_{I_{d_0,m}}(x)$ is presented. Modelling the MUI with the GGDs is first proposed in [66], where the GGDs are used to fit the distribution of the MUI term $I_{d_0,m}$. These distributions can be represented by [80]

$$f_{I_{d_0,m}}(x) = \frac{c_1(\beta)}{\sqrt{\sigma^2}} \exp\left(-c_2(\beta)\left|\frac{x}{\sqrt{\sigma^2}}\right|^{\frac{2}{1+\beta}}\right) \tag{A.1}$$

$$\text{with} \quad c_1(\beta) = \frac{\Gamma^{\frac{1}{2}}\left(\frac{3}{2}(1+\beta)\right)}{(1+\beta)\Gamma^{\frac{3}{2}}\left(\frac{1}{2}(1+\beta)\right)} \quad \text{and} \quad c_2(\beta) = \left[\frac{\Gamma\left(\frac{3}{2}(1+\beta)\right)}{\Gamma\left(\frac{1}{2}(1+\beta)\right)}\right]^{\frac{1}{1+\beta}}$$

where $\beta > -1$ and $\Gamma(x) = \int_0^\infty u^{x-1}e^{-u}du$ is the Gamma function. The $n$th-order moment of the absolute value of a generalized Gaussian variable is given by [81]

$$\mathbf{E}(|x|^n) = \frac{\Gamma\left(\frac{n+1}{\alpha}\right)}{\Gamma\left(\frac{1}{\alpha}\right)}\left(\sqrt{\frac{\Gamma\left(\frac{1}{\alpha}\right)}{\Gamma\left(\frac{3}{\alpha}\right)}\sigma^2}\right)^n \quad \text{with} \quad \alpha = \frac{2}{1+\beta} \tag{A.2}$$

where $\mathbf{E}(\cdot)$ is the expected value operator and $\sigma^2 = \mathbf{E}(x^2)$ is the variance of the GGD. Based on (A.2), the relation between the kurtosis $\gamma = \frac{\mathbf{E}(x^4)}{\mathbf{E}(x^2)^2} - 3$ and $\beta$ can be obtained as [66]

$$\gamma = \frac{\Gamma\left(\frac{5(1+\beta)}{2}\right)\Gamma\left(\frac{(1+\beta)}{2}\right)}{\left(\Gamma\left(\frac{3(1+\beta)}{2}\right)\right)^2} - 3. \tag{A.3}$$

This means that by estimating the second and fourth moments of the MUI term distribution, the kurtosis value $\gamma$ can be obtained, which then can be used to find the corresponding $\beta$

value. Once the $\beta$ value is determined, the GGD $f_{I_{d_0,m}}(x)$ that models the distribution of $I_{d_0,m}$ can be obtained, since it is only a function of $\beta$ and $\sigma^2$.

When TH-MPPM is considered, $I_{d_0,m} = (I_{d_0} - I_m)$ is simulated for the given $(d_0, m)$-pair for different channel realizations and user delay values given in (3.9). For MCSK, different combinations of $\{C_j\}$ are taken into account for the given $(d_0, m)$-pair. After simulation values are obtained for $I_{d_0,m}$, the second and fourth moments are calculated in order to find the corresponding $\beta$-values and the GGDs $f_{I_{d_0,m}}(x)$ and $f_{I_{d_0,m}(\{C_j\})}(x)$, respectively, for TH-MPPM and MCSK. These distributions are then used in (3.24) to find $\Phi_{I_{d_0,m}}(\omega)$, the CF of the MUI term.

# Appendix B

# Characteristic Functions of $I_0$ & $I_n$

The characteristic functions of $I_0$ and $I_n$ are derived as follows. First, $I_0$ given in (4.21) can be rewritten using (4.15) as

$$I_0 = \sum_{k=2}^{N_u} A_k \left\{ \sum_{j=(i-1)N_s}^{(i-1)N_s+\gamma_k-1} \left[ R\left(\theta^0_{i,d_i^{(1)}}\right) - R\left(\theta^0_{i,d_i'^{(1)}}\right) \right] + \sum_{j=(i-1)N_s+\gamma_k}^{iN_s-1} \left[ R\left(\theta^0_{(i+1),d_i^{(1)}}\right) - R\left(\theta^0_{(i+1),d_i'^{(1)}}\right) \right] \right\} \tag{B.1}$$

where

$$\theta^0_{i,d_i^{(1)}} = \alpha_k + \left[ (c^{(k)}_{m_i})_j - (c^{(1)}_0)_j \right] T_c + \left[ d_i^{(k)} - d_i^{(1)} \right] \delta_d \tag{B.2}$$

$$\theta^0_{(i+1),d_i^{(1)}} = \alpha_k + \left[ (c^{(k)}_{l_{(i+1)}})_j - (c^{(1)}_0)_j \right] T_c + \left[ d^{(k)}_{(i+1)} - d_i^{(1)} \right] \delta_d. \tag{B.3}$$

Further, (B.1) can be rewritten as $I_0 = \sum_{k=2}^{N_u} A_k I_0^{(k)} = \sum_{k=2}^{N_u} A_k \left( X_0^{(k)} + Y_0^{(k)} \right)$ with

$$X_0^{(k)} = \sum_{j=(i-1)N_s}^{(i-1)N_s+\gamma_k-1} \left[ R\left(\theta^0_{i,d_i^{(1)}}\right) - R\left(\theta^0_{i,d_i'^{(1)}}\right) \right] \tag{B.4}$$

$$Y_0^{(k)} = \sum_{j=(i-1)N_s+\gamma_k}^{iN_s-1} \left[ R\left(\theta^0_{(i+1),d_i^{(1)}}\right) - R\left(\theta^0_{(i+1),d_i'^{(1)}}\right) \right]. \tag{B.5}$$

To find the characteristic function of $X_0^{(k)}$, initially the probability density functions (pdf's) of $\theta^0_{i,d_i^{(1)}}$ and $\theta^0_{i,d_i'^{(1)}}$ should be known. Since the TH codes in $\left[ (c^{(k)}_{m_i})_j - (c^{(1)}_0)_j \right]$ are independent and uniformly distributed, the pdf's of $\theta^0_{i,d_i^{(1)}}$ and $\theta^0_{i,d_i'^{(1)}}$ are identical for a given

$\alpha_k$ when conditioned on $\left[d_i^{(k)} - d_i^{(1)}\right]$ and $\left[d_i^{(k)} - d_i^{\prime(1)}\right]$, respectively. Then it can be shown to

$$f_{\theta^0_{i,x}|d,\alpha}\Big(\theta \,\Big|\, \left[d_i^{(k)} - x\right] = d, \alpha_k = \alpha\Big) = \frac{1}{{N_h}^2} \sum_{h=-(N_h-1)}^{N_h-1} \Big(N_h - |h|\Big)\delta_d\Big(\theta - hT_c - d\delta_d - \alpha\Big) \quad \text{(B.6)}$$

where $x \in \left\{d_i^{(1)}, d_i^{\prime(1)}\right\}$. Using [15, eqs. (21,23-24)] and the equal probability conditions of $\left\{d_i^{(k)} \in \{0,1\}; d_i^{(1)} \in \{0,1\}\right\}$ in $\left\{d_1 = \left[d_i^{(k)} - d_i^{(1)}\right]; d_2 = \left[d_i^{(k)} - d_i^{\prime(1)}\right]\right\}$ pairs, the CF of $X_0^{(k)}$ conditioned on $\alpha_k$ and $\gamma_k$ can be evaluated as

$$\begin{aligned}\Phi_{X_0^{(k)}|\alpha,\gamma}(\omega) &= \sum_{\{d_1,d_2\}} \Pr\left[\{d_1,d_2\}\right] \Phi_{X_0^{(k)}|\{d_1,d_2\},\alpha,\gamma}(\omega) \\ &= \frac{1}{2{N_h}^{2\gamma}} \left[ \left( \sum_{h=-(N_h-1)}^{N_h-1} \Big(N_h - |h|\Big) e^{jw\left[R(\alpha+hT_c) - R(\alpha+hT_c-\delta_d)\right]} \right)^{\gamma} \right. \\ &\quad \left. + \left( \sum_{h=-(N_h-1)}^{N_h-1} \Big(N_h - |h|\Big) e^{jw\left[R(\alpha+hT_c+\delta_d) - R(\alpha+hT_c)\right]} \right)^{\gamma} \right]. \end{aligned} \quad \text{(B.7)}$$

Similarly, the CF of $Y_0^{(k)}$ conditioned on $\alpha$ and $\gamma$ can be evaluated as

$$\begin{aligned}\Phi_{Y_0^{(k)}|\alpha,\gamma}(\omega) = \frac{1}{2{N_h}^{2(N_s-\gamma)}} \cdot &\left[ \left( \sum_{h=-(N_h-1)}^{N_h-1} \Big(N_h - |h|\Big) e^{jw\left[R(\alpha+hT_c) - R(\alpha+hT_c-\delta_d)\right]} \right)^{(N_s-\gamma)} \right. \\ &\left. + \left( \sum_{h=-(N_h-1)}^{N_h-1} \Big(N_h - |h|\Big) e^{jw\left[R(\alpha+hT_c+\delta_d) - R(\alpha+hT_c)\right]} \right)^{(N_s-\gamma)} \right]. \end{aligned} \quad \text{(B.8)}$$

Thus the CF of $I_0^{(k)}$ conditioned on $\alpha$ and $\gamma$ is derived as

$$\Phi_{I_0^{(k)}|\alpha,\gamma}(\omega) = \Phi_{X_0^{(k)}|\alpha,\gamma}(\omega)\, \Phi_{Y_0^{(k)}|\alpha,\gamma}(\omega). \quad \text{(B.9)}$$

To find the CF of $I_n^{(k)}$ conditioned on $\alpha$ and $\gamma$, we follow a similar procedure by rewriting $I_n$ and finding the pdf's of the variables that contribute to the noise term. $I_n$ can be rewritten using (4.15) as

$$\begin{aligned} I_n = \sum_{k=2}^{N_u} A_k \sum_{i=1}^{N_p/N_s} \Bigg\{ &\sum_{j=(i-1)N_s}^{(i-1)N_s+\gamma_k-1} \left[ R\Big(\theta^n_{i,d_i^{(1)}}\Big) - R\Big(\theta^n_{i,v_i}\Big) \right] \\ &+ \sum_{j=(i-1)N_s+\gamma_k}^{iN_s-1} \left[ R\Big(\theta^n_{(i+1),d_i^{(1)}}\Big) - R\Big(\theta^n_{(i+1),v_i}\Big) \right] \Bigg\} \end{aligned} \quad \text{(B.10)}$$

where

$$\theta^n_{i,d_i^{(1)}} = \alpha_k + \left[(c^{(k)}_{m_i})_j - (c^{(1)}_0)_j\right]T_c + \left[d_i^{(k)} - d_i^{(1)}\right]\delta_d \quad \text{(B.11)}$$

$$\theta^n_{i,v_i} = \alpha_k + \left[(c^{(k)}_{m_i})_j - (c^{(1)}_n)_j\right]T_c + \left[d_i^{(k)} - v_i\right]\delta_d \quad \text{(B.12)}$$

$$\theta^n_{(i+1),d_i^{(1)}} = \alpha_k + \left[(c^{(k)}_{l_{(i+1)}})_j - (c^{(1)}_0)_j\right]T_c + \left[d_{(i+1)}^{(k)} - d_i^{(1)}\right]\delta_d \quad \text{(B.13)}$$

$$\theta^n_{(i+1),v_i} = \alpha_k + \left[(c^{(k)}_{l_{(i+1)}})_j - (c^{(1)}_n)_j\right]T_c + \left[d_{(i+1)}^{(k)} - v_i\right]\delta_d. \quad \text{(B.14)}$$

Then (B.10) can be rewritten as $I_n = \sum_{k=2}^{N_u} A_k I_n^{(k)} = \sum_{k=2}^{N_u} A_k \left\{\sum_{i=1}^{N_p/N_s}\left(X_{n,i}^{(k)} + Y_{n,i}^{(k)}\right)\right\}$ with

$$X_{n,i}^{(k)} = \sum_{j=(i-1)N_s}^{(i-1)N_s+\gamma_k-1}\left[R\left(\theta^n_{i,d_i^{(1)}}\right) - R\left(\theta^n_{i,v_i}\right)\right] \quad \text{(B.15)}$$

$$Y_{n,i}^{(k)} = \sum_{j=(i-1)N_s+\gamma_k}^{iN_s-1}\left[R\left(\theta^n_{(i+1),d_i^{(1)}}\right) - R\left(\theta^n_{(i+1),v_i}\right)\right]. \quad \text{(B.16)}$$

Since the TH codes in (B.11) and (B.12) are uniformly distributed and independent, the pdf's of $\theta^n_{i,d_i^{(1)}}$ and $\theta^n_{i,v_i}$ when conditioned on $[d_i^{(k)} - d_i^{(1)}]$ and $[d_i^{(k)} - v_i]$, respectively, for a given $\alpha_k$, and based on the TH code design condition $\left\{(c_0^{(1)})_j \neq (c_n^{(1)})_j; \forall j\right\}$, can be shown to

$$f_{\theta^n_{i,d_i^{(1)}}|d_1,\alpha}\left(\theta \left| \left[d_i^{(k)} - d_i^{(1)}\right] = d_1, \alpha_k = \alpha\right.\right) = \frac{1}{{N_h}^2(N_h-1)}\sum_{\mathbf{h_1},\mathbf{h_2}}\delta_d\left(\theta - h_1T_c - d_1\delta_d - \alpha\right)$$

$$f_{\theta^n_{i,v_i}|d_2,\alpha}\left(\theta \left| \left[d_i^{(k)} - v_i\right] = d_2, \alpha_k = \alpha\right.\right) = \frac{1}{{N_h}^2(N_h-1)}\sum_{\mathbf{h_1},\mathbf{h_2}}\delta_d\left(\theta - h_2T_c - d_2\delta_d - \alpha\right) \quad \text{(B.17)}$$

where $\mathbf{h_1} = \left[(c^{(k)}_{m_i})_j - (c^{(1)}_0)_j\right]$, $\mathbf{h_2} = \left[(c^{(k)}_{m_i})_j - (c^{(1)}_n)_j\right]$, and

$$\sum_{\mathbf{h_1},\mathbf{h_2}} = \sum_{(c^{(k)}_{m_i})_j=0}^{N_h-1}\sum_{(c^{(1)}_0)_j=0}^{N_h-1}\sum_{\{(c^{(1)}_n)_j=0,\,(c^{(1)}_n)_j\neq(c^{(1)}_0)_j\}}^{N_h-1}$$

is used for a simplified representation. Using [15, eqs. (21,23-24)] and the equal probability conditions of $\{d_i^{(k)}\}$, the CF of $X_{n,i}^{(k)}$ conditioned on $\alpha_k$ and $\gamma_k$ can be evaluated as

$$\Phi_{X_{n,i}^{(k)}|\alpha,\gamma}(\omega) = \Pr\left[d_i^{(k)} = 0\right]\Phi_{X_{n,i}^{(k)}|\{d_1,d_2\},\alpha,\gamma}(\omega) + \Pr\left[d_i^{(k)} = 1\right]\Phi_{X_{n,i}^{(k)}|\{d_1,d_2\},\alpha,\gamma}(\omega)$$

$$= \frac{1}{2}\left(\frac{1}{{N_h}^2(N_h-1)}\right)^{\gamma} \cdot \left[\left(\sum_{\mathbf{h_1},\mathbf{h_2}} e^{jw\left[R(\alpha+h_1T_c-d_i^{(1)}\delta_d)-R(\alpha+h_2T_c-v_i\delta_d)\right]}\right)^{\gamma} + \left(\sum_{\mathbf{h_1},\mathbf{h_2}} e^{jw\left[R(\alpha+h_1T_c+[1-d_i^{(1)}]\delta_d)-R(\alpha+h_2T_c+[1-v_i]\delta_d)\right]}\right)^{\gamma}\right]. \quad \text{(B.18)}$$

Similarly, the CF of $Y_{n,i}^{(k)}$ conditioned on $\alpha$ and $\gamma$ can be evaluated as

$$\Phi_{Y_{n,i}^{(k)}|\alpha,\gamma}(\omega) = \frac{1}{2}\left(\frac{1}{{N_h}^2(N_h-1)}\right)^{(N_s-\gamma)} \cdot \left[\left(\sum_{\mathbf{h_1},\mathbf{h_2}} e^{jw\left[R(\alpha+h_1T_c-d_i^{(1)}\delta_d)-R(\alpha+h_2T_c-v_i\delta_d)\right]}\right)^{(N_s-\gamma)} + \left(\sum_{\mathbf{h_1},\mathbf{h_2}} e^{jw\left[R(\alpha+h_1T_c+[1-d_i^{(1)}]\delta_d)-R(\alpha+h_2T_c+[1-v_i]\delta_d)\right]}\right)^{(N_s-\gamma)}\right]. \quad \text{(B.19)}$$

Hence, the CF's of $I_{n,i}^{(k)}$ and $I_n^{(k)}$ conditioned on $\alpha$ and $\gamma$ are respectively derived as

$$\Phi_{I_{n,i}^{(k)}|\alpha,\gamma}(\omega) = \Phi_{X_{n,i}^{(k)}|\alpha,\gamma}(\omega)\,\Phi_{Y_{n,i}^{(k)}|\alpha,\gamma}(\omega) \quad \text{(B.20)}$$

$$\Phi_{I_n^{(k)}|\alpha,\gamma}(\omega) = \prod_{i=1}^{N_p/N_s} \Phi_{I_{n,i}^{(k)}|\alpha,\gamma}(\omega) \quad \text{(B.21)}$$

because of the independent data sequences and TH codes.

After deriving the CF's of $I_0^{(k)}$ and $I_n^{(k)}$ conditioned on $\alpha$ and $\gamma$, the CF of $I_m$ is evaluated for $I_0$ $(m=0)$ and $I_n$ $(m=n)$, respectively. From the uniform distribution of $\gamma_k$, the CF of $I_m^{(k)}$ conditioned on $\alpha$ is

$$\Phi_{I_m^{(k)}|\alpha}(\omega) = \frac{1}{N_s}\sum_{\gamma=0}^{N_s-1} \Phi_{I_m^{(k)}|\alpha,\gamma}(\omega). \quad \text{(B.22)}$$

Again, from the uniform distribution of $\alpha_k$, the CF of the interference term due to the $k$th user is

$$\Phi_{I_m^{(k)}}(\omega) = \frac{1}{T_f}\int_{-T_f/2}^{T_f/2} \Phi_{I_m^{(k)}|\alpha}(\omega), \quad \text{(B.23)}$$

which finally yields the CF of $I_m$ consisting of independent interference terms as

$$\Phi_{I_m}(\omega) = \prod_{k=2}^{N_u} \Phi_{I_m^{(k)}}(A_k w). \quad \text{(B.24)}$$

# Appendix C

# Simplified ACF

$R_{cc}(\tau)$ is periodic with $N_pT_f$. Therefore, the time average ACF of $c(t)$ should be evaluated. By definition,

$$R_{cc}(\tau) = \frac{1}{N_pT_f}\int_0^{N_pT_f} \mathbf{E}\{c(t)c(t+\tau)\}dt \tag{C.1}$$

is the temporal and statistical average ACF of $c(t)$, where

$$c(t) = \begin{cases} \sum_{l=0}^{L-1}\sum_{h=0}^{N_s-1} a_l \delta\Big(t - k(N_pT_f) - t_0\Big), & \text{if } k = 0 \\ 0, & \text{if } k \neq 0 \end{cases} \tag{C.2}$$

with $t_0 = \big(lT_b + hT_f + (c_{m_0})_{(lN_s+h)}T_c + d_l\delta_d\big)$ for the given integration interval and

$$c(t+\tau) = \sum_{k'=-\infty}^{\infty}\sum_{l'=0}^{L-1}\sum_{h'=0}^{N_s-1} a_{l'}\,\delta\Big(t + \tau - k'(N_pT_f) - t_1\Big) \tag{C.3}$$

with $t_1 = \big(l'T_b + h'T_f + (c_{m_{k'}})_{(l'N_s+h')}T_c + d_{l'}\delta_d\big)$. Accordingly, (C.1) can be rewritten as

$$R_{cc}(\tau) = \frac{1}{N_pT_f}\mathbf{E}\Bigg\{\int_0^{N_pT_f}\sum_{k'=-\infty}^{\infty}\sum_{l'=0}^{L-1}\sum_{l=0}^{L-1}\sum_{h'=0}^{N_s-1}\sum_{h=0}^{N_s-1} a_{l'}a_l \cdot\delta\Big(t - t_0\Big)\delta\Big(t + \tau - k'(N_pT_f) - t_1\Big)dt\Bigg\}. \tag{C.4}$$

Using the definition of delta function

$$\delta(t) = \lim_{\Delta\to 0}\frac{1}{\Delta}\Pi\left(\frac{t}{\Delta}\right) \tag{C.5}$$

where $\Pi\left(\frac{t}{\Delta}\right) = 1,\ -\frac{\Delta}{2} \leq t \leq \frac{\Delta}{2}$, and the property

$$\lim_{\Delta \to 0} \int_{-\infty}^{\infty} \frac{1}{\Delta} \Pi\left(\frac{t}{\Delta}\right) dt = 1, \tag{C.6}$$

it can be shown that

$$\int_0^{N_p T_f} \delta\Big(t - t_0\Big)\, \delta\Big(t + \tau - k'(N_p T_f) - t_1\Big) dt = \delta\Big(\tau - k' N_p T_f - (t_1 - t_0)\Big). \tag{C.7}$$

Therefore, (C.4) simplifies to

$$R_{cc}(\tau) = \frac{1}{N_p T_f} \mathbf{E}\left\{ \sum_{k'=-\infty}^{\infty} \sum_{l'=0}^{L-1} \sum_{l=0}^{L-1} \sum_{h'=0}^{N_s-1} \sum_{h=0}^{N_s-1} a_{l'} a_l \cdot \delta\Big(\tau - k'(N_p T_f) - (t_1 - t_0)\Big) \right\} \tag{C.8}$$

and is given in the explicit form in (5.6).

# Appendix D

# PSD Terms

A general representation for $\{\Phi_i(f)\}$ terms can be found by evaluating the Fourier transform of (5.9), where

$$\Phi_i(f) \equiv \sum_z \sum_{(l,h)_{(i)}} \mathbf{E}\Big\{a_x a_y\Big\}\mathbf{E}\Big\{e^{-j2\pi f c_{m_k}(z)T_c}\Big\}\mathbf{E}\Big\{e^{-j2\pi f[d_x-d_y]\delta_d}\Big\}e^{-j2\pi f z T_f}. \tag{D.1}$$

Let the expectation values of the data terms be defined as

$$\mathbf{E}\{a_x a_y\} = \begin{cases} R_0^a, & \text{if } x = y \\ R_1^a, & \text{if } x \neq y \end{cases} \tag{D.2}$$

$$\mathbf{E}\{e^{-j2\pi f[d_x-d_y]\delta_d}\} = \begin{cases} R_0^d(f), & \text{if } x = y \\ R_1^d(f), & \text{if } x \neq y. \end{cases} \tag{D.3}$$

For $\Pr[c_{m_x}] = \frac{1}{M}$ for $\forall m_x$, $m_x \in \{0, \ldots, M-1\}$, the expectation value of the code term can be given as

$$\mathbf{E}\Big\{e^{-j2\pi f c_{m_k}(z)T_c}\Big\} = C_{m_k}(f) = \frac{1}{M^3}\sum_{m_0=0}^{M-1}\sum_{m_1=0}^{M-1}\sum_{m_2=0}^{M-1} e^{-j2\pi f c_{m_k}(z)T_c}. \tag{D.4}$$

Based on (D.1) – (D.4) and considering the sub–regions, $\{\Phi_i(f)\}$'s can be found as

$$\Phi_1(f) = \sum_{|z|<N_s}\Bigg(\sum_{(l,h)_{(1,1)}} R_0^a R_0^d(f) C_{m_0}(f) + \sum_{(l,h)_{(1,2)}} R_1^a R_1^d(f) C_{m_0}(f) + \sum_{(l,h)_{(1,3)}} R_1^a R_1^d(f) C_{m_1}(f)\Bigg) e^{-j2\pi f z T_f} \tag{D.5}$$

$$\Phi_2(f) = \sum_{N_s \leq |z| < N_p} \left( \sum_{(l,h)_{(2,1)}} C_{m_0}(f) + \sum_{(l,h)_{(2,2)}} C_{m_1}(f) \right) \cdot R_1^a R_1^d(f) e^{-j2\pi f z T_f} \tag{D.6}$$

$$\begin{aligned} \Phi_3(f) = \Bigg\{ & \sum_{-N_p < z \leq 0} \left( \sum_{(l,h)_{(3,1)}} C_{m_1}(f) + \sum_{(l,h)_{(3,2)}} C_{m_2}(f) \right) e^{-j2\pi f z T_f} \\ & + \sum_{0 \leq z < N_p} \left( \sum_{(l,h)_{(3,1)}} C_{m_1}(f) + \sum_{(l,h)_{(3,2)}} C_{m_2}(f) \right) e^{-j2\pi f z T_f} \Bigg\} \\ & \cdot R_1^a R_1^d(f) \left( \frac{1}{2N_p T_f} \sum_{k=-\infty}^{\infty} \delta\left( f - \frac{k}{N_p T_f} \right) - 1 \right) + \left( \sum_{\{z=0\}} \sum_{(l,h)_{(3,1)}} C_{m_1}(f) \right) R_1^a R_1^d(f). \end{aligned} \tag{D.7}$$

# Bibliography


[1] FCC Report and Order, *In the Matter of Revision of Part 15 of the Commission's Rules Regarding Ultra-Wideband Transmission Systems*, FCC 02-48, Apr. 2002.

[2] Multi-Band OFDM Physical Layer Proposal for IEEE 802.15 Task Group 3a, IEEE 802.15.3a Working Group, P802.15-03/268r2, 2003.

[3] DS-UWB Physical Layer Submission to 802.15 Task Group 3a, IEEE 802.15.3a Working Group, P802.15-04/0137r0, 2004.

[4] Draft P802.15.4a/D6, IEEE 802.15.4a Working Group, Mar. 2006.

[5] M. Z. Win and R. A. Scholtz, "Impulse radio: how it works," *IEEE Commun. Lett.*, vol. 2, pp. 36–38, Feb. 1998.

[6] R. A. Scholtz, "Multiple access with time-hopping impulse modulation," *IEEE Proc. MILCOM '93*, vol. 2, pp. 447–450.

[7] M. Z. Win and R. A. Scholtz, "Ultra-wide bandwidth time-hopping spread-spectrum impulse radio for wireless multiple-access communications," *IEEE Trans. Commun.*, vol. 48, pp. 679–691, Apr. 2000.

[8] F. Ramirez-Mireles, "Performance of ultrawideband SSMA using time hopping and M-ary PPM," *IEEE J. Sel. Areas Commun.*, vol. 19, pp. 1186–1196, June 2001.

[9] J. G. Proakis, Digital Communications, 4th ed., McGraw Hill, New York, 2001.

[10] C. J. Le Martret and G. B. Giannakis, "All-digital PAM impulse radio for multiple-access through frequency-selective multipath" *IEEE Proc. GLOBECOM '00*, vol. 1, pp. 77–81.

[11] N. H. Lehmann and A. M. Haimovich, "The power spectral density of a time hopping UWB signal: a survey," *IEEE Ultra Wideband Systems and Tech. Conf. '03*, pp. 234–239.

[12] M. L. Welborn, "System considerations for ultra-wideband wireless networks," *IEEE Proc. RAWCON '01*, pp. 5–8.

[13] H. Zhang and T. A. Gulliver, "Performance and capacity of PAM and PPM UWB systems with multiple receive antennas," *IEEE Proc. PACRIM '03*, vol. 2, pp. 740–743.

[14] N. Laurenti, T. Erseghe, and V. Cellini, "On the performance of TH-PPM and TH-PAM as transmission formats for UWB communications," *IEEE Proc. VTC '04 Spring*, vol. 2, pp. 947–951.

[15] B. Hu and N. C. Beaulieu, "Accurate evaluation of multiple-access performance in TH-PPM and TH-BPSK UWB systems," *IEEE Trans. Commun.*, vol. 52, pp. 1758–1766, Oct. 2004.

[16] J. Zhang, T. D. Abhayapala, and R. A. Kennedy, "Performance of ultra-wideband correlator receiver using Gaussian monocycles, *IEEE Proc. ICC '03*, vol. 3, pp. 2192-2196.

[17] H. Sheng, P. Orlik, A. M. Haimovich, L. J. Cimini, and J. Zhang, "On the spectral and power requirements for ultra-wideband transmission," *IEEE Proc. ICC '03*, vol. 1, pp. 738–742.

[18] B. Hu and N. C. Beaulieu, "Pulse shapes for ultrawideband communication systems," *IEEE Trans. Commun.*, vol. 4, pp. 1789–1797, July 2005.

[19] C. Mitchell and R. Kohno, "High data rate transmissions using orthogonal modified Hermite pulses in UWB communications," *10th Intl. Conf. Telecommun. '03*, vol. 2, pp. 1278–1283.

[20] B. Parr, B. L. Cho, K. Wallace, and Z. Ding, "A novel ultra-wideband pulse design algorithm," *IEEE Commun. Lett.*, vol. 7, pp. 219–221, May 2003.

[21] L. Zhao and A. M. Haimovich, "Capacity of M-ary PPM ultra-wideband communications over AWGN channels," *IEEE Proc. VTC '01 Fall*, vol. 2, pp. 1191–1195.

[22] N. V. Kokkalis, P. T. Mathiopoulos, G. K. Karagiannidis, and C. S. Koukourlis, "Performance analysis of M-ary PPM TH-UWB systems in the presence of MUI and timing jitter," *IEEE J. Sel. Areas Commun.*, vol. 24, pp. 822–828, Apr. 2006.

[23] G. Durisi, J. Romme, and S. Benedetto, "A general method for SER computation of M-PAM and M-PPM UWB systems for indoor multiuser communications," *IEEE Proc. GLOBECOM '03*, vol. 2, pp. 734–738.

[24] S. Niranjayan, A. Nallanathan, and B. Kannan, "Modeling of multiple access interference and SER derivation for M-ary TH-PAM/PPM UWB systems," *IEEE Proc. VTC '05 Spring*, vol. 3, pp. 2008–2012.

[25] H. Liu, "Error performance of a pulse amplitude and position modulated ultra-wideband system over lognormal fading channels," *IEEE Commun. Lett.*, vol. 7, pp. 531–533, Nov. 2003.

[26] H. Zhang, W. Li, and T. A. Gulliver, "Pulse position amplitude modulation for time-hopping multiple-access UWB communications," *IEEE Trans. Commun.*, vol. 53, pp. 1269–1273, Aug. 2005.

[27] H. Harada, K. Ikemoto, and R. Kohno, "Modulation and hopping using modified Hermite pulses for UWB communications," *Intl. Workshop UWB Systems and Technol. '04*, pp. 336–340.

[28] J. A. N. da Silva and M. L. R. de Campos, "Spectrally efficient UWB pulse shaping with application in orthogonal PSM," *IEEE Trans. Commun.*, vol. 55, pp. 313–322, Feb. 2007.

[29] R. Hoctor and H. Tomlinson, "Delay-hopped transmitted-reference RF communications," *IEEE Proc. UWBST '02*, pp. 265–269.

[30] S. Gezici, F. Tufvesson, and A. F. Molisch, "On the performance of transmitted-reference impulse radio," *IEEE Proc. Globecom '04*, vol. 5, pp. 2874–2879.

[31] T. Q. S. Quek and M. Win, "Analysis of UWB transmitted-reference communication systems in dense multipath channels," *IEEE J. Sel. Areas Commun.*, vol. 23, pp. 1863-1874, Sept. 2005.

[32] X. Dong, L. Xiao, and A. Lee, "Performance analysis of dual pulse transmission in UWB channels," *IEEE Commun. Lett.*, vol. 10, pp. 626–628, Aug. 2006.

[33] D. I. Kim and T. Jia, "M-ary orthogonal coded/balanced UWB transmitted-reference system," *IEEE Proc. ICC '06*, vol. 12, pp. 5552–5557.

[34] W. M. Lovelace and J. K. Townsend, "The effects of timing jitter and tracking on the performance of impulse radio," *IEEE J. Sel. Areas Commun.*, vol. 20, pp. 1646–1651, Dec. 2002.

[35] J. Chen, T. Lv, Y. Chen, and J. Lv, "A timing-jitter robust UWB modulation scheme," *IEEE Signal Proc. Lett.*, vol. 13, pp. 593–596, Oct. 2006.

[36] X. Wu, Z. Tian, T. N. Davidson, and G. B. Giannakis, "Optimal waveform design for UWB radios," *IEEE Trans. Signal Proc.*, vol. 54, pp. 2009–2021, June 2006.

[37] X. Luo, L. Yang, and G. B. Giannakis, "Designing optimal pulse-shapers for UWB radios," *J. Commun. Netw.*, vol. 5, no. 4, pp. 344-353, Dec. 2003.

[38] N. C. Beaulieu and B. Hu, "A novel pulse design algorithm for ultra-wideband communications," *IEEE Proc. GLOBECOM '04*, vol. 5, pp. 3220–3224.

[39] J. Romme and L. Piazzo, "On the power spectral density of time-hopping impulse radio," *IEEE Ultra Wideband Systems and Tech. Conf. '02*, pp. 241–244.

[40] S. Erküçük and D. I. Kim, "Power spectral density characteristics of MCSK based impulse radios in UWB communications," *IEEE Proc. VTC '05 Spring*, vol. 2, pp. 1391–1395.

[41] L. Piazzo, "Performance analysis and optimization for impulse radio and direct-sequence impulse radio in multiuser interference," *IEEE Trans. Commun.*, vol. 52, pp. 801–810, May 2004.

[42] Y. P. Nakache and A. F. Molisch, "Spectral shape of UWB signals – influence of modulation format, multiple access scheme and pulse shape," *IEEE Proc. VTC '03 Spring*, vol. 4, pp. 2510–2514.

[43] Y. P. Nakache and A. F. Molisch, "Spectral shaping of UWB signals for time-hopping impulse radio," *IEEE J. Sel. Areas Commun.*, vol. 24, pp. 738–744, Apr. 2006.

[44] M. Z. Win, "A unified spectral analysis of generalized time-hopping spread-spectrum signals in the presence of timing jitter," *IEEE J. Select. Areas Commun.*, vol. 20, pp. 1664–1676, Dec. 2002.

[45] M. Hamalainen, V. Hovinen, R. Tesi, J. H. J. Iinatti, and M. Latva-aho, "On the UWB system coexistence with GSM900, UMTS/WCDMA, and GPS," *IEEE J. Select. Areas Commun.*, vol. 20, pp. 1712–1721, Dec. 2002.

[46] J. Bellorado, S. S. Ghassemzadeh, L. J. Greenstein, T. Sveinsson, and V. Tarokh, "Coexistence of ultra-wideband systems with IEEE-802.11a wireless LANs," *IEEE Proc. GLOBECOM '03*, vol. 1, pp. 410–414.

[47] Y. Wang, X. Dong, and I. J. Fair, "A method for spectrum shaping and NBI suppression in UWB communications," *IEEE Proc. ICC '06*, vol. 4, pp. 1476–1481.

[48] J. Bellorado, S. S. Ghassenzadeh, A. Kavcic, B. Tarokh, and V. Tarokh, "Time-hopping sequence design for narrowband interference suppression," *IEEE Proc. VTC '04 Fall*, vol. 6, pp. 3925–3929.

[49] M. Pendergrass, "Empirically based statistical ultra-wideband channel model," IEEE P802.15-02/240-SG3a, 2002.

[50] J. R. Foerster and Q. Li, "UWB channel modeling contribution from Intel," IEEE P802.15 02/279SG3a, 2002.

[51] S. Ghassemzadeh and V. Tarokh, "The ultra-wideband indoor multipath loss model," IEEE P802.15-02/282-SG3a and IEEE P802.15-02/283-SG3a, 2002.

[52] A. Molisch, M. Win, and D. Cassioli, "The ultra-wide bandwidth indoor channel: from statistical model to simulations," IEEE P802.15-02/284-SG3a and IEEE P802.15-02/285-SG3a, 2002.

[53] J.-M. Cramer, R. Scholtz, and M. Win, "Evaluation of an indoor ultra-wideband propagation channel," IEEE P802.15-02/286-SG3a and IEEE P802.15-02/325-SG3a, 2002.

[54] J. R. Foerster *et. al.*, "Channel modeling subcommittee final report," IEEE P802.15-02/490-SG3a, Feb. 2003.

[55] A. Saleh and R. Valenzuela, "A statistical model for indoor multipath propagation," *IEEE J. Sel. Areas Commun.*, vol. 5, pp. 128–137, Feb. 1987.

[56] A. Molisch, "Ultrawideband propagation channels-theory, measurement, and modeling," *IEEE Trans. Vehic. Tech.*, vol. 54, pp. 1528–1545, Sep. 2005.

[57] A. F. Molisch, D. Cassioli, C.-C. Chong, S. Emami, A. Fort, B. Kannan, J. Karedal, J. Kunisch, H. G. Schantz, K. Siwiak, and M. Z. Win, "A comprehensive standardized model for ultrawideband propagation channels," *IEEE Trans. Antennas and Prop.*, vol. 54, pp. 3151–3166, Nov. 2006.

[58] S. Zhao and H. Liu, "On the optimum linear receiver for impulse radio systems in the presence of pulse overlapping," *IEEE Commun. Lett.*, vol. 9, pp. 340–342, Apr. 2005.

[59] X. Chu and R. D. Murch, "Performance analysis of DS-MA ultra-wideband communications incorporating channel-induced pulse overlap," *IEEE Trans. Wireless Commun.*, vol. 5, pp. 948–959, April 2006.

[60] S. Erküçük, D. I. Kim, and K. S. Kwak, "Effects of channel models and Rake receiving process on UWB-IR system performance," *IEEE Proc. ICC '07.*

[61] B. Mielczarek, M-O. Wessman, and A. Svensson, "Performance of coherent UWB Rake receivers with channel estimators," *IEEE Proc. VTC '03 Fall*, vol. 3, pp. 1880–1884.

[62] M. A. Rahman, S. Sasaki, J. Zhou, and H. Kikuchi, "On the Rake reception of ultra wideband signals over multipath channels from energy capture perspective," *IEICE Trans. Fundamentals*, vol. E88–A, pp. 2339–2349, Sep. 2005.

[63] T. Jia and D. I. Kim, "Analysis of channel-averaged SINR for indoor UWB Rake receiving and transmitted reference systems," to appear in *IEEE Trans. Commun.*

[64] S. Erküçük and D. I. Kim, "UWB-IR system performance for implementable Rake receivers," *IEEE Proc. Canadian Conf. Elec. and Comp. Engineering '07.*

[65] S. Erküçük, D. I. Kim, and K. S. Kwak, "Code shift keying impulse modulation for UWB communications," to appear in *IEEE Trans. Wireless Commun.*

[66] J. Fiorina, "A simple IR-UWB receiver adapted to multi-user interferences," *IEEE Proc. GLOBECOM '06.*

[67] S. Erküçük and D. I. Kim, "Spectral characteristics of M-ary code shift keying based impulse radios: effects of code design," *IEEE Trans. Wireless Commun.*, vol. 6, pp. 2266–2275, June 2007.

[68] M. Abramowitz and I. A. Stegun, Handbook of Mathematical Functions with Formulas, Graphs, and Mathematical Tables, Dover, New York, 1972.

[69] A. Papoulis, The Fourier Integral and Its Applications. McGraw Hill, New York, 1962.

[70] S. Erküçük and D. I. Kim, "Combined $M$-ary code shift keying/binary pulse position modulation for ultra wideband communications," *IEEE Proc. GLOBECOM '04*, vol. 2, pp. 804–808.

[71] S. Erküçük and D. I. Kim, "$M$-ary code shift keying impulse modulation combined with BPPM for UWB communications," *IEEE Trans. Wireless Commun.*, vol. 6, pp. 2255–2265, June 2007.

[72] M. B. Pursley and H. F. A. Roefs, "Numerical evaluation of correlation parameters for optimal phases of binary shift-register sequences," *IEEE Trans. Commun.*, vol. 27, pp. 1597–1604, Oct. 1979.

[73] S. Kim, K.-H. Park, S. Yang, H.-S. Kim, and Y. Shin, "Time hopping sequences based on pseudo random codes for ultra wideband impulse radio systems," *Proc. Intl. Tech. Conf. Circuits/Systems, Comp. and Commun. '02.*

[74] D. Cassioli, M. Z. Win, F. Vatalaro, and A. F. Molisch, "Performance of low-complexity RAKE reception in a realistic UWB channel," *IEEE Proc. ICC 2002*, vol. 2, pp. 763–767.

[75] S. M. Ross, Introduction to Probability Models, 3rd ed., Academic Press Inc., Florida, 1985.

[76] S. Erküçük and D. I. Kim, "Effects of code design on the spectral characteristics of MCSK based impulse radios," *IEEE Proc. ICC '06*, vol. 10, pp. 4757–4762.

[77] G. B. Aiello and G. D. Rogerson, "Ultra-wideband wireless systems," *IEEE Microwave Mag.*, pp. 36–47, June 2003.

[78] S. Villarreal-Reyes, R. M. Edwards, and J. C. Vardaxoglou, "On the use of simulation-DFT based analysis for spectral estimation of PPM TH-IR UWB signals," *IEEE Proc. VTC '05 Spring*, vol. 2, pp. 1370–1374.

[79] S. Erküçük, D. I. Kim, and K. S. Kwak, "Code shift keying modulation for low-rate UWB communications under dense multipath," *IEEE Proc. GLOBECOM '06*.

[80] S. M. Kay, Fundamentals of Statistical Signal Processing: Detection Theory, Prentice Hall, Englewood Cliffs, 1998.

[81] H. Mathis, Nonlinear Functions for Blind Separation and Equalization, PhD. Thesis, Swiss Federal Institute of Technology, Zurich, Switzerland, Nov. 2001.

[82] D. I. Kim, "Combined binary pulse position modulation/biorthogonal modulation for direct-sequence code division multiple access," *IEEE Trans. Commun.*, vol. 47, pp. 22–26, Jan. 1999.

[83] D. I. Kim, S. Erküçük, and K. S. Kwak, "UWB MCSK/BPPM wireless communication system and method for increased information rate," US Patent application number: 11/157297, June 2005.

[84] D. I. Kim, S. Erküçük, and K. S. Kwak, "M-ary Code Shift Keying/Binary PPM (MCSK/BPPM) Based Impulse Radio," *doc. IEEE 802.15-05-0022-02-004a*, Jan. 2005.

[85] D. I. Kim, S. Erküçük, and K. S. Kwak, "Merged proposal of Chaotic UWB System for IEEE 802.15.4a contributed section: Combined M-ary code Shift/Differential Chaos Shift Keying," *doc. IEEE 802.15-05-0132-03-004a*, Mar. 2005.

[86] S. Erküçük, D. I. Kim, and K. S. Kwak, "Code Shift Keying for UWB PHY," *doc. IEEE 802.15-06-0045-00-004a*, Jan. 2006.

[87] S. Erküçük and D. I. Kim, "Combined M-ary code shift/differential chaos shift keying for low-rate UWB communications," *IEEE Proc. Intl. Conf. on Ultra Wideband '05*, pp. 33–37.